Title
Nanoplasmonics-enabled On-Demand and Systematic Gene Regulation

Author
Lee, Eunice Somin

Publication Date
2010

Peer reviewed|Thesis/dissertation

Nanoplasmonics-enabled On-Demand and Systematic Gene Regulation

by

Eunice Somin Lee

A dissertation submitted in partial satisfaction of the

requirements for the degree of

Joint Doctor of Philosophy
with University of California, San Francisco

in

Bioengineering

in the

Graduate Division

of the

University of California, Berkeley

Committee in charge:

Professor Luke P. Lee, Chair
Professor Michel Maharbiz
Professor Tejal Desai
Professor Han Lim

Spring 2010

Nanoplasmonics-enabled On-Demand and Systematic Gene Regulation

by Eunice Somin Lee

Abstract

Nanoplasmonics-enabled On-Demand and Systematic Gene Regulation

by

Eunice Somin Lee

Joint Doctor of Philosophy
with University of California, San Francisco

University of California, Berkeley

Professor Luke P. Lee, Chair

In this dissertation, nanoplasmonic optical antennae are utilized as “nanoplasmonic gene switches” for on-demand and systematic gene regulation in living systems. The plasmon resonance of nanoplasmonic gene switches is specifically tuned to the near-infrared spectral region where cells and tissues are essentially transparent. Due to their extraordinarily large surface-to-volume ratio, nanoplasmonic gene switches are ideal carriers of interfering oligonucleotides, such as antisense DNA and short interfering RNA oligonucleotides (siRNA). Interfering oligonucleotides enable direct, sequence-specific silencing of genes, but alone, lack the temporal control necessary for precise spatiotemporal manipulation. While interfering oligonucleotides are attached to nanoplasmonic gene switches, oligonucleotide functionality is inactivated. Using light illumination as a remote trigger to release free oligonucleotides and “activate” their functionality, genes can be silenced on-demand. In addition to inhibitory effects, genes are also expressed on-demand. A transcriptional pulse of target gene expression is generated using nanoplasmonic gene switches of different aspect ratios to selectively and temporally manipulate the activities of repressors and activators upstream from the target gene. In this way, the magnitude and timing of genetic activities can be systematically varied on-demand. Equipped with new nanoplasmonic tools to directly probe the intracellular space, quantitative approaches should capture many dynamic activities within the living cell that were otherwise previously impossible to detect using conventional methods.

TABLE OF CONTENTS

CHAPTER 1: INTRODUCTION

A single living cell is an amazingly dynamic system that is capable of constantly sensing and responding to its perpetually changing environment. As such, it is an integrated system consisting of extracellular input signals streaming in from the local external environment, interlinked signaling cascades of internal connections, and gene transcriptional networks that respond by producing the appropriate proteins to give rise to cell function (Fig. 1.1). Quantitatively understanding the inner workings of these systems is the quest set forth by quantitative cell biology and systems biology. By systematically perturbing with extracellular stimuli, specific internal connections can be mapped and the resulting cell function can be observed in response to the single environmental change. Spatial, temporal, and systematic variation of extracellular stimuli has been shown to be absolutely critical for developmental processes (1), growth (2), differentiation (3), apoptosis, and stem cell fate decisions (4).

In addition to extracellular control of environmental stimuli, intracellular control of the actual internal connections themselves can provide unparalleled insight into the inner workings of these systems. When a cell is treated as input-output "black box," ideally, the output response is directly correlated to the input signal. However, signal distortions - time delays, noise, and signal magnitude reductions - can confound this input-output relationship. Time delays, due to inherent time-dependent interactions, transcriptional rates, and translational rates, are associated with each interconnected step inside the "black box." Noise, from stochastic fluctuations in proteins, is introduced at each stage inside the "black box." Signal magnitude reductions, due to degradation, dilution and diffusion effects, are also inevitable. These signal distortions can have significant implications on the output response. Consider a simple transcriptional network, where gene X regulates gene Y, and gene Y in turn regulates the output. In the presence of its input signal, X becomes active. Threshold effects are known to govern many gene regulatory processes (5). Thus, when the concentration of X is greater than the threshold concentration required for activating Y, then Y is produced. Subsequently, when the concentration of Y is greater than the threshold concentration required for activating the output, then the output is produced. Now, suppose that the input signal is externally introduced (Fig. 1.1a). As this extracellular input signal traverses through each step of the extracellular-to-intracellular cascade, signal distortions are introduced. If the signal is significantly confounded by noise or if the signal magnitude is significantly reduced such that the activity of Y no longer satisfies the threshold condition (Fig. 1.1b), the output is not produced (Fig. 1.1c). This result can give the misleading impression that no relationship exists between the input signal and Y, when in fact they are related. Internal connections can be incorrectly mapped. Suppose now that Y is directly controlled at the intracellular level (Fig. 1.1d). Steps in the extracellular-to-intracellular cascade are essentially bypassed, thereby minimizing signal distortions. As a result, the output is reliably produced (Fig. 1.1e). Internal connections can be correctly mapped.

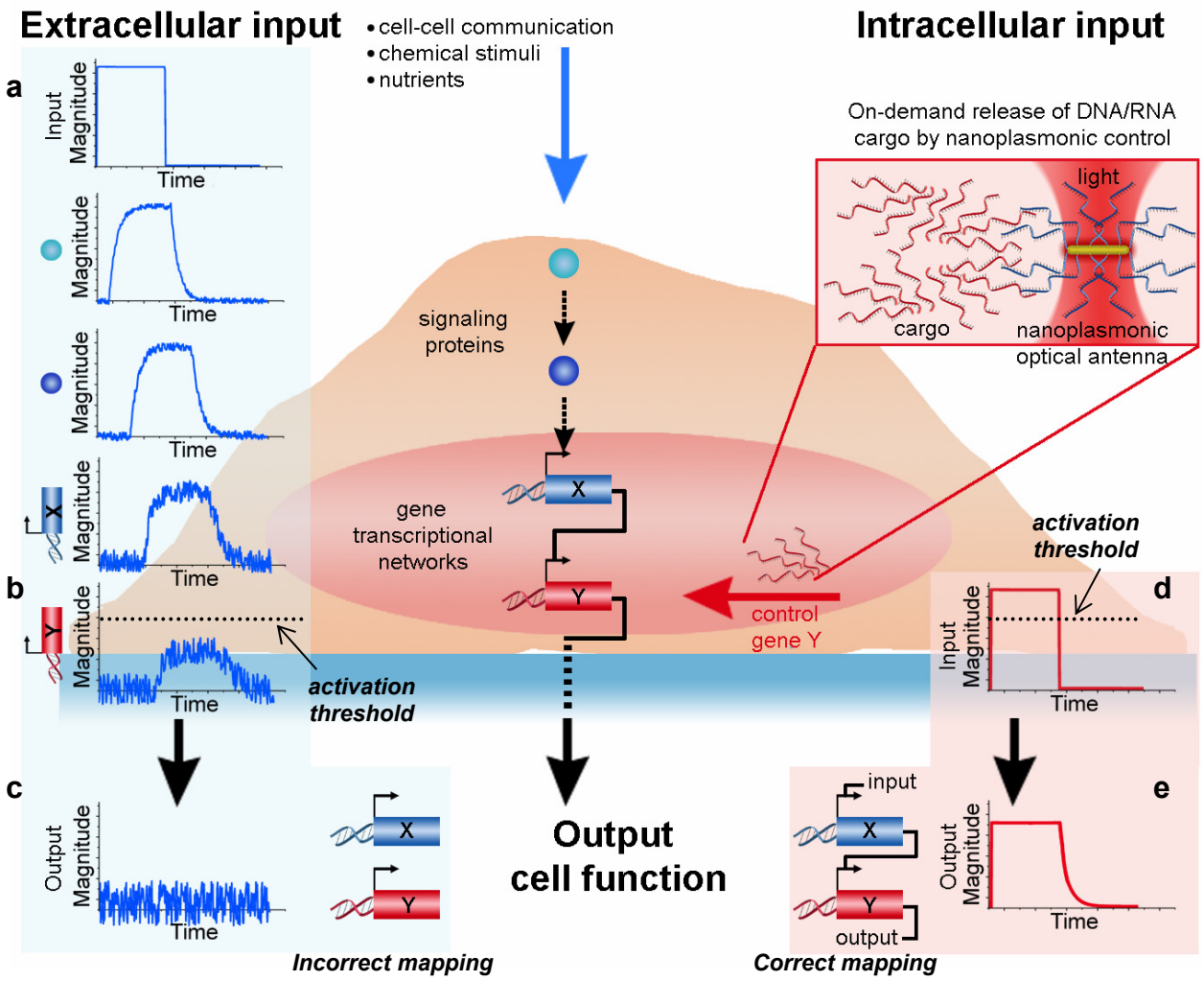

Figure 1.1. Concept of nanoplasmonics-enabled on-demand and systematic intracellular gene regulation. (a) Extracellular Control. Extracellular input signals, such as chemical stimuli or nutrients, are externally introduced. As this extracellular input signal traverses through each step of the extracellular-to-intracellular cascade, signal distortions are introduced. **(b)** The activity of Y does not satisfy the threshold condition due to signal distortions. **(c)** The output is not produced. This result gives the misleading impression that no relationship exists between the input signal and Y, when in fact they are related. Internal connections are incorrectly mapped. **(d) Intracellular Control.** Nanoplasmonic optical antennae are used as carriers of oligonucleotide cargo. Using light illumination as a remote trigger to release free oligonucleotides and "activate" their functionality, Y is directly controlled at the intracellular level. Signal distortions are minimized since steps in the extracellular-to-intracellular cascade are essentially bypassed. As a result, the output is reliably produced and internal connections are correctly mapped.

By delving directly into the intracellular "black box," the magnitude and timing of intracellular processes can be precisely controlled. Interfering oligonucleotides, such as DNA, RNA, short hairpin RNA (shRNA), and short interfering RNA (siRNA), enable direct, sequence-specific control of intracellular genes, but alone, lack the temporal control necessary for precise manipulation. Recent advancements in chemical biology,

nanotechnology, and plasmonics now enable new light-sensitive tools of sub-nanometer and nanometer size scales to directly interface with intracellular processes. For example, nanoplasmonic optical antennae can be used as carriers of oligonucleotide cargo (Fig. 1.1d). Initially, oligonucleotide functionality is inactivated. Using light illumination as a remote trigger to release free oligonucleotides and "activate" their functionality, endogenous intracellular genes can be silenced on-demand. In addition to the inhibitory effects of interfering oligonucleotides, exogenous foreign genes can be also introduced and expressed on-demand. In this way, the magnitude and timing of genetic activities can be systematically varied on-demand. Signal distortions can be minimized since light-sensitive tools are activated from within the intracellular space, and therefore, steps in the extracellular-to-intracellular cascade are bypassed at the time of activation. Equipped with new tools to directly probe the intracellular space, quantitative and systematic approaches should capture many dynamic activities within the living cell that were otherwise previously impossible to detect using conventional methods.

Caging Technologies

Caging is also an effective means to temporarily inactivate oligonucleotide functionality by incorporating photo-labile protective groups, otherwise known as caging groups, into the bases or the phosphate backbone (6). Ultra-violet (UV) irradiation removes the caging groups and restores oligonucleotide functionality. UV-activated gene silencing using caged antisense DNA has been demonstrated in mouse NIH 3T3 fibroblast cells (7). UV-activated gene silencing using caged siRNA has also been demonstrated in human HeLa cervical carcinoma cells (8). While caging enables excellent spatiotemporal control of intracellular genes, the particular use of UV wavelengths is of some concern since intracellular proteins and nucleic acids are widely known to absorb, crosslink, and mutagenize in the presence of UV irradiation. Therefore, activation using less biologically harmful wavelengths of light is highly desirable.

NIR Nanoplasmonic Optical Antennae

Gold nanoplasmonic optical antennae, in the near-infrared (NIR) spectral region, are attractive candidates for intracellular control. The NIR wavelength regime is well suited for biological and biomedical applications since tissues and cells are essentially transparent between 700-1300 nm (9). Due to their strong and sharp resonance peak in their optical properties, nanoplasmonic optical antennae efficiently convert light energy into surface-localized heat, otherwise known as photothermal conversion (10-12), when the incident light is matched to their plasmon resonance wavelength. In the presence of this incident light, the conduction electrons of the antennae collectively oscillate in phase on resonance and subsequently make collisions with the metal lattice, thereby dissipating heat (12). Heat transfer from the surface of antennae' to the surrounding cellular environment is highly localized, decaying exponentially within a few nanometers (10, 13, 14) and therefore is thought to have minimal adverse effects on cells. Among the nanoplasmonic optical antennae geometries, rod-shaped nanoplasmonic optical

antennae, otherwise known as gold nanorods (13, 15, 16), are of widespread interest and pervasive use due to their large absorption cross-section, facile tunability of their plasmon resonance wavelength based on geometry, narrow spectral width of the longitudinal plasmon resonance band, and uniformly large-scale synthesis (Fig. 1.2).

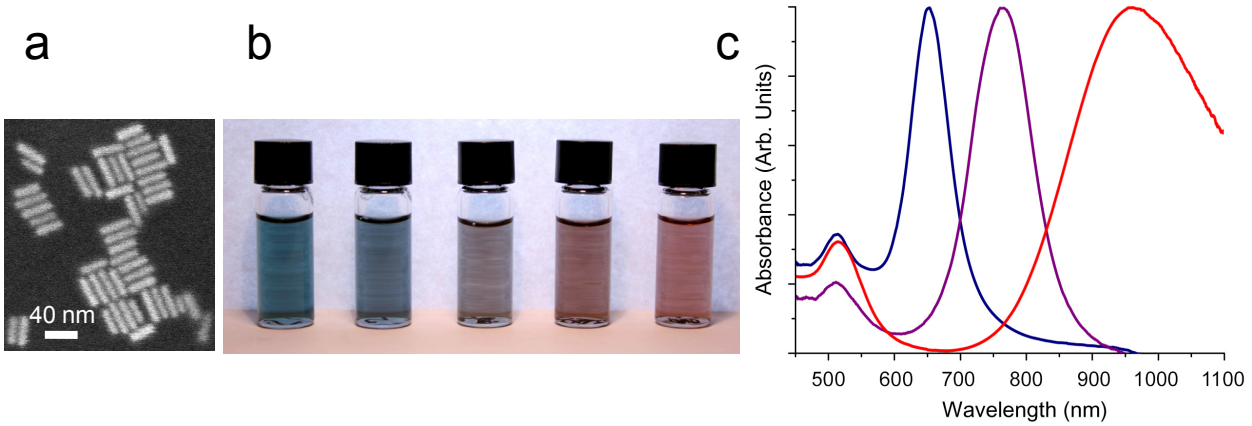

Figure 1.2. Rod-shaped nanoplasmonic optical antennae (gold nanorods). (a) Scanning electron microscopy image showing uniformly large-scale synthesis, **(b)** visual image showing facile tunability of the plasmon resonance wavelength, and **(c)** UV-VIS absorbance spectra showing large absorption cross-sections of rod-shaped nanoplasmonic optical antennae (otherwise known as gold nanorods).

Because of their extraordinarily large surface-to-volume ratio, nanoplasmonic optical antennae are ideal carriers of cargo, such as interfering oligonucleotides. While attached to their carriers, cargo is rendered inactive due to steric hinderances between the tightly-packed cargo. In the presence of light that is matched to their plasmon resonance wavelength, carriers photothermally release their cargo to freely interact with the local environment. Several strategies, employing different carrier and cargo types, have been demonstrated. For example, it is shown in this dissertation that short single-stranded DNA, otherwise known as antisense DNA, can be hybridized to a thiolated complementary sense strand, bound to a gold nanorod's surface through the gold-thiol covalent bond, and photothermally dehybridized using continuous-wave incident light that is matched to the plasmon resonance wavelength of the gold nanorods (13) (Fig. 1.3a). Antisense DNA can also be photothermally dehybridized from other geometries, such as gold nanoshells (17) (Fig. 1.3b) and gold nanoprisms (18) (Fig. 1.3c) using continuous-wave illumination. This strategy of photothermal dehybridization using continuous-wave illumination offers several notable advantages. Firstly, no chemical modifications are made to the antisense DNA strand itself since a thiolated complementary strand is used to directly conjugate to the carrier's surface. Because chemical modifications can interfere with nucleic acid functionality and gene silencing efficacy, unmodified antisense DNA is highly desirable. Secondly, gold-thiol covalent bonds are stable after illumination, such that the carrier's surface remains covered with the thiolated complementary sense strands. With respect to cytotoxicity, this surface coating of complementary strands after illumination is critical. While the gold core is widely accepted as being biocompatible, bare gold nanoparticles have been shown to interact with proteins and induce mis-folding at physiological conditions (19).

Maintaining surface coverage with complementary strands after illumination also prevents reattachment of antisense DNA strands back onto the carrier since rehybridization events are thermodynamically unfavorable due to steric hinderances and electrostatic repulsive forces at the carrier's surface (20). Finally, the structural integrity of carriers is uncompromised after illumination. Maintaining structure after illumination allows unique nano-scale optical properties to be retained, thereby enabling the same incident light wavelength to be used. Repetitive or finely-graded release of cargo is conceivable for future applications requiring precise temporal patterns of cargo release. Maintaining structure after illumination is also crucial for *in vivo* applications, where the size, geometry, coating material, and core material of nanoparticles are precisely designed and carefully characterized for proper biodistribution (21).

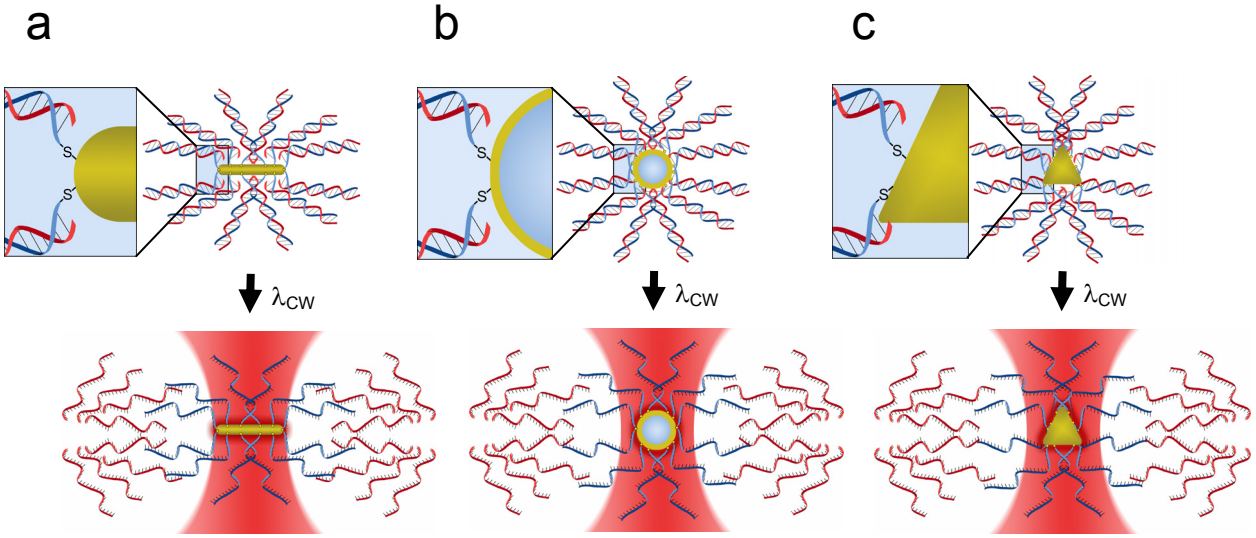

Figure 1.3. Photothermal dehybridization using continuous-wave illumination from nanoplasmonic optical antennae of various geometries. (a) In this dissertation, duplexes of thiol-modified sense and antisense DNA are covalently bound to the gold nanorod. In the presence of continuous-wave illumination, the antisense DNA strands dehybridize while the thiol-modified sense strands remain attached. **(b)** Antisense DNA has also been photothermally dehybridized from gold nanoshells (17). **(c)** Antisense DNA has also been photothermally dehybridized from gold nanoprisms (18).

Alternatively, thiol-modified antisense DNA can be covalently bound to gold nanorods directly. It has been demonstrated that pulsed incident light can photothermally melt gold nanorods into spheres, thereby destabilizing the gold-thiol covalent bond and releasing thiol-modified antisense DNA (22) (Fig. 1.4a). Photothermal melting has also been effective at releasing thiol-modified linearized plasmid DNA from gold nanorods (23) (Fig. 1.4b) and thiol-modified siRNA from gold hollow nanoshells (24) (Fig. 1.4d). Additionally, photothermal melting has been shown to destabilize electrostatically-attached circular plasmid DNA from gold nanorods (25, 26) (Fig. 1.4c). This strategy of photothermal melting using pulsed illumination presents several unique functionalities. Firstly, photothermal melting ensures complete release of all cargo. Secondly, the resulting shape change from rods to spheres enables a distinct and defined shift in the plasmon resonance wavelength. A second light source can be

easily employed to re-match to the plasmon resonance wavelength of these shape-transformed carriers. These functionalities may be useful for future studies that involve multifunctional release and detection schemes. Conceivably, cargo can be completely release from gold nanorods using pulsed illumination, and after a shape transformation, binding activity can then be detected using the now bare gold spherical surface. In the case of gold nanoshells, their silica cores deform after pulsed illumination due to high temperature heating (lattice temperatures reaching ~1064°C, the melting point of bulk gold) (27). As a result, their plasmon resonance wavelength can also shift after illumination, but in a less distinct and controlled manner compared with photothermally melted gold nanorods. Re-matching the incident light wavelength can therefore be considerably more difficult if the plasmon resonance wavelength cannot be easily controlled after shape transformation.

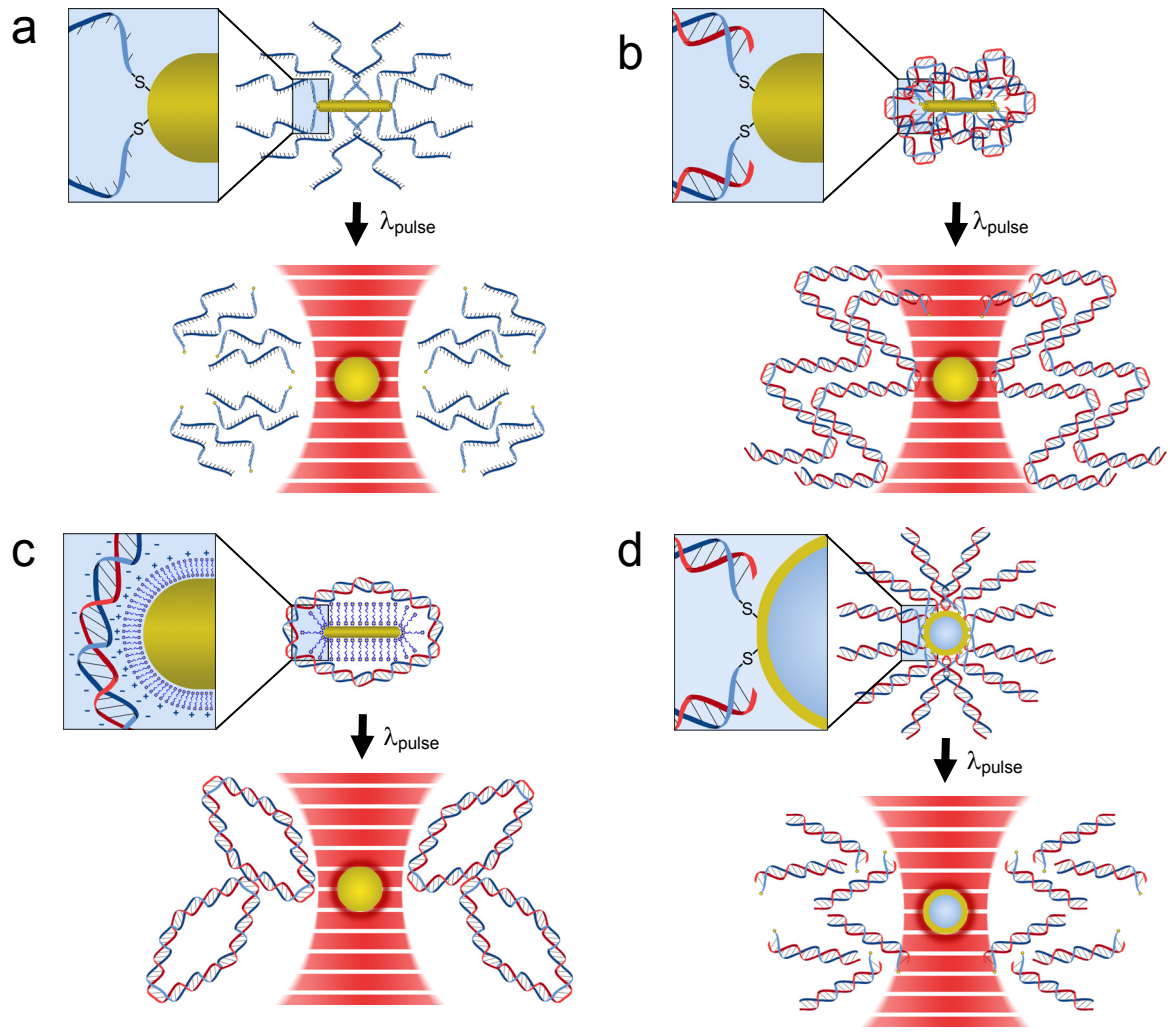

Figure 1.4. Photothermal melting using pulsed illumination. (a) Thiol-modified antisense DNA is released by photothermally melting gold nanorod (22). **(b)** Thiol-modified linearized plasmid DNA is released by photothermally melting gold nanorod (23). **(c)** Electrostatically-attached circular plasmid DNA is released by photothermally melting gold nanorod (25, 26). **(d)** Thiol-modified siRNA is released by photothermally melting gold hollow nanoshell.

Nanoplasmonics-enabled Intracellular Control

Nanoplasmonic optical antennae enable “nanoplasmonic control” of genetic activities with sequence-specificity and spatiotemporal resolution. In this dissertation, rod-shaped nanoplasmonic optical antennae are primarily utilized because of their unique optical properties that arise from their asymmetric geometry. Rod-shaped nanoplasmonic optical antennae carrying genetic cargo are internalized in living cells by endocytosis. While attached to their carriers, the cargo is temporarily “inactive”. The cargo is also protected from degradation by nucleases due to steric hinderances between the tightly-packed cargo at the carriers’ surface (28). Continuous-wave illumination matched to the plasmon resonance wavelength of carriers is used to “activate” cargo by photothermally disrupting encapsulating endosomes (13, 29-31) and photothermally releasing free cargo into the cytosol. In this way, endogenous intracellular genes can be silenced on-demand.

On-demand gene silencing of endogenous intracellular genes using antisense DNA is demonstrated in Chapter 3. In Chapter 3, duplexes of thiol-modified sense and unmodified antisense DNA cargo are covalently bound to carriers and internalized in living cells (Fig. 1.5). In the presence of continuous-wave illumination, antisense DNA strands dehybridize and release into the cytosol, while the thiol-modified sense strands remain attached to the carriers. The unbound antisense DNA then binds to a portion of the corresponding mature mRNA. Once the mRNA/antisense DNA heteroduplex is formed, it is recognized and degraded by RNase H enzymes in the cytosol, thereby silencing the gene-of-interest.

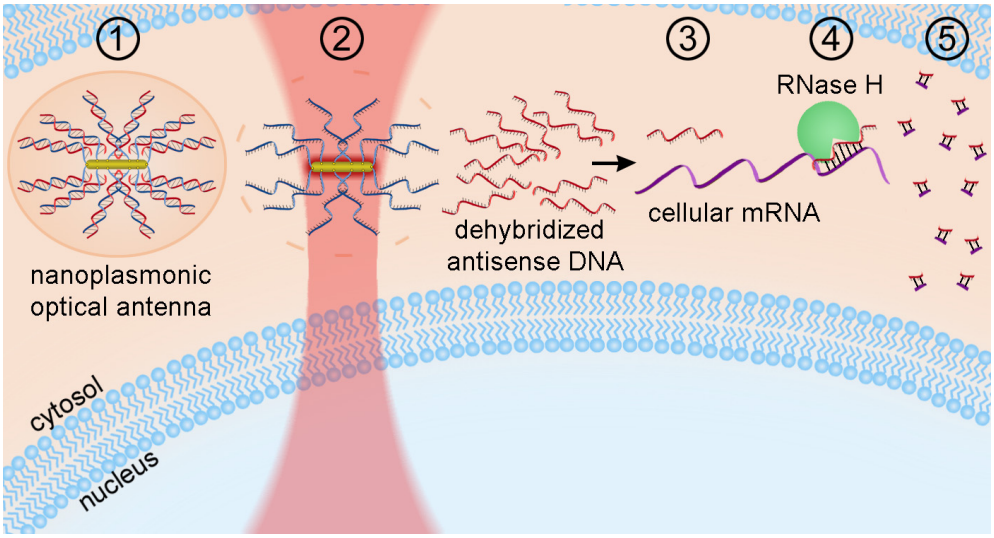

Figure 1.5. On-demand gene silencing mechanism by antisense DNA. *(detailed in Chapter 3)*

In addition to antisense DNA, short interfering RNA (siRNA) is also known to inducing silencing effects. Therefore, biologically functional cationic phospholipid-gold nanoplasmonic carriers that are compatible with and capable of carrying siRNA cargo are described in Chapter 4. These carriers simultaneously exhibit carrier functionality,

demonstrate improved nanoparticle stability, retain nano-scale optical properties, and show no cytotoxicity under physiological conditions

Using biologically functional cationic phospholipid-gold nanoplasmonic carriers of siRNA, on-demand gene silencing of endogenous intracellular genes by siRNA is demonstrated in Chapter 5. In Chapter 5, siRNA duplexes are electrostatically attached to cationic phospholipid-gold nanoplasmonic carriers and internalized in living cells (Fig. 1.6). In the presence of continuous-wave illumination, the electrostatic interaction is destabilized and siRNA duplexes are released into the cytosol. The unbound siRNA duplexes sequentially trigger cytosolic RNA-inducing silencing complex (RISC) to unwind the duplexes, bind to complementary mature mRNA, and silence gene expression.

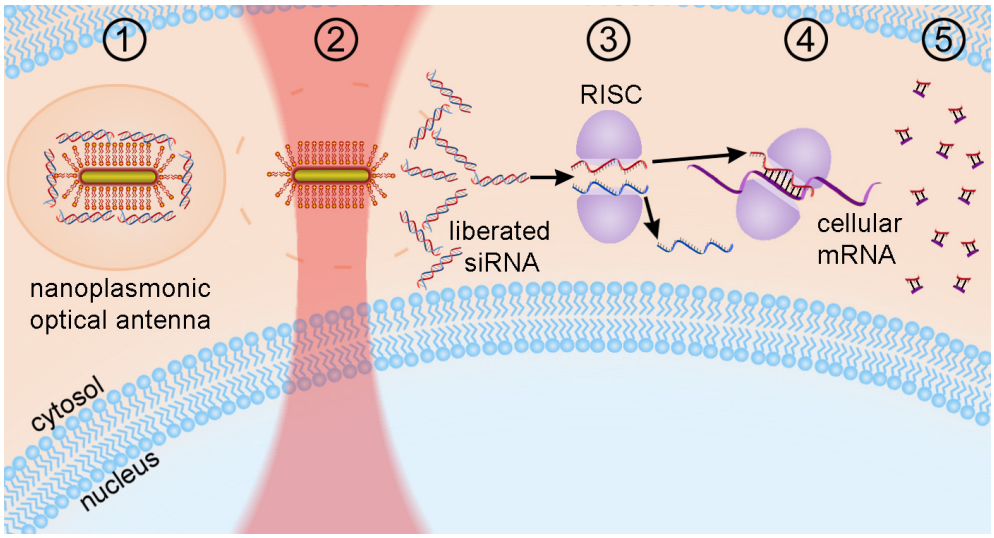

Figure 1.6. On-demand gene silencing mechanism by siRNA. *(detailed in Chapter 5)*

In addition to inhibitory effects, genes can also be expressed on-demand using nanoplasmonic optical antennae. In Chapter 6, a transcriptional pulse of target gene expression is generated using siRNA-conjugated nanoplasmonic gene switches of different aspect ratios to selectively and temporally manipulate the activities of repressors and activators upstream from the target gene. In this way, the magnitude and timing of genetic activities can be systematically varied on-demand. Equipped with new nanoplasmonic optical antennae to directly probe the intracellular space, quantitative and systematic approaches should capture many dynamic activities within the living cell that were otherwise previously impossible to detect using conventional methods.

References

1. Ismagilov, R. F., Maharbiz, M.M., Can We Build Synthetic, Multicellular Systems by Controlling Developmental Signaling in Space and Time?, *Current Opinion in Chemical Biology, 11*, 604 (2007).
2. Hung, P. J., Lee, P.J., Sabounchi, P., Lin, R., Lee, L.P., Continuous Perfusion Microfluidic Cell Culture Array for High Throughput Cell Based Assays, *Biotechnology and Bioengineering, 89*, 1 (2005).
3. Steedman, M. R., Tao, S.L., Klassen, H., Desai, T.A., Enhanced Differentiation of Retinal Progenitor Cells using Microfabricated Topographical Cues, *Biomedical Microdevices* (2010).
4. LaBarge, M. A., Nelson, C.M., Villadsen, R., Fridriksdottir, A., Ruth, J.R., Stampfer, M.R., Peterson, O.W., Bissell, M.J., Human mammary progenitor cell fate decisions are products of interactions with combinatorial microenvironments, *Integrative Biology, 1*, 70 (2009).
5. Little, J. W., Threshold Effects in Gene Regulation: When Some Is Not Enough, *Proceedings of the National Academy of Sciences, 102*, 5310 (2005).
6. Deiters, A., Light-activation as a Method of Regulating and Studying Gene Expression, *Current Opinion in Chemical Biology, 13*, 678 (2009).
7. Young, D. D., Lusic, H., Lively, M.O., Yoder, J.A., Deiters, A., Gene Silencing in Mammalian Cells with Light-Activated Antisense Agents, *ChemBioChem, 9*, 2937 (2008).
8. Mikat, V., Heckel, A., Light-dependent RNA interference with nucleobase-caged siRNAs, *RNA, 13*, 2341 (2007).
9. Svoboda, K., Biological Applications of Optical Forces, *Annu. Rev. Biophys. Biomol. Struct., 23*, 247 (1994).
10. Cortie, M., Xu, X., Chowdhury, H., Zareie, H., Smith, G., Plasmonic Heating of Gold Nanoparticles and Its Exploitation, *Proc. SPIE, 5649*, 565–573 (2005).
11. Khlebtsov, B., Zharov, V., Melnikov, A., Tuchin, V., Khlebtsov, N., Optical Amplification of Photothermal Therapy with Gold Nanoparticles and Nanoclusters, *Nanotechnology, 17*, 5167–5179 (2006).
12. Link, S., El-Sayed, M., Shape and Size Dependence of Radiative, Non-Radiative and Photothermal Properties of Gold Nanocrystals, *Int. Reviews in Physical Chemistry, 19*, 409 (2000).
13. Lee, S. E., Liu, G. L., Kim, F., Lee, L. P., Remote Optical Switch for Localized and Selective Control of Gene Interference, *Nanoletters, 9*, 562 (2009).
14. Skirtach, A. G., Dejugnat, C., Braun, D., Susha, A.S., Rogach, A.L., Parak, W.J., Mohwald, H., Sukhorukov, G.B., The Role of Metal Nanoparticles in Remote Release of Encapsulated Materials, *Nanoletters, 5*, 1371 (2005).
15. Nikoobakht, B., El-Sayed, M. A., Preparation and Growth Mechanism of Gold Nanorods (NRs) Using Seed-Mediated Growth Method, *Chem. Mater., 15*, 1957 (2003).
16. Gou, L., Murphy, C. J., Fine-Tuning the Shape of Gold Nanorods, *Chem. Mater., 17*, 3668 (2005).

17. Barhoumi, A., Huschka, R., Bardhana, R., Knight, M.W., Halas, N.J., Light-Induced Release of DNA from Plasmon-Resonant Nanoparticles: Towards Light-Controlled Gene Therapy, *Chemical Physics Letters, 482*, 171 (2009).
18. Jones, M. R., Millstone, J.E., Giljohann, D.A., Seferos, D.S., Young, K.L., Mirkin, C.A., Plasmonically Controlled Nucleic Acid Dehybridization with Gold Nanoprisms, *ChemPhysChem, 10*, 1461 (2009).
19. Zhang, D., Neumann, O., Wang, H., Yuwono, V.M., Barhoumi, A., Perham, M., Hartgerink, J.D., Wittung-, and Stafshede, P., Halas, N.J., Gold Nanoparticles Can Induce the Formation of Protein-based Aggregates at Physiological pH, *Nanoletters, 9*, 666 (2009).
20. Demers, L. M., Mirkin, C.A., Mucic, R.C., Reynolds, R.A., Letsinger, R.L, Elghanian, R., Viswanadham, G., A Fluorescence-Based Method for Determining the Surface Coverage and Hybridization Efficiency of Thiol-Capped Oligonucleotides Bound to Gold Thin Films and Nanoparticles, *Anal. Chem., 72*, 5535 (2000).
21. Brayner, R., The Toxicology Impact of Nanoparticles, *Nanotoday, 3*, 48 (2008).
22. Wijaya, A., Schaffer, S.B., Pallares, I.G., Hamad-Schifferli, K., Selective Release of Multiple DNA Oligonucleotides from Gold Nanorods, *ACS Nano, 3*, 80 (2009).
23. Chen, C., Lin, Y., Wang, C., Tzeng, H., Wu, C., Chen, Y., Chen, C., Chen, L., Wu, Y., DNA-Gold Nanorod Conjugates for Remote Control of Localized Gene Expression by near Infrared Irradiation, *Journal of the Americal Chemical Society, 128*, 3709 (2006).
24. Braun, G. B., Pallaoro, A., Wu, G., Missirlis, D., Zasadzinski, J.A., Tirrell, M., Reich, N.O., Laser-Activated Gene Silencing via Gold Nanoshell-siRNA Conjugates, *ACS Nano, 3*, 2007 (2009).
25. Horiguchi, Y., Niidome, T., Yamada, S., Nakashima, N., Niidome, Y., Expression of Plasmid DNA Released from DNA Conjugates of Gold Nanorods, *Chemistry Letters, 36*, 952–953 (2007).
26. Takahashi, H., Niidome, Y., Yamada, S., Controlled Release of Plasmid DNA from Gold Nanorods Induced by Pulsed Near-Infrared Light, *Chem. Commun.*, 2247–2249 (2005).
27. Aguirre, C. M., Moran, C.E., Young, J.F., Halas, N.J., Laser-Induced Reshaping of Metallodielectric Nanoshells under Femtosecond and Nanosecond Plasmon Resonant Illumination, *J. Phys. Chem. B, 108*, 7040 (2004).
28. Rosi, N. L., Giljohann, D.A., Thaxton, C.S., Lytton-Jean, A.K.R., Han, M.S., Mirkin, C.A., Oligonucleotide-Modified Gold Nanoparticles for Intracellular Gene Regulation, *Science, 312*, 1027 (2006).
29. Troutman, T. S., Leung, S.J., Romanowski, M., Light-induced Content Release from Plasmon-resonant Liposomes, *Advanced Materials, 21*, 2334 (2009).
30. Wu, G., Mikhailovsky, A., Khant, H.A., Fu, C., Chiu, W., Zasadzinski, J.A., Remotely Triggered Liposome Release by Near-Infrared Light Absorption via Hollow Gold Nanoshells, *Journal of the American Chemical Society, 130*, 8175–8177 (2008).
31. Skirtach, A. G., Javier, A. M., Kreft, O., Kohler, K., Alberola, A. P., Mohwald, H., Parak, W. J., Sukhorukov, G. B., Laser-Induced Release of Encapsulated Materials inside Living Cells, *Angew. Chem. Int. Ed., 45*, 4612 –4617 (2006).

CHAPTER 2:
THEORETICAL BACKGROUND OF NANOPLASMONIC OPTICAL ANTENNAE

Nanoplasmonic optical antennae convert freely propagating electromagnetic energy into localized energy by utilizing the unique optical properties of metallic nanostructures. The understanding of the optical and photothermal properties of metallic nanostructures requires electrodynamics, solid-state, and heat transfer theory. Concepts from these disciplines are covered in this chapter; however, for a more in-depth review, the reader is directed to classical textbooks on electrodynamics by Griffiths (1) and by Bohren (2), solid-state physics by Kittel (3), and heat transfer by Ingropera and Dewitt (4) and by Carslaw and Jaeger (5).

A nanoplasmonic optical antenna receives, focuses, and transmits incoming optical and NIR electromagnetic radiation as an analogous, classical antenna receives, focuses, and transmits radio-frequency electromagnetic radiation. A nanoplasmonic optical antenna focuses incoming electromagnetic radiation down to dimensions smaller than the diffraction limit, otherwise known as the *antenna effect*, by coupling the incoming electromagnetic radiation to the localized excitation of conduction electrons at the conductor-dielectric interface of the nanoplasmonic optical antenna (Fig. 2.1). This antenna effect is prominent when the incoming electromagnetic radiation is matched to the plasmon resonance of the nanoplasmonic optical antenna, and as a result, the conduction electrons at the conductor-dielectric interface of the nanoplasmonic optical antenna collectively oscillate in phase on resonance.

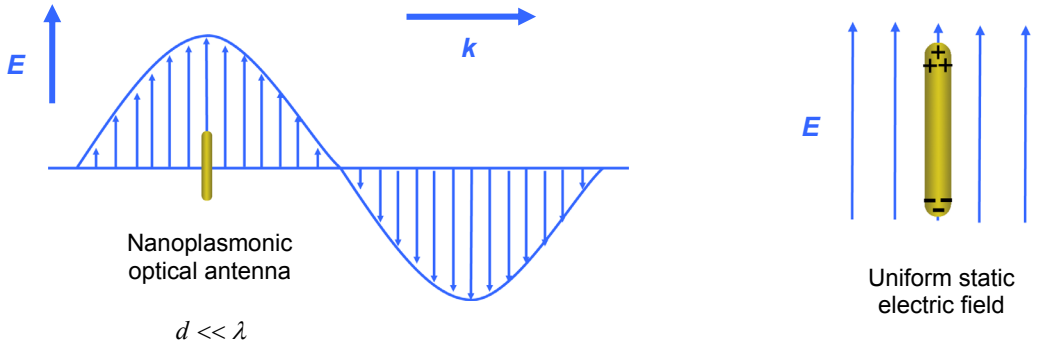

Figure 2.1. Antenna effect. When the diameter d of a nanoplasmonic optical antenna is much smaller than the wavelength λ of incoming electromagnetic radiation, the antenna is subject to a uniform static electric field. Under this condition, a nanoplasmonic optical antenna focuses incoming electromagnetic radiation (electric field *E*, wave vector *k*) down to dimensions smaller than the diffraction limit, otherwise known as the antenna effect, by coupling the incoming electromagnetic radiation to the localized excitation of conduction electrons at the conductor-dielectric interface of the nanoplasmonic optical antenna.

Quasi-static Theory for Rod-shaped Nanoplasmonic Optical Antennae

As a result of the antenna effect, nanoplasmonic optical antennae exhibit resonantly enhanced absorption and scattering properties that are useful for drug delivery, gene delivery, biomedical and spectroscopic imaging, and therapeutics. Among the nanoplasmonic optical antennae geometries, rod-shaped nanoplasmonic optical antennae, otherwise known as gold nanorods, are of widespread interest and pervasive use in the aforementioned applications due to their large absorption cross-section, facile tunability of the their plasmon resonance based on geometry, narrow spectral width of the longitudinal plasmon resonance band, and uniformly large-scale synthesis. Since it is subject to a uniform static electric field when its size is much smaller than the wavelength of the incoming electromagnetic radiation, a rod-shaped nanoplasmonic optical antenna exhibits resonantly enhanced absorption and scattering properties which can be mathematically described using the *quasi-static approximation* (1, 2, 6-8). Under this electrostatic condition, the Laplace equation for the potential is:

$$\nabla^2\Phi = 0$$

The solution to this Laplace equation for the potential can then be used to solve for the electric field:

$$\mathrm{E} = -\nabla\Phi$$

Here, a rod-shaped nanoplasmonic optical antenna is modeled as an ellipsoid:

$$\frac{x^2}{a^2} + \frac{y^2}{b^2} + \frac{z^2}{c^2} = 1$$

where c is the major axis, a and b are the minor axes of the ellipsoid, and $a = b$. In ellipsoidal coordinates (ξ, η, ζ), the equation becomes:

$$\frac{x^2}{a^2+\xi} + \frac{y^2}{b^2+\xi} + \frac{z^2}{c^2+\xi} = 1, \qquad -c^2 < \xi < \infty$$

$$\frac{x^2}{a^2+\eta} + \frac{y^2}{b^2+\eta} + \frac{z^2}{c^2+\eta} = 1, \qquad -b^2 < \eta < -c^2$$

$$\frac{x^2}{a^2+\zeta} + \frac{y^2}{b^2+\zeta} + \frac{z^2}{c^2+\zeta} = 1, \qquad -a^2 < \zeta < -b^2$$

The general solution for the potential is of the form:

$$\Phi(\xi,\eta,\zeta) = F(\xi)\left\{\left(c^2+\eta\right)\left(c^2+\zeta\right)\right\}^{1/2}$$

Due to the requirement that potentials remain finite at the origin, the solutions for the potentials Φ_{in} inside and Φ_{in} outside the antenna can be written as:

$$\Phi_{in}(\xi,\eta,\zeta) = C_1 F_1(\xi)\left\{\left(c^2+\eta\right)\left(c^2+\zeta\right)\right\}^{1/2}$$

$$\Phi_{out}(\xi,\eta,\zeta) = C_2 F_2(\xi)\left\{\left(c^2+\eta\right)\left(c^2+\zeta\right)\right\}^{1/2}$$

The coefficients C_1 and C_2 can be determined from the boundary conditions. Firstly, the potentials must be continuous at the boundary of the antenna:

$$\Phi_{in}(0,\eta,\zeta) = \Phi_0(0,\eta,\zeta) + \Phi_{out}(0,\eta,\zeta)$$

Secondly, there must be continuity of the normal component of the displacement field at the boundary between the antenna and the medium:

$$\varepsilon \frac{d\Phi_{in}}{d\xi} = \varepsilon_m \frac{d\Phi_0}{d\xi} + \varepsilon_m \frac{d\Phi_{out}}{d\xi} \qquad (\xi = 0)$$

Therefore, the potentials inside Φ_{in} and outside Φ_{out} the antenna are:

$$\Phi_{in} = \frac{\Phi_0}{1 + \frac{L(\varepsilon - \varepsilon_m)}{\varepsilon_m}}$$

$$\Phi_{out} = \Phi_0 \frac{\frac{abc}{2}\frac{\varepsilon_m - \varepsilon}{\varepsilon_m}\int_{\xi}^{\infty} \frac{dq}{(c^2+q)f(q)}}{1 + \frac{L(\varepsilon - \varepsilon_m)}{\varepsilon_m}} \approx \frac{E_0 \cos\theta}{r^2} \frac{\frac{abc}{3}\frac{\varepsilon - \varepsilon_m}{\varepsilon_m}}{1 + \frac{L(\varepsilon - \varepsilon_m)}{\varepsilon_m}}, \qquad (r >> a)$$

where

$$L = \frac{1-e^2}{e^2}\left(-1 + \frac{1}{2e}\ln\frac{1+e}{1-e}\right)$$

and

$$e^2 = 1 - \frac{a^2}{c^2}$$

The potential Φ_{out} outside the antenna can then be re-written to introduce the dipole moment $\mathbf{p}$:

$$\mathbf{p} = 4\pi\varepsilon_m abc \frac{\varepsilon - \varepsilon_m}{3\varepsilon_m + 3L(\varepsilon - \varepsilon_m)}\mathrm{E}_0$$

Therefore, when the incoming electromagnetic radiation travels along the *x*-axis, the applied field is parallel to the *z*-axis and the polarizability α is:

$$\alpha = 4\pi abc \frac{\varepsilon - \varepsilon_m}{3\varepsilon_m + 3L(\varepsilon + \varepsilon_m)}$$

Similarly, when the electromagnetic radiation travels along the *z*-axis and the applied field is parallel to either the *x*-axis or the *y*-axis, the respective polarizabilities α_1 and α_2 are:

$$\alpha_1 = 4\pi abc \frac{\varepsilon - \varepsilon_m}{3\varepsilon_m + 3L_1(\varepsilon + \varepsilon_m)}$$

$$\alpha_2 = 4\pi abc \frac{\varepsilon - \varepsilon_m}{3\varepsilon_m + 3L_2(\varepsilon + \varepsilon_m)}$$

where

$$L_1 = L_2 = \frac{1}{2}(1 - L)$$

Since no known alignment mechanism is used to intentionally align the rod-shaped nanoplasmonic optical antennae, it can be reasonably assumed that rod-shaped nanoplasmonic optical antennae are randomly oriented. Therefore, the overall

polarizability $\overline{\alpha}$ is equal to the average of the polarizabilities α, α_1, and α_2 in the three principle orientations is:

$$\overline{\alpha} = \frac{1}{3}(\alpha + \alpha_1 + \alpha_2)$$

Finally, the absorption cross-section C_{abs} and the scattering cross-section C_{sca} can be written as:

$$C_{abs} = k\,\mathrm{Im}(\overline{\alpha})$$

$$C_{sca} = \frac{k^4}{6\pi}|\overline{\alpha}|^2$$

Dual Functions of Nanoplasmonic Optical Antennae

When nanoplasmonic optical antennae are geometrically designed such that their absorption cross-section C_{abs} dominates over their scattering cross-section C_{sca}, the antenna effect can be utilized to efficiently convert absorbed light energy into surface-localized heat, otherwise known as *photothermal conversion* (9-11). Here, when the incoming electromagnetic radiation is coupled to the localized excitations of conduction electrons at the conductor-dielectric interface of the nanoplasmonic optical antenna, these conduction electrons are excited from the ground (unexcited) state (Fig. 2.2a). Treating the electrons and the lattice as two coupled systems (11), energy is then transferred from the excited conduction electrons to the lattice through electron-phonon collisions. As the system relaxes back to the ground state, the absorbed energy is finally dissipated as heat through phonon-phonon interactions. This photothermally generated heat transfer from the surface of the antenna to the surrounding cellular environment is highly localized, decaying exponentially within a few nanometers (9, 12, 13) and therefore is thought to have minimal adverse effects on cells. Additionally, the plasmon resonance of the nanoplasmonic optical antenna is also tuned to the NIR during fabrication, since tissues and cells are essentially transparent in the NIR wavelength regime (14). Nanoplasmonic optical antennae, serving as nanoplasmonic gene switches, utilize photothermally generated heat to liberate surface-bound cargo, such as single-stranded DNA (12, 15-17), short interfering RNA (siRNA) (18), or plasmid DNA (19-21), in a highly localized manner.

Alternatively, nanoplasmonic optical antennae can be geometrically designed such that their scattering cross-section C_{sca} dominates over their absorption cross-section C_{abs}. The geometry and structure can also be specifically designed to substantially enhance the antenna effect by utilizing the plasmon coupling between closely positioned geometrical features of the antenna and the lightning rod effect (22) at sharp geometrical features of the antenna. Therefore, when the incoming electromagnetic radiation is coupled to the localized excitations of conduction electrons at the conductor-dielectric interface of the nanoplasmonic optical antenna, intense scattered radiation is generated. Molecules in proximity undergo a momentary transition from the ground state to a virtual state (Fig. 2.2b). Transitions are related to the biochemical composition.

Enhanced Raman scattering, utilized in surface-enhanced Raman spectroscopy (SERS) (23-31), results when the transition is immediately to a vibrational level of the ground state. Enhanced Rayleigh scattering, utilized in plasmon resonance energy transfer (PRET) (32-34), results when the transition is immediately back to the ground state. In this way, nanoplasmonic optical antennae serve here as biosensors to enable a highly sensitive and label-free spectral readout of the biochemical composition in the local environment.

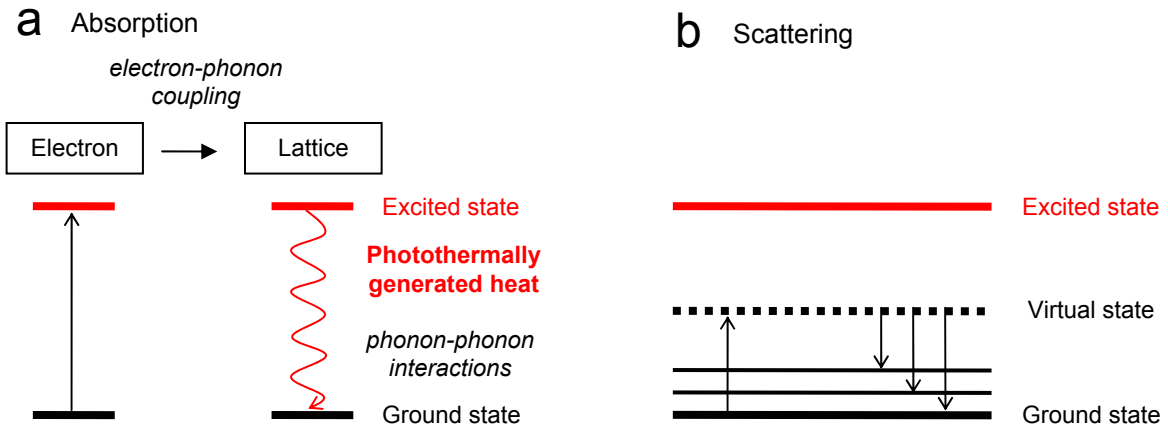

Figure 2.2. Dual functions of nanoplasmonic optical antennae. (a) Nanoplasmonic gene switches are geometrically designed such that their absorption cross-section dominates over their scattering cross-section. Therefore, when the incoming electromagnetic radiation is coupled to the localized excitations of conduction electrons, these conduction electrons are excited from the ground (unexcited) state. Energy is then transferred from the excited conduction electrons to the lattice through electron-phonon collisions. As the system relaxes back to the ground state, the absorbed energy is finally dissipated as heat through phonon-phonon interactions. **(b)** Biosensors are designed such that their scattering cross-section dominates over their absorption cross-section. Therefore, when the incoming electromagnetic radiation is coupled to the localized excitations of conduction electrons, a momentary transition from the ground state to a virtual state occurs. Enhanced Raman scattering, results when the transition is immediately to a vibrational level of the ground state. Enhanced Rayleigh scattering results when the transition is immediately back to the ground state.

Heat Transfer Theory

To minimize adverse effect on cells, it is critical that the photothermally generated heat transfer from the surface of the nanoplasmonic optical antenna to the surrounding cellular environment is highly localized. A nanoplasmonic optical antenna (radius 25 nm) internalized in a cell (radius 10 μm) can be modeled as a point source of heat based on its dimensions relative to the cell's dimensions. It can be reasonably assumed that radiative effects are negligible since radiative heat transfer scales with temperature T^4 and, in this case, low temperatures (<70°C) are utilized for on-demand liberation of surface-bound cargo. It is also assumed that convective effects are negligible since convective heat transfer occurs through a gas or liquid and, in this case, the cell cytoplasm is assumed to be more of a gelatinous material. Therefore, the main

mode of heat transfer is heat conduction from this point source of heat (5). The derivation begins with the general form of the conservation of energy (4) is:

$$\dot{E}_{in} + \dot{E}_g - \dot{E}_{out} = \dot{E}_{stored}$$

The energy inflow $\dot{E}_{in}$ is described by the heat conduction rates q_x, q_y, and q_z in the x. y and z directions, respectively:

$$\dot{E}_{in} = q_x + q_y + q_z$$

The energy generation $\dot{E}_g$ is described by the rate of thermal energy generation:

$$\dot{E}_g = \dot{q}dxdydz$$

The energy outflow $\dot{E}_{out}$ is expressed as:

$$\dot{E}_{out} = q_{x+dx} + q_{y+dy} + q_{z+dz}$$

The energy stored $\dot{E}_{stored}$ is expressed as:

$$\dot{E}_{stored} = \rho c_p \frac{dT}{dt} dxdydz$$

where ρ is the density and c_p is the specific heat. Therefore, the conservation of energy equation can be re-written as:

$$\left(q_x + q_y + q_z\right) + \left(\dot{q}dxdydz\right) - \left(q_{x+dx} + q_{y+dy} + q_{z+dz}\right) = \left(\rho c_p \frac{dT}{dt} dxdydz\right)$$

The heat conduction rates q_x, q_y, and q_z are expressed as:

$$q_x = -kdydz\frac{dT}{dx}$$

$$q_y = -kdxdz\frac{dT}{dy}$$

$$q_z = -kdxdy\frac{dT}{dz}$$

where k is the thermal conductivity. Substituting in these equations, the conservation of energy equation can then be re-written as:

$$\frac{d}{dx}\left(k\frac{dT}{dx}\right) + \frac{d}{dy}\left(k\frac{dT}{dy}\right) + \frac{d}{dz}\left(k\frac{dT}{dz}\right) + \dot{q} = \rho c_p \frac{dT}{dt}$$

Assuming the thermal conductivity remains constant:

$$\frac{d^2T}{dx^2} + \frac{d^2T}{dy^2} + \frac{d^2T}{dz^2} + \frac{\dot{q}}{k} = \frac{1}{\alpha}\frac{dT}{dt}$$

Assuming there is no internal mechanism for heat generation within the system:

$$\frac{d^2T}{dx^2} + \frac{d^2T}{dy^2} + \frac{d^2T}{dz^2} = \frac{1}{\alpha}\frac{dT}{dt}$$

Therefore, the solution for T is:

$$T = \frac{Q}{8\left(\pi kt\right)^{3/2}} e^{-\left((x-x')^2+(y-y')^2+(z-z')^2\right)/4kt} = \frac{Q}{8\left(\pi kt\right)^{3/2}} e^{-r^2/4kt}$$

The temperature over time can be obtained by integrating over time:

$$T - T_0 = \frac{1}{8(\pi kt)^{3/2}} \int_0^t Q e^{-r^2/4k(t-t')} \frac{dt'}{(t-t')^{3/2}}$$

$$T - T_0 = \frac{Q}{4\pi kr} erfc \frac{r}{\sqrt{4kt}}$$

$$T - T_0 = \frac{C_{abs} I}{4\pi kr} erfc \frac{r}{\sqrt{4kt}}$$

where C_{abs} is the absorption cross-section and I is the light intensity. Using cargo liberation temperature of 70°C, antenna radius of 25 nm, thermal conductivity of 0.5 W/m*K for gelatin (35), exposure time of 30 sec, and light power of 80 mW, the temperature distribution from the surface of the nanoplasmonic optical antenna is shown in graphical form in Figure 2.3a. An important observation from this graph is that the temperature returns back to 37°C within 20 nm, indicating that photothermally generated heat transfer from the surface of the antenna to the surrounding cellular environment is highly localized.

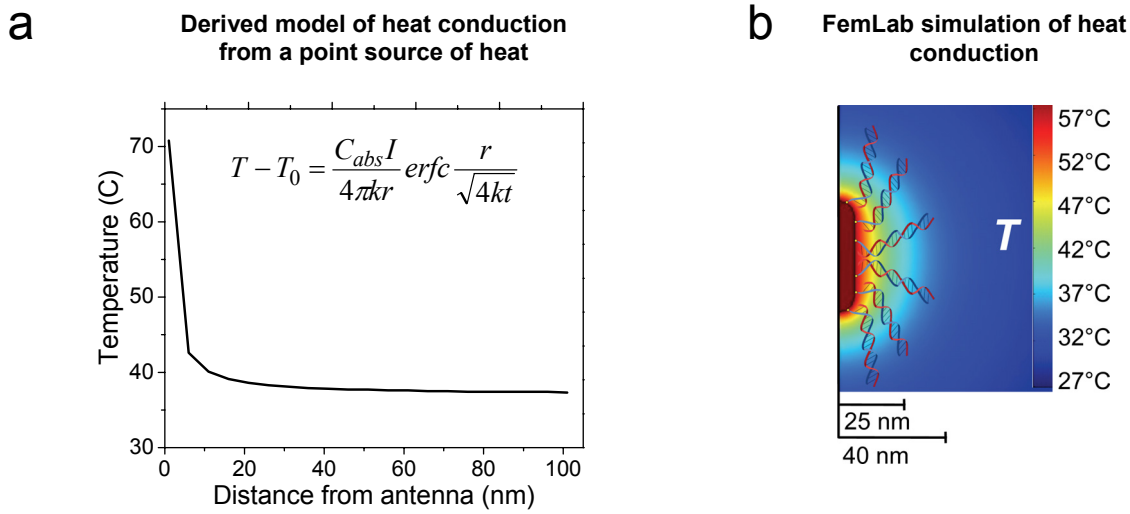

Figure 2.3. Temperature distribution from the surface of the nanoplasmonic optical antenna. (a) Localized heat distribution from the surface of the nanoplasmonic optical antenna is modeled as heat conduction from a point source of heat. **(b)** Axisymmetric FemLab simulation also demonstrating localized heat distribution at the nanoplasmonic optical antenna's surface at steady-state.

Additionally, FEMLab software can also be used to simulate an axisymmetric model of the heat distribution of a single nanoplasmonic optical antenna at steady-state (Fig. 2 3b). Fig. 2.3b shows the temperature distribution as a function of distance from the surface of the nanoplasmonic optical antenna. From the surface outwards, the temperature profile begins at the dehybridization temperature of short double-stranded oligonucleotides and falls off exponentially to 37ºC within 20 nm from the surface of the nanoplasmonic optical antenna. This further demonstrates that the photothermally generated heat is highly localized to the surface and should not propagate significantly

within the intracellular environment. Thus, we expect cell viability will remain uncompromised after light illumination.

References

1. Griffiths, D. J., *Introduction to Electrodynamics*, Prentice-Hall International, Inc., Upper Saddle River, NJ (1999).
2. Bohren, C. F., Huffman, D.R., *Absorption and Scattering of Light by Small Particles*, John Wiley & Sons, Inc., New York, NY (1983).
3. Kittel, C., *Introduction to Solid State Physics*, John Wiley& Sons, Inc. (2005).
4. Incropera, F. P., DeWitt, D.P., *Fundamentals of Heat and Mass Transfer*, John Wiley & Sons, Inc. (2002).
5. Carslaw, H. S., Jaeger, J.C., *Conduction of Heat in Solids*, Oxford University Press (1959).
6. Zhu, J., Huang, L., Zhao, J., Wang, Y., Zhao, Y., Hao, L., Lu, Y., Shape dependent resonance light scattering properties of gold nanorods, *Materials Science and Engineering B, 121*, 199 (2005).
7. Zhu, J., Li, J., Zhao, J., Bai, S., Light absorption efficiencies of gold nanoellipsoid at different resonance frequency, *J. Mater Sci, 43*, 5199 (2008).
8. Maier, S. A., *Plasmonics: Fundamentals and Applications*, Springer Science+Business Media LLC, New York, NY (2007).
9. Cortie, M., Xu, X., Chowdhury, H., Zareie, H., Smith, G., Plasmonic Heating of Gold Nanoparticles and Its Exploitation, *Proc. SPIE, 5649*, 565–573 (2005).
10. Khlebtsov, B., Zharov, V., Melnikov, A., Tuchin, V., Khlebtsov, N., Optical Amplification of Photothermal Therapy with Gold Nanoparticles and Nanoclusters, *Nanotechnology, 17*, 5167–5179 (2006).
11. Link, S., El-Sayed, M., Shape and Size Dependence of Radiative, Non-Radiative and Photothermal Properties of Gold Nanocrystals, *Int. Reviews in Physical Chemistry, 19*, 409 (2000).
12. Lee, S. E., Liu, G. L., Kim, F., Lee, L. P., Remote Optical Switch for Localized and Selective Control of Gene Interference, *Nanoletters, 9*, 562 (2009).
13. Skirtach, A. G., Dejugnat, C., Braun, D., Susha, A.S., Rogach, A.L., Parak, W.J., Mohwald, H., Sukhorukov, G.B., The Role of Metal Nanoparticles in Remote Release of Encapsulated Materials, *Nanoletters, 5*, 1371 (2005).
14. Svoboda, K., Biological Applications of Optical Forces, *Annu. Rev. Biophys. Biomol. Struct., 23*, 247 (1994).
15. Barhoumi, A., Huschka, R., Bardhana, R., Knight, M.W., Halas, N.J., Light-Induced Release of DNA from Plasmon-Resonant Nanoparticles: Towards Light-Controlled Gene Therapy, *Chemical Physics Letters, 482*, 171 (2009).
16. Jones, M. R., Millstone, J.E., Giljohann, D.A., Seferos, D.S., Young, K.L., Mirkin, C.A., Plasmonically Controlled Nucleic Acid Dehybridization with Gold Nanoprisms, *ChemPhysChem, 10*, 1461 (2009).
17. Wijaya, A., Schaffer, S.B., Pallares, I.G., Hamad-Schifferli, K., Selective Release of Multiple DNA Oligonucleotides from Gold Nanorods, *ACS Nano, 3*, 80 (2009).

18. Braun, G. B., Pallaoro, A., Wu, G., Missirlis, D., Zasadzinski, J.A., Tirrell, M., Reich, N.O., Laser-Activated Gene Silencing via Gold Nanoshell-siRNA Conjugates, *ACS Nano, 3*, 2007 (2009).
19. Horiguchi, Y., Niidome, T., Yamada, S., Nakashima, N., Niidome, Y., Expression of Plasmid DNA Released from DNA Conjugates of Gold Nanorods, *Chemistry Letters, 36*, 952–953 (2007).
20. Takahashi, H., Niidome, Y., Yamada, S., Controlled Release of Plasmid DNA from Gold Nanorods Induced by Pulsed Near-Infrared Light, *Chem. Commun.*, 2247–2249 (2005).
21. Chen, C., Lin, Y., Wang, C., Tzeng, H., Wu, C., Chen, Y., Chen, C., Chen, L., Wu, Y., DNA-Gold Nanorod Conjugates for Remote Control of Localized Gene Expression by near Infrared Irradiation, *Journal of the Americal Chemical Society, 128*, 3709 (2006).
22. Gersten, J., Electromagnetic Theory of Enhanced Raman Scattering by Molecules Adsorbed on Rough Surfaces, *J. Chem. Phys., 73*, 3023 (1980).
23. Nikoobakht, B., Wang, J., El-Sayed, M. A., Surface-enhanced Raman Scattering of Molecules Adsorbed on Gold Nanorods: Off-Surface Plasmon Resonance Condition, *Chemical Physics Letters, 366*, 17–23 (2002).
24. Nie, S., Emory, S.R., Probing Single Molecules and Single Nanoparticles by Surface-Enhanced Raman Scattering, *Science, 275*, 1102 (1997).
25. Willets, K. A., Van Duyne, R.P., Localized Surface Plasmon Resonance Spectroscopy and Sensing, *Annu. Rev. Phys. Chem., 58*, 267–297 (2007).
26. Liu, G. L., Lu, Y., Kim, J., Doll, J.C., Lee, L.P., Magnetic Nanocrescents as Controllable Surface-enhanced Raman Scattering Nanoprobes for Biomolecular Imaging, *Advanced Materials, 17*, 2683 (2005).
27. Lu, Y., Liu, G.L., Kim, J., Mejia, Y.X., Lee, L.P., Nanophotonic Crescent Moon Structures with Sharp Edge for Ultrasensitive Biomolecular Detection by Local Electromagnetic Field Enhancement Effect, *Nanoletters, 5*, 119 (2005).
28. Kniepp, K., Kniepp, H., Itzkan, I., Dasari, R.R., Feld, M.S., Ultrasensitive Chemical Analysis by Raman Spectroscopy, *Chem. Rev., 99*, 2957 (1999).
29. Jackson, J. B., Halas, N.J., Surface-enhanced Raman Scattering on Tunable Plasmonic Nanoparticle Substrates, *Proceedings of the National Academy of Sciences, 101*, 17930–17935 (2004).
30. Cho, H., Lee, B., Liu, G.L., Agarwal, A., Lee, L.P., Label-free and Highly Sensitive Biomolecular Detection using SERS and Electrokinetic Preconcentration, *Lab Chip, 9*, 3360–3363 (2009).
31. Choi, D., Kang, T., Cho, H., Choi, Y., Lee, L.P., Additional Amplifications of SERS via an Optofluidic CD-based Platform, *Lab Chip, 9*, 239 (2009).
32. Liu, G. L., Long, Y., Choi, Y., Kang, T., Lee, L.P., Quantized Plasmon Quenching Dips Nanospectroscopy via Plasmon Resonance Energy Transfer, *Nature Methods, 4*, 1015 (2007).
33. Choi, Y., Park, Y., Kang, T., Lee, L.P., Selective and Sensitive Detection of Metal Ions by Plasmon Resonance Energy Transfer-based Nanospectroscopy, *Nature Nanotechnology, 4*, 742 (2009).

34. Choi, Y., Kang, T., Lee, L.P., Plasmon Resonance Energy Transfer (PRET)-based Molecular Imaging of Cytochrome c in Living Cells, *Nanoletters, 9*, 85 (2009).
35. Sakiyama, T., Yano, T., Effects of Air and Water Contents on the Effective Thermal Conductivity of Air-impregnated Gels, *Agric. Biol. Chem., 54*, 1375 (1990).

CHAPTER 3:
NANOPLASMONICS-ENABLED ON-DEMAND GENE SILENCING: ANTISENSE DNA APPROACH

Precise spatiotemporal control of gene silencing in living cells is in critical demand (1, 2) for dynamically studying cellular signaling pathways (3), quantitative cell biology (4), systems biology (5), and molecular cell biology (6). In order to advance these dynamic cellular studies, nanoscale intracellular transmitter and receiver systems (ie. nanoplasmonic optical antennae) are required for the remote manipulation of biological systems. Remote electronic control of DNA hybridization by inductive coupling of a radio-frequency (7), photo-uncaging of DNA by UV light (8-10), and chromophore-based optical activation (11, 12) of biomolecules has previously been demonstrated. Enzymes (13) and thermo-responsive polymers (14) have also been used to release biomolecules from carriers. Additionally, photothermal melting of carriers has previously been used to release large plasmids from carriers (15, 16). High energies have also been utilized in photothermal therapies to destroy cells-of-interest (17-19). However, on-demand gene silencing with precise spatiotemporal resolution, minimal photo-damage, as well as the selective coupling of the optical transmission frequencies to different nanoplasmonic optical antennae has not yet been accomplished.

In this chapter, nanoplasmonic optical antennae are utilized here as nanoplasmonic gene switches for on-demand gene silencing in living cells. The plasmon resonance of nanoplasmonic gene switches is specifically tuned to the NIR spectral region where cells and tissues are essentially transparent. Due to their extraordinarily large surface-to-volume ratio, nanoplasmonic gene switches are ideal carriers of interfering antisense DNA (Fig. 3.1a). Antisense DNA is a short single strand of DNA (15-50 bp) that is complementary to the mRNA corresponding to the gene-of-interest. Interfering antisense DNA enables direct, sequence-specific silencing of genes, but alone, lacks the temporal control necessary for precise manipulation. To enable on-demand control, duplexes of thiol-modified sense and unmodified antisense DNA cargo are covalently bound to carriers and internalized in living cells. While antisense DNA is attached to nanoplasmonic gene switches, its interfering functionality is inactivated. Using light illumination as a remote trigger to photothermally dehybridize antisense DNA and “activate” their functionality (Fig 3.1b), genes can be silenced on-demand (Fig. 3.1c). The unbound antisense DNA binds to a portion of the corresponding mature mRNA. Once the mRNA/antisense DNA heteroduplex is formed, it is recognized and degraded by RNase H enzymes in the cytosol, thereby silencing the gene-of-interest (Fig. 3.1c). Since RNase H, is ubiquitously present in both the cytosol and the nucleus (20, 21), an alternative model (20) suggests that unbound antisense DNA transports to the nucleus. In the nucleus, the antisense DNA binds to the premature mRNA. Once this heteroduplex is formed, it is recognized and degraded by nuclear RNase H enzymes (Fig. 3.1d).

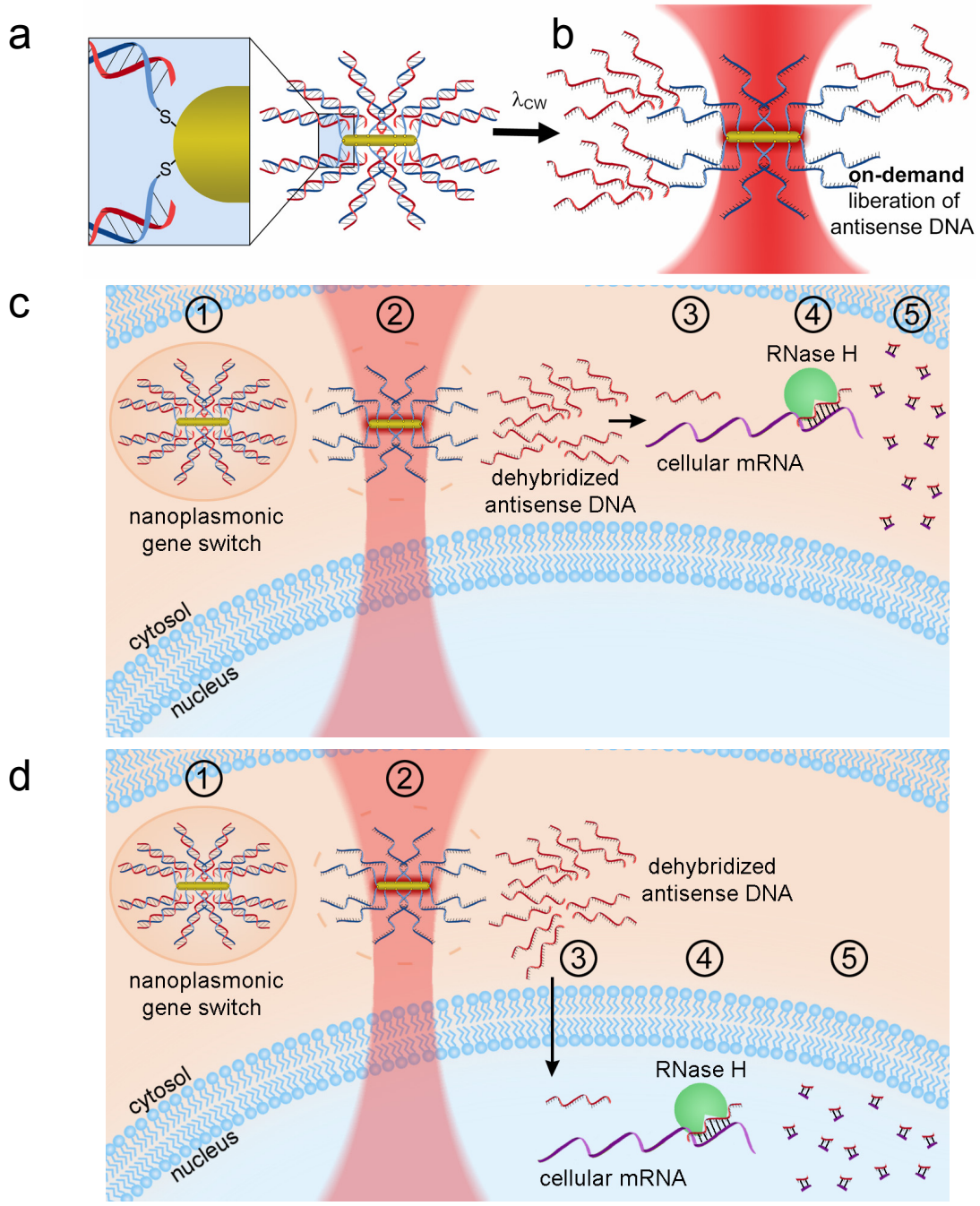

Figure 3.1. Nanoplasmonics-enabled on-demand gene silencing using antisense DNA. (a) Duplexes of thiol-modified sense and antisense DNA covalently bound to the gold nanorod. **(b)** In the presence of continuous-wave illumination, the antisense DNA strands dehybridize while the thiol-modified sense strands remain attached. **(c)** On-demand gene silencing using antisense DNA: Step 1 – duplexes are covalently bound to gold nanorods and internalized in cells. Step 2 - in the presence of illumination, antisense DNA strands dehybridize and release into the cytosol. Step 3 - unbound antisense DNA binds to a portion of the mature mRNA. Step 4 - mRNA/antisense DNA heteroduplex is recognized by RNase H enzymes. Step 5 - RNase H degrade the heteroduplex, thereby silencing the gene-of-interest. **(d)** Alternative model: Step 1 and step 2 are the same. Step 3 - unbound antisense DNA transports to the nucleus and binds to the premature mRNA. Step 4 - heteroduplex is formed and recognized by RNase H. Step 5 – heteroduplex is degraded by nuclear RNase H enzymes, thereby silencing the gene-of-interest.

Methods

Preparation of antisense DNA-conjugated gold nanorods. Gold nanorods with aspect ratio of 3.5 (Fig. 3.2 b) were synthesized using a previously reported seed-mediated growth method (22, 23). These switches were selected because of the maximum light absorbance at a wavelength in the NIR range of interest (785 nm). Phosphorothioate oligonucleotides sequences directed against the 5' region of the ERBB2 mRNA molecule were purchased from Integrated DNA Technologies (Coralville, IA). The sense sequence was 3'-GTGAGCACCATGGAG-5'-SH and the antisense sequence was 3' - CTCCATGGTGCTCAC-5'. Scrambled sense sequence 5' AAGAUCCAGUGGUAAUCUAC-3'-SH and antisense sequence 5' GUAGAUUACCACUGGAGUCUU-3' were used as control sequences. Unless otherwise specified, all sequences were purchased from Integrated DNA Technologies and all sequences were not labeled with dye. All thiolated oligonucleotides were reduced with dithiothreitol (Fisher Scientific) and were purified using NAP5 purification columns (GE Healthcare). To conjugate sense oligonucleotides to switches, 100 μL of 100 μM thiolated, sense oligonucleotides was incubated with 2000 μL of switches ($1x10^9$ particles/ml) and 40 μL of phosphate-buffered saline (PBS) on a rocker for 24 hours. The sense oligonucleotides attached to the switches through the thiol (-SH) group on the 5' end. To hybridize antisense oligonucleotides to the sense oligonucleotides, 100 μL of 100 μM antisense oligonucleotides were added to the switch-containing solution. This mixture was then heated for 2 minutes at 80˚C and then heated for 15 minutes at 65˚C. The mixture was finally incubated at room temperature on a rocker for 24 hours to ensure maximum hybridization. For use with cell culture, the conjugated switches were concentrated to $1x10^{14}$ particles/μL by centrifugation at 5000 rpm for 30 minutes, removal of the supernatant, and sonication for 1 minute to resuspend switches. The functionalized particles were then mixed with lipid complexes (Metafectene, Biontex) at a 3:1 ratio and allowed to incubate for 20 minutes, as suggested by manufacturer's instructions. The complexes were then added to cells and allowed to incubate for 12 hours. After 12 hours, the media was then exchanged back to normal media.

Surface immobilization of conjugated nanoplasmonic gene switches. TAMRA-modified (559 nm excitation/583 nm emission), phosphorothioate antisense oligonucleotides (TAMRA - 3' - CTCCATGGTGCTCAC-5') were used to visually monitor the photothermal dehybridization of antisense oligonucleotides from the switches. Conjugated switches were electrostatically attached to the glass slide. The solution containing switches was firstly dispensed onto the glass slide. Immediately after drying on the slide, the switches were re-immersed in buffer solutions. A few rounds of washing steps were also performed to remove free standing switches. When re-immersed in solution, the conjugated switches remain permanently attached to the glass surface.

Characterization of laser power, wavelength specificity, and temperature. A 785 nm laser (model APM50/1557, Power Technologies, Little Rock, AR) was positioned

above the sample. The laser spot size was 2 mm. An inverted microscope operating in epi-fluorescence mode was used to visualize photothermal dehybridization.

To characterize laser power, the power intensity was measured using an optical power meter (model 1830-C, Newport Corp, Irvine, CA). Immobilized switches with TAMRA-labeled antisense oligonucleotides were illuminated at three different power intensities: 4 mW/mm^2, 6 mW/mm^2, and 9 mW/mm^2 for 30 minutes. At 10 minute intervals, the fluorescence intensity of an area away from the conjugated switches was captured using a color CCD camera (Qfire, Olympus America, Inc.).

To characterize wavelength specificity, a 658 nm laser (model LM658-65C, Newport Corporation, Irvine, CA), outside the peak optical absorption, was also used in addition to the 785 nm laser. Immobilized switches with TAMRA-labeled antisense oligonucleotides were illuminated at the same power density of 9 mW/mm^2 for 30 minutes using each laser. At 10 minute intervals, the fluorescence intensity of an area away from the conjugated switches was captured using a color CCD camera (Qfire, Olympus America, Inc.). Matlab™ software was used to analyze the fluorescence intensity by integrating the signal over the area of the image. Various areas located at the same radial distance from the immobilized switches were measured to obtain statistical information (mean, standard deviation).

To characterize the temperature on the switches, three different lengths of oligonucleotides (15 bp, 25 bp, and 50 bp) with known melting temperatures (50ºC, 63ºC, and 70ºC respectively) were purchased: (15 bp sense) 5' – GTG AGC ACC ATG GAG - 3' SH, (15 bp antisense) 5'- CTC CAT GGT GCT CAC - 3' FAM, (25 bp sense) 5' - AAC CTC CTC GAA CCT CCT CGA ACC T - 3' SH, (25 bp antisense) 5' - AGG TTC GAG GAG GTT CGA GGA GGT T - 3' FAM, (50 bp sense) 5' - AAC CTC CTC GAA CCT CCT CGA ACC TAAC CTC CTC GAA CCT CCT CGA ACC T- 3' SH, and (50 bp antisense) 5' - AGG TTC GAG GAG GTT CGA GGA GGT TAGG TTC GAG GAG GTT CGA GGA GGT T- 3' FAM. Here, all the antisense strands were labeled with FAM dye (495 nm excitation/520 nm emission) on the 3' end to visually monitor the photothermal dehybridization of antisense oligonucleotides from the switches. To characterize the temperature, immobilized switches with different lengths of oligonucleotides were illuminated with 9 mW/mm^2 for 15 minutes. The fluorescence intensity of the conjugated switches was captured at 3 frames/sec using a color CCD camera (Qfire, Olympus America, Inc.).

Cell preparation. The human breast carcinoma line BT474 was purchased from the American Type Culture Collection (Rockville, MD). Cells were cultured in DMEM media supplemented with 10% heat-inactivated fetal bovine serum and were maintained in a 37˚C incubator with 5% CO_2 humidified air. Cells were initially seeded in either 6-well plate at a cell density of 400,000 cells/well (9.6 cm^2) or 96-well plates at 20,000 cells/well. The cells were allowed to plate for 24 hours prior to treatment with conjugated switches.

Experimental setup for localized photothermal dehybridization. To show highly localized photothermal dehybridization, a 785 nm laser was positioned above a sample using a micro-manipulated xyz stage (MP-285, Sutter Instrument Company). The laser was then focused to a 5 μm diameter spot size using a 4X objective lens located above the sample. An inverted microscope operating in epi-fluorescence mode was used to visualize photothermal dehybridization. Conjugated switches were illuminated using the focused laser at 9 mW/mm^2 for 2 minutes without illuminating other neighboring switches. Images were captured using a color CCD camera (Qfire, Olympus America, Inc.) before and after illumination.

For intracellular photothermal dehybridization, 10 μL of conjugated switches (1x10^{14} particles/μL) were internalized inside BT474 breast carcinoma cells (which were plated on glass coverslips in the 6-well plates) for 8 hours. The antisense strand was labeled with FAM fluorescent dye. After 8 hours, the coverslips containing cells were removed from the 6-well plate and were washed three times with 1X PBS. The coverslip containing cells was then placed on a microscope slide. Cured PDMS was used to form a well around the coverslip on the microscope slide. This well was then filled with media. Conjugated switches were illuminated using the focused laser at 9 mW/mm^2 for 2 minutes without illuminating other neighboring switches within a BT474 cell. Images were captured using a highly sensitive monochrome CCD camera (Cascade 512B, Photometrics) before and after illumination.

Experimental setup for conventional transfection of ERBB2 antisense DNA. Antisense DNA, complementary to ERBB2 mRNA (FAM - 3' - CTCCATGGTGCTCAC-5'), were transfected into BT474 cells using Fugene 6 (Roche Diagnostics) transfection reagent. Briefly, 10 μl of Fugene was mixed with 90 μl of Optimem media (Gibco) and incubated for 5 minutes at room temperature. Then 0.5 μg of antisense oligonucleotides was added to the Fugene/Optimem mixture and allowed to incubate for 20 minutes at room temperature. Finally, this solution was added to one wells of the 6-well plate containing BT474 cells and media. After 24 hours and 48 hours, the samples were prepared for flow cytometry analysis (described below).

Experimental setup for nanoplasmonics-enabled on-demand ERBB2 silencing. 10 μL of conjugated switches (1x10^{14} particles/μL) was added to each well of the 96-well plate. The BT474 cells were incubated for 24 hours at 37°C with the conjugated switches. After 24 hours, a 785 nm laser was positioned above a sample (spot size of the laser was 2 mm in diameter). The laser was used to illuminate the cells at 9 mW/mm^2 for 2 minutes. The cells were then incubated at 37°C for 48 hours.

Indirect immuno-fluorescence staining of ERBB2. Cells were washed three times with 1X PBS, fixed using 2% paraformaldehyde (15712-S, Electron Microscope Sciences, Hatfield, PA) for 10 minutes, and blocked with bovine serum albumin (15260-037, Invitrogen Corporation) for 30 minutes. The cells were then stained using mouse anti-ERBB2 (OP15T, Calbiochem) primary antibody (1:100 dilution) for 90 minutes and anti-mouse IgG (F5262-1ML, Sigma-Aldrich) secondary antibody conjugated with (1:128 dilution) FITC dye (488 nm excitation/518 nm emission) for 30 minutes.

Viability analysis. Cells were seeded in 6-well plates as explained in the cell preparation method above. After 24 hours, cells were incubated with 10 μL of concentrated switches ($1x10^{14}$ particles/μL) in 2 ml of Optimem media per well for 24 hours. After 24 hours, the cells were washed with 1X PBS and placed back in media. The laser was used to illuminate cells at 9 mW/mm^2 for 2 minutes. The cells were then incubated at 37°C for two days and five days.

Two days and five days later, the cells were prepared for analysis with flow cytometry. The cells were not fixed when they were analyzed. The cells were detached from the 6-well plates using 0.25% trypsin for 2 minutes, collected using centrifugation (1100 rpm, 8 minutes), and re-suspended in 1X PBS which contains 2μM Calcein AM. As a control, un-adhered dead cells were collected from the media in the 6-well plates and sonicated for 10 seconds. These dead cells are then collected using centrifugation (1100 rpm, 8 minutes), and re-suspended in 1X PBS which contains 2μM Calcein AM (Invitrogen) for 20 minutes. These samples were then immediately transferred to FACS tubes for flow cytometry analysis. Their fluorescence was analyzed by flow cytometry using the Coulter EPICS XL flow cytometer (Beckman Coulter Inc., Fullerton, CA) at an average flow rate of 500 cells/second. Flow cytometry profiles were analyzed using WinMDI software. To qualitatively view viability, cells were adhered onto glass-coverslips and prepared on-demand gene silencing in the same way as explained the above paragraph. Five days after illumination, the cells were washed in 1X PBS and incubated in 1X PBS containing 2 μM Calcein AM and 4 μM Ethidium homodimer (Invitrogen). The cells were imaged using DIC and fluorescence microscopy.

Flow cytometry analysis. For flow cytometry analysis, duplicate samples were made in the 96-well plates so that the total cell number per sample was approximately 500,000 cells. After treatment, the cells were washed three times with 1X PBS, detached from the cell culture dish using 1m M EDTA for 10 minutes, collected using centrifugation (1100 rpm, 8 minutes), and re-suspended in PBS containing 2% fetal bovine serum (16000-036, Invitrogen Corporation) and 0.1% sodium azide. The suspended cells were then stained for ERBB2 using 10 μl of mouse anti-ERBB2 conjugated with PE dye (340552, BD Biosciences) for 60 minutes in the dark. Cells in the isotype control were stained with mouse IgG1 conjugated with phycoerythrin (PE) dye (340761, BD Biosciences) to ensure no non-specific antibody binding took place. The suspended cells were finally fixed in 2% paraformaldehyde for 10 minutes and transferred to FACS tubes for flow cytometry analysis. Their fluorescence was analyzed by flow cytometry using the Coulter EPICS XL flow cytometer (Beckman Coulter Inc., Fullerton, CA) at an average flow rate of 500 cells/second. Flow cytometry profiles were analyzed using WinMDI software.

Results and Discussion

The first stage in demonstrating on-demand gene silencing was confirming the wavelength specificity for photothermal dehybridization. Duplex-conjugated switches were prepared as previously described (33, 34) and immobilized onto a glass surface. All the experiments were on based on permanently-attached switches. The antisense DNA was labeled with fluorescent dye to visually monitor their dehybridization using fluorescence microscopy. To demonstrate wavelength specificity, a laser at the peak optical absorption (785 nm) was compared to a laser outside the peak optical absorption (658 nm) for photothermal dehybridization. The entire viewing window was illuminated using each laser, positioned above the sample. An inverted microscope operating in epi-fluorescence mode was used to visualize photothermal dehybridization. Photothermal dehybridization was monitored by observing the fluorescence intensity of an area away from the conjugated switches. Initially, the normalized fluorescence intensity of this area was set to 0. When the temperature on the switch reached the melting temperature of the double-stranded oligonucleotides, the antisense strand was dehybridized and the fluorescence intensity in the observed area increased. Fig. 3.2e shows that the photothermal efficiency is two and a half times greater at the peak optical absorption wavelength.

To minimize laser exposure to cells, the minimal power necessary to achieve photothermal dehybridization was characterized. Conjugated switches, with fluorescently-labeled antisense strands, were immobilized onto a glass surface and a 785 nm laser was used to illuminate the switches at various power densities: 4 mW/mm^2, 6 mW/mm^2, and 9 mW/mm^2. Fig. 3.2f illustrates that the photothermal efficiency rises with increasing power densities.

In order to demonstrate on-demand gene silencing in living cells, it is important to confirm that the photothermally generated heat generated will not adversely affect cells. Heat transfer theory, in Chapter 2, theoretically verified that photothermally generated heat is highly localized to the surface of switches. In this chapter, the temperature on the surface of the switches is experimentally characterized. It was reasoned that if three different oligonucleotides of known length (15 bp, 25 bp, and 50 bp) with known melting temperatures (50ºC, 63ºC, and 70ºC respectively) are photothermally dehybridized, the temperature on the switches as a function of input energy can be correlated by visualizing their melting profiles. As seen in Figure 3.2c, when the temperature on the switches reaches the melting temperature of the oligonucleotides for each length, the fluorescent intensity decreases sharply, indicating that the antisense oligonucleotides have been released into solution. Using each profile, the energy required to reach each melting temperature is approximated by $E = \alpha P t$, where *E* is the energy in J/cm^2, α is the absorptivity of gold, *P* is the power of the laser in W/cm^2, and *t* is the time in seconds (shown in inset of Fig. 3.2c). Experimental characterization showed that melting temperatures as low as 50ºC required 2 mJ/cm^2 of energy and temperatures as high as 70 ºC required 5 mJ/cm^2 of energy. This demonstrates that low temperature activation can be achieved during illumination.

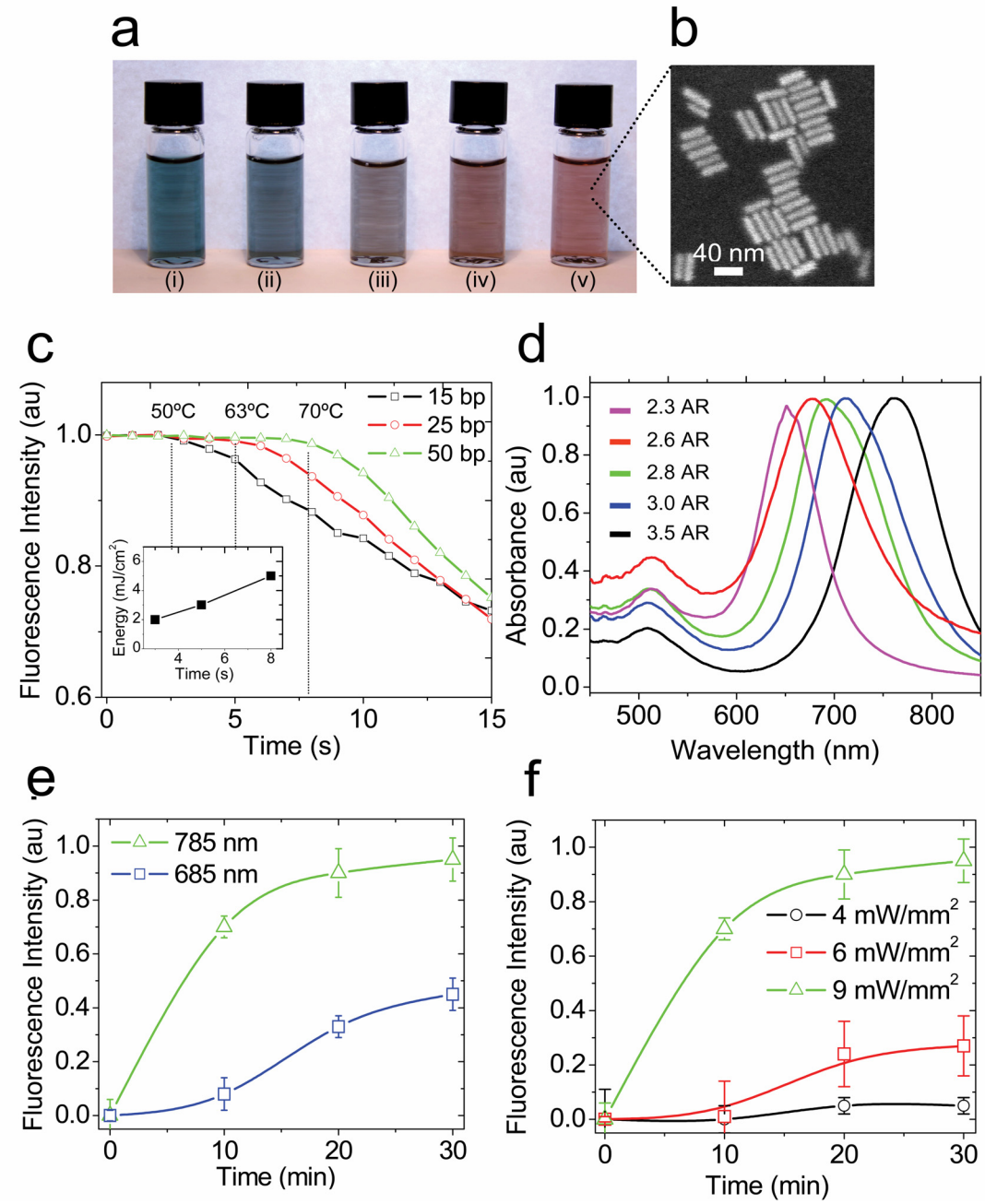

Figure 3.2. Experimental characterization of nanoplasmonic gene switches. (a) Tunable rod-shaped nanoplasmonic gene switches (ie. gold nanorods) based on different aspect ratios. Each solution of nanoplasmonic gene switches corresponds to a maximum absorbance (left to right): (i) 652nm, (ii) 676 nm, (iii) 694 nm, (iv) 715 nm , (v) 785 nm. **(b)** Scanning electron microscopy image showing the switches' aspect ratio (length/diameter) is 3.5. **(c)** Melting profiles for three different lengths of oligonucleotides (15 bp, 25 bp, and 50 bp) with known melting temperatures (50ºC, 63ºC, and 70ºC respectively). Antisense oligonucleotides are FAM-labeled. Temperature is correlated to input energy by analyzing their melting profiles. **(d)** Absorption spectrum of tunable rod-shaped nanoplasmonic gene switches based on different aspect ratios (A.R.): (i) 2.3 A.R.: 652nm, (ii) 2.6 A.R.: 676 nm, (iii) 2.8 A.R.: 694 nm, (iv) 3.0 A.R.: 715 nm , (v) 3.5 A.R.: 785 nm. **(e)** Fluorescence versus time plots comparing photothermal dehybridization for a laser at the peak optical absorption (785 nm) and a laser outside the peak optical absorption (658 nm). **(f)** Fluorescence versus time plots comparing photothermal dehybridization for various power densities.

As a qualitative test of localized photothermal dehybridization, spatially controlled photothermal dehybridization was performed both outside and inside of living cells. A NIR laser was focused to a 5 μm diameter spot size using an objective lens located above the sample. Using this focused NIR laser, certain immobilized switches (with fluorescently-labeled antisense oligonucleotides) were illuminated while other neighboring switches were not (Fig. 3.3). Upon illumination, the antisense oligonucleotides were photothermally dehybridized and the fluorescence intensity at the illuminated switches' locations vanished (Fig. 3.3b).

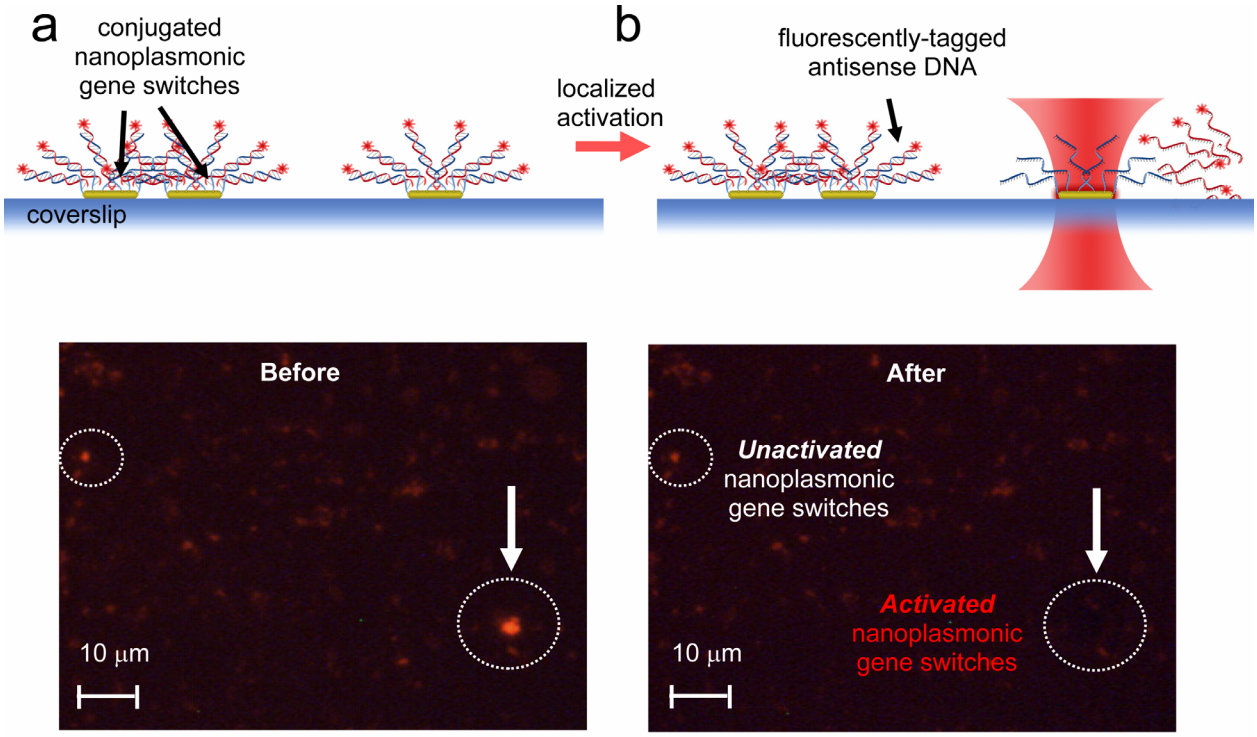

Figure 3.3. ***In vitro*** **demonstration of photothermal dehybridization.** Fluorescence is from the TAMRA-labeled antisense strand of the double-stranded oligonucleotides attached to immobilized nanoparticles on glass. **(a)** Concept and fluorescent images before illumination. **(b)** Concept and fluorescence images after illumination.

Having established that oligonucleotides can be released in a highly-localized manner, we investigated localized photothermal dehybridization within BT474 breast carcinoma cells. Switches functionalized with fluorescently-labeled antisense strands were encapsulated in commercially-available lipid complexes which undergo repulsive membrane acidolysis in a weakly acidic environment (24, 25). The complexes were then internalized within a population of cells via endocytosis. Once inside endosomes, the lipid complexes destabilized due to repulsive electrostatic forces generated in the weakly acidic endosomal environment, and finally, due to osmotic disruption, the endosomal membrane was broken. At this point, the functionalized switches were released into the cytosol. Alternatively, it was also possible that by photothermally heating switches inside endosomes, the endosomal membrane was disrupted and the contents were released from the endosomes (26-28). In Fig. 3.4d, the darkfield

scattering image of single switches is overlaid with a DAPI-stained nuclei image to demonstrate that single switches congregate in groups at the nuclear membrane. Using a highly-sensitive monochromatic camera, Fig. 3.4a shows fluorescing functionalized switches internalized within cells. Because of the diffraction limit, single, closely-congregated fluorescent switches cannot be distinguished and the switches groups therefore appear as fluorescent "patches" or spots around the nuclei. A surface plot of the fluorescent intensity is shown as an inset in Fig. 3.4a to clearly visualize each of the fluorescent "patches." Control experiments were carried out to verify that cells lacking the fluorescently-labeled antisense strands do not show similar fluorescence.

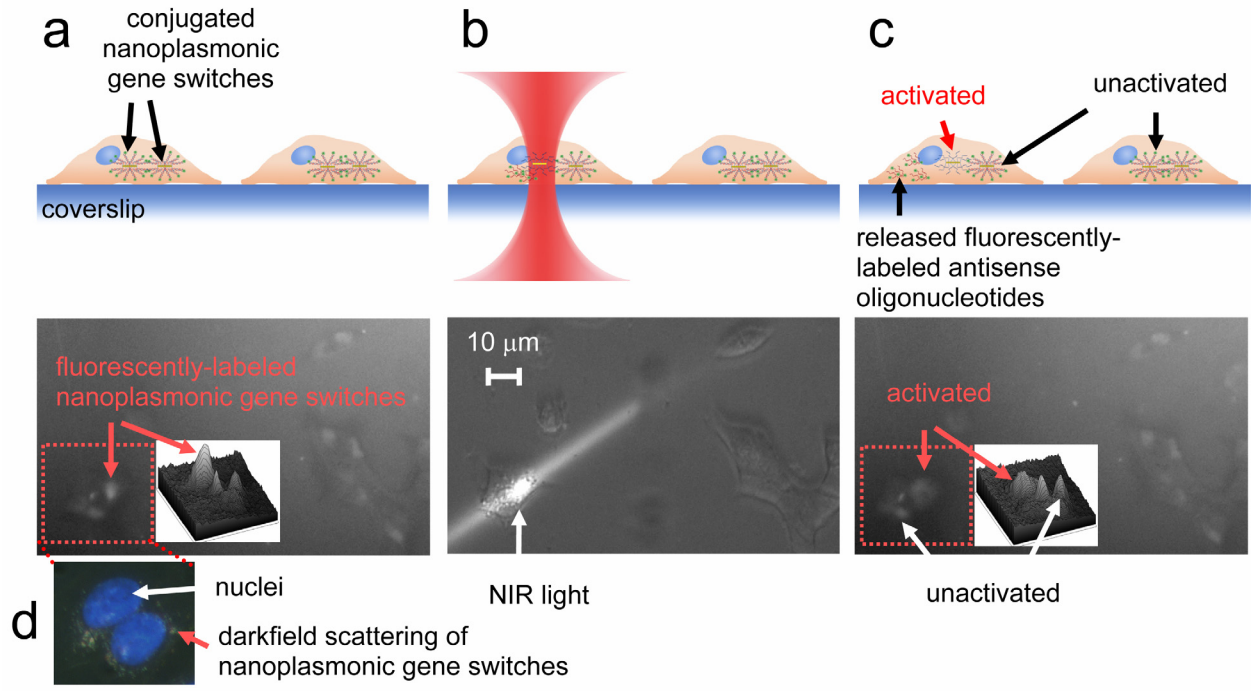

Figure 3.4. Visualization of intracellular photothermal dehybridization. Antisense oligonucleotides are FAM-labeled. **(a)** Concept and fluorescence images before illumination. Inset shows surface plot of fluorescence intensity of a cell (located on the left-hand side) before illumination. **(b)** Concept and brightfield image of localized NIR activation. **(c)** Concept and fluorescent images after photothermal dehybridization inside BT474 breast carcinoma cells. Inset shows surface plot of fluorescence intensity of a cell (located on the left-hand side) after illumination. **(d)** Darkfield scattering image of single switches is overlaid with a DAPI-stained nuclei image to demonstrate that single switches congregate in groups at the nuclear membrane.

To show localized, intracellular photothermal dehybridization, a focused NIR laser was used to illuminate a specific fluorescent patch within the cells (Fig. 3.4b). To insure that oligonucleotides were well-dispersed in the cells after photothermal dehybridization, the illumination time was chosen such that it was longer than the estimated diffusion time of the oligonucleotides. During illumination, no oligonucleotide back-binding of released oligonucleotides back onto the switches occurred due to the elevated temperature at the surface of the switches. The diffusion time was expected to be approximately 30 s, assuming the diffusion length was approximated by the diameter

of the cell (10^{-5}m) and the diffusion coefficient is $3x10^{12}$ m^2/s for a 100 bp oligonucleotide (29). Therefore, the cells were illuminated for 2 minutes at 9 mW/mm^2 to allow enough time for oligonucleotides to be well-dispersed in the cytoplasm.

Upon illumination, double-stranded oligonucleotides photothermally dehybridized and the labeled antisense strands diffused around the cytosol (Fig. 3.4c). A surface plot of the fluorescence intensity is shown as an inset in Fig. 3.4c to clearly demonstrate the decrease in intensity at the illuminated location while other surrounding fluorescent patches remain unaffected. The surface plot in Fig. 3.4c compared with the surface plot in Fig. 3.4a, shows that at the illuminated patch location, the maximum peak fluorescence intensity decreases and broadens out as the released fluorescently-labeled oligonucleotides slowly diffuse into the surrounding cytosol. Control experiments were carried out to confirm that change in fluorescence was not due to the movement of the switches themselves during illumination.

After validating steps essential to photothermal dehybridization, on-demand gene silencing of ERBB2, an oncoprotein commonly overexpressed in 20-30% of breast cancers (30), was carried out in breast carcinoma cells. As a conventional measure of gene silencing, a multi-component lipid-based transfection reagent was used to initially determine the optimal modulation of ERBB2 expression in BT474 breast carcinoma cells using interfering antisense oligonucleotides. General transfection methods, such as viral vectors or cationic liposome-mediated transfection, enable DNA to enter cells, but alone lack the spatiotemporal control of gene silencing. ERBB2 receptors were stained with fluorescently-labeled antibodies against ERBB2. Flow cytometry results show that there is no significant change in expression 24 hours after transfection (Fig. 3.5a). However, for 9.0% of transfected cells, the ERBB2 levels dropped below threshold after 48 hours (Fig. 3.5b).

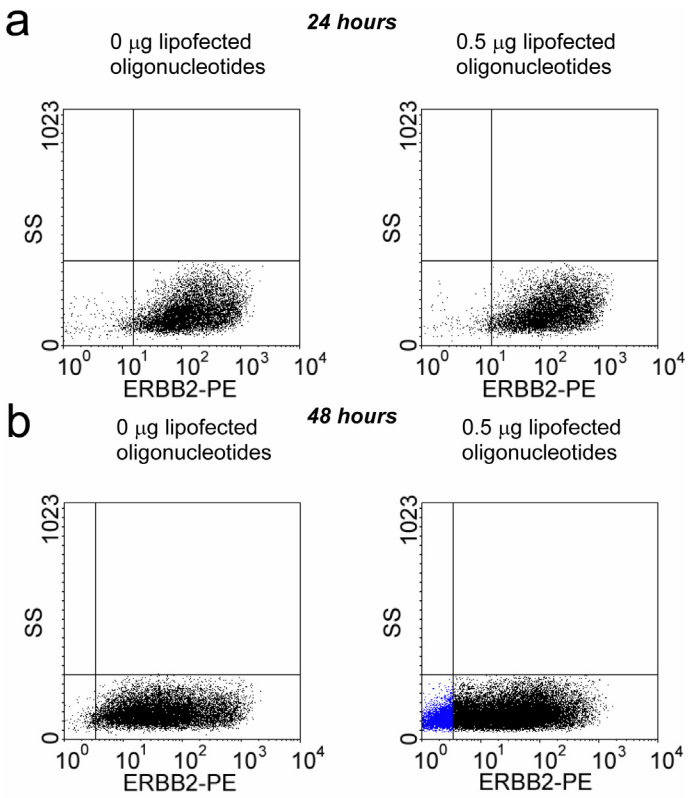

Figure 3.5. ERBB2 silencing by conventional transfection. Control cells contain no ERBB2 antisense DNA while treated cells contain ERBB2 antisense DNA. Flow cytometry used to analyze ERBB2 protein levels **(a)** 24 hours after transfection. **(b)** 48 hours after transfection.

After characterizing the experimental parameters for conventional gene silencing of ERBB2, on-demand gene silencing of ERBB2 was then conducted. Conjugated switches were internalized within cultured BT474 breast carcinoma cells. It has been suggested that there are between 168 and 336 ERBB2 molecules per cell (31). Since each switch was estimated to release approximately 250 molecules of oligonucleotides, a difference in expression should be expected since there should be enough released oligonucleotides to bind with ERBB2 mRNA. To initiate photothermal dehybridization, an unfocused NIR laser was used to illuminate an entire population of cells. The cells were then allowed to culture for 48 hours. Three control experiments were conducted to insure that photothermal dehybridization was the reason for gene silencing: unilluminated cells with conjugated switches (Fig. 3.6a), illuminated cells lacking switches (Fig. 3.6b), and illuminated cells with scrambled sequence-conjugated switches (Fig. 3.6c). On-demand gene silencing of ERBB2 resulted in a decrease in ERBB2 levels (Fig. 3.6d) while control cells expressed high ERBB2 levels (Fig. 3.6 a-c). All samples were stained with PE-labeled antibodies against ERBB2 and their fluorescence was analyzed by flow cytometry. The flow cytometric results (mean μ, coefficient of variation *CV*, % cells whose protein levels which have dropped below threshold) for all the samples are summarized in a table in Table 3.1. Table 3.1 shows that for 13.2% of the illuminated cells containing ERBB2-switches, the protein levels dropped below threshold. It is especially noteworthy to point out that the average

ERBB2 protein level of the entire cell population decreased by 55% after on-demand gene silencing. In Fig. 3.6, the average fluorescence intensity of the control, illuminated cells lacking switches, is 178.6 a.u. and the average fluorescence intensity of illuminated cells containing ERBB2-conjugated switches is 79.5 a.u. The average fluorescence intensity of the control, unilluminated cells containing switches, is 199.4 a.u. To qualitatively visualize ERBB2 silencing, cells were fixed and immunostained with fluorescently-labeled antibodies against the ERBB2 (Fig. 3.6c, 3.6d). The decrease in fluorescence in the cells containing ERBB2-conjugated switches versus the control sample indicates successful gene silencing of ERBB2 expression.

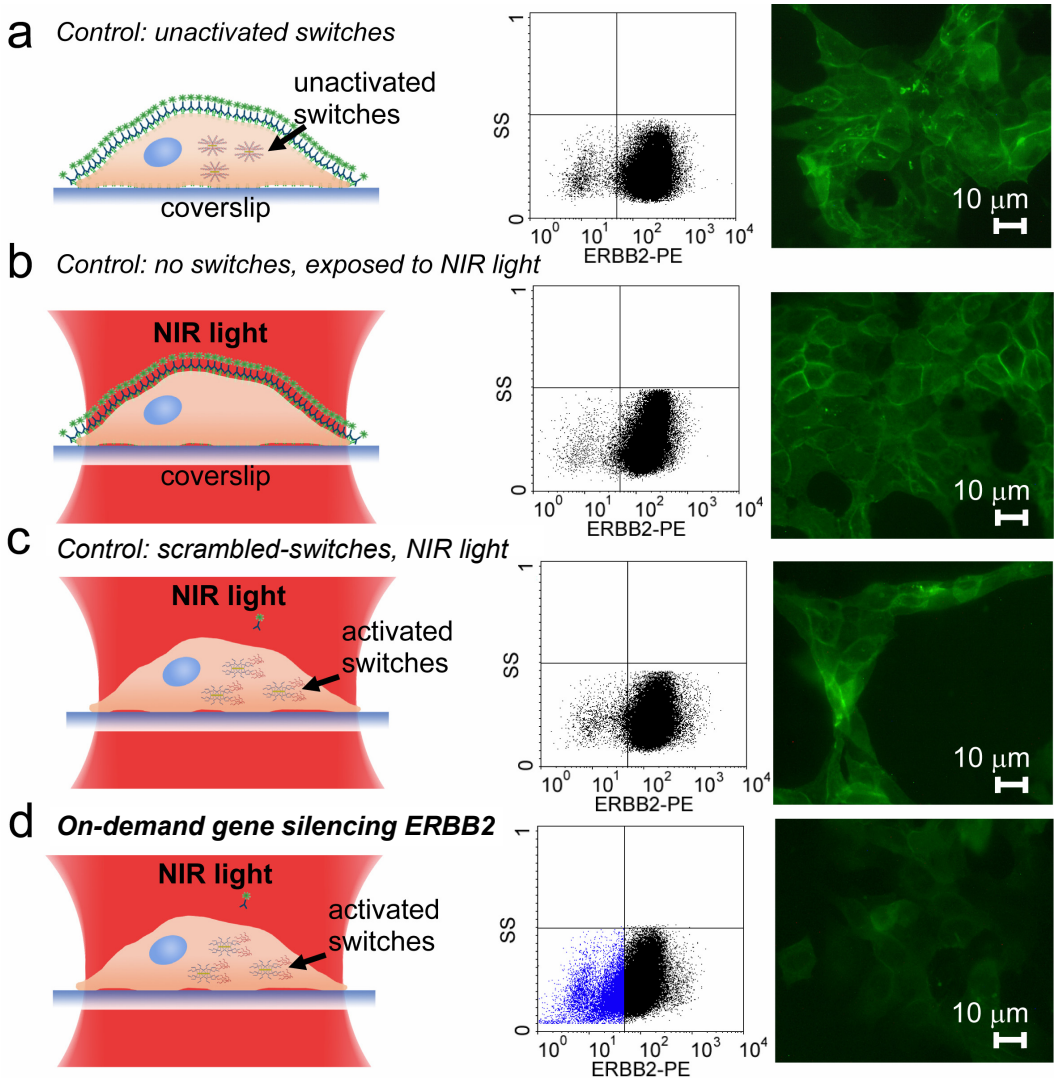

Figure 3.6. On-demand gene silencing of ERBB2 using antisense DNA. (a) Concept, flow cytometric results, and representative image of indirect immunofluorescent staining of ERBB2 after 48 hrs in control cells which have been treated with conjugated switches but have not been exposed to NIR light. **(b)** Concept, flow cytometric results, and representative image of indirect immunofluorescent staining of ERBB2 after 48 hours in control cells which do not contain conjugated switches but have been exposed to light. **(c)** Concept, flow cytometric results, and representative image of indirect immunofluorescent staining of ERBB2 in illuminated cells containing switches functionalized with scrambled sequences **(d)** Concept, flow cytometric results, and representative image of indirect immunofluorescent staining of ERBB2 after on-demand gene silencing of ERBB2 in BT474 breast carcinoma cells.

Sample	% cells below threshold	Mean, μ (a.u.)	*CV* (a.u.)
Control : ERBB2 switches,no NIR light	2.4	199.4	13.72
Control: no switches, NIR light	1.5	178.6	10.8
Control: scrambled-switches, NIR light	2.5	162.2	11.3
ERBB2-switches, NIR light	13.2	79.5	17.18

Table 3.1. Flow cytometry results. Table summarizing flow cytometric results by % of cells whose protein levels have dropped below threshold, average fluorescence intensity μ (a.u.), and coefficient of variation CV (a.u.).

Finally, viability of cells after illumination is crucial. Calcein AM, a dye which converts from nonfluorescent cell-permeant calcein AM into fluorescent calcein by intracellular esterase enzymes in living cells, is used as a measure of cell viability. Flow cytometry is used to analyze the samples 2 days and 5 days after activation. As a control for the Calcein AM dye, cells are intentionally killed using sonication and stained with calcein AM. Two days after activation, cell samples show between 96-99% viability. Five days after activation, cell samples show between 93-97% viability (Fig. 3.7a). There is only 2-3% variation in the viability between the control sample which contains switches but has not been exposed to light, the control sample which does not contain switches but has been exposed to light, and the illuminated switch-containing sample. A representative DIC image and fluorescent image (live cells stained with Calcein AM, dead cells stained with Ethidium homodimer) of the illuminated switch-containing sample is shown in Fig. 3.7b and 3.7c and confirms the efficacy of this method.

On-demand gene silencing has several key advantages over conventional methods to silence gene expression. Whereas various methods can interfere with gene expression within a population of cells, precise control of single cell's gene expression in the proximity of neighboring cells is not yet feasible. On-demand gene silencing can be performed within single cells, enabling future studies in cell-cell communication between single cells. Furthermore, on-demand gene silencing provides precise temporal regulation of a single cell's gene expression. Finally, unlike other nanoparticle-based gene interference methods, on-demand gene silencing can achieve nanometer-scale spatial resolution while maintaining high cell viability due to the low temperature mechanism of photothermal dehybridization.

As the flow cytometric results for conventional transfection (Fig. 3.5) and on-demand gene silencing (Fig. 3.6) indicate, the delivery of oligonucleotides into the cell with high efficiency remains challenging. It is however conceivable that this limitation can be overcome. For example, magnetically driven magnetic switches may be used to penetrate cell membranes with high efficiency (32). Once inside the cells, on-demand gene silencing can be activated with high efficiency.

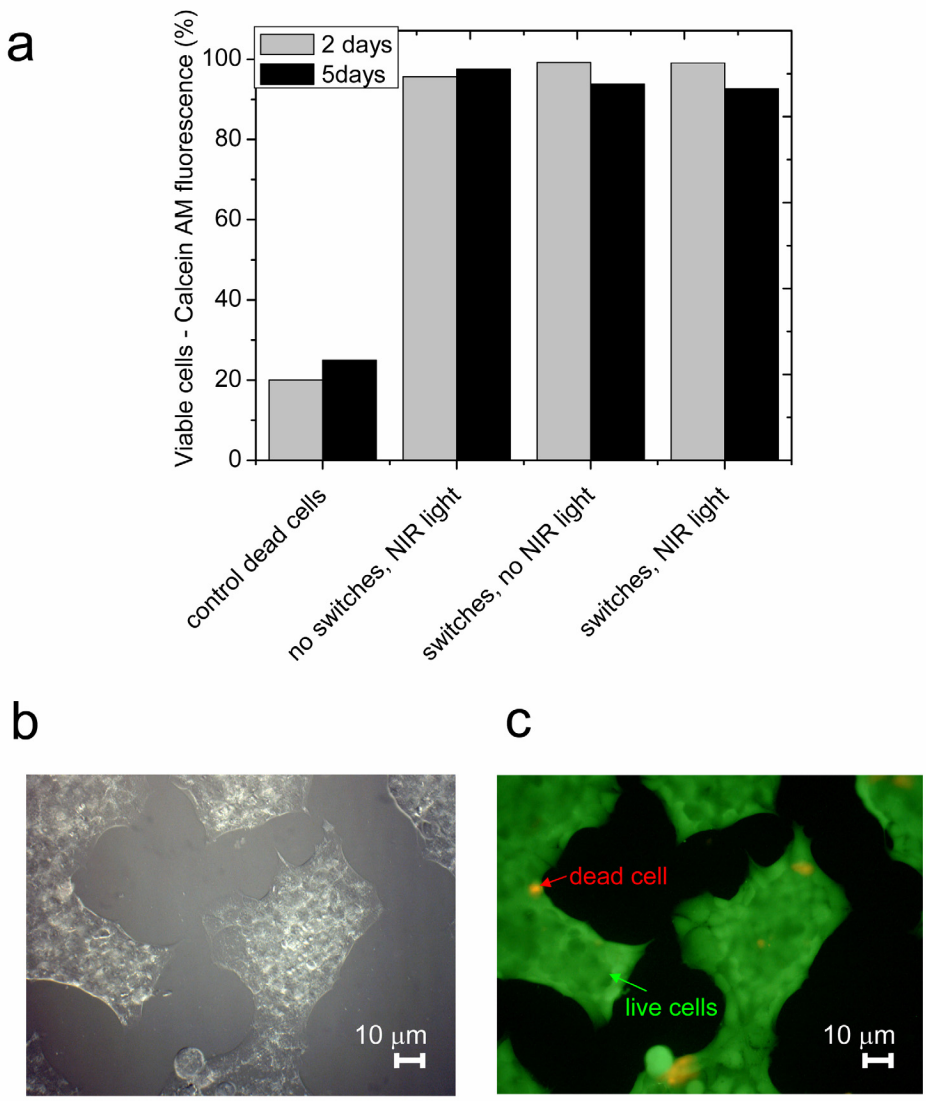

Figure 3.7. Viability after light illumination. (a) Calcein AM, a dye which converts from nonfluorescent cell-permeant calcein AM into fluorescent calcein by intracellular esterase enzymes in living cells, is used as a measure of cell viability. Flow cytometry is used to analyze the samples 2 days and 5 days after activation **(b)** Representative DIC image of BT474 cells after illumination. **(c)** Representative fluorescence image of live/dead cells after illumination. Live cells are stained with Calcein AM (green). Dead cells are stained with Ethidium homodimer (red).

In summary, nanoplasmonic optical antennae have been designed, which can silence with gene expression in a single cell for applications requiring nanometer-scale targeted release and precise temporal control of release. Using this method, it is possible to gain more control and flexibility in genetics, systems biology, and molecular cell biology-related studies. Gene silencing can be programmed at a desired phase of a cell cycle or a certain moment after external growth factor stimulation, making it possible to study dynamic changes in translational events and gene expression that would normally be hidden by ensemble averaging of the bulk population response.

References

1. Bahcall, O., Single Cell Resolution in Regulation of Gene Expression, *Molecular Systems Biology, 1*, E1 (2005).
2. Brent, R., A Partnership Between Biology and Engineering, *Nature Biotechnology, 22*, 1211 (2004).
3. Vance, V., Vaucheret, H., RNA Silencing in Plants - Defense and Counterdefense., *Science, 292*, 2277 (2001).
4. Rosenfeld, N., Young, J., Alon, U., Swain, P., Elowitz, M., Gene Regulation at the Single-cell Level, *Science, 307*, 1962 (2005).
5. Gardner, T., Cantor, C., Collins, J., Construction of a Genetic Toggle Switch in Escherichia Coli, *Nature, 403*, 339 (2000).
6. Nie, S., Xing, Y., Kim, G., Simons, J., Nanotechnology Applications in Cancer, *Annu. Rev. Biomed. Eng., 9*, 12.1 (2007).
7. Hamad-Schifferli, K., Schwartz, J., Santos, A., Zhang, S., Jacobsen, J., Remote Electronic Control of DNA Hybridization Through Inductive Coupling to an Attached Metal Nanocrystal Antenna, *Nature, 415*, 152 (2002).
8. Deiters, A., Light-activation as a Method of Regulating and Studying Gene Expression, *Current Opinion in Chemical Biology, 13*, 678 (2009).
9. Young, D. D., Lusic, H., Lively, M.O., Yoder, J.A., Deiters, A., Gene Silencing in Mammalian Cells with Light-Activated Antisense Agents, *ChemBioChem, 9*, 2937 (2008).
10. Mikat, V., Heckel, A., Light-dependent RNA interference with nucleobase-caged siRNAs, *RNA, 13*, 2341 (2007).
11. Liu, D., Karanicolas, J., Yu, C., Zhang, Z., Woolley, G., Site-specific Incorporation of Photoisomerizable Azobenzene Groups into Ribonuclease S, *Bioorg. Med. Chem. Lett., 7*, 2677 (1997).
12. Asanuma, H., Yoshida, T., Ito, T., Komiyama, M., Photo-responsive Oligonucleotides Carrying Azobenzene at the 2'-position of Uridine, *Tetrahedr. Lett., 40*, 7995 (1999).
13. Rosi, N. L., Giljohann, D.A., Thaxton, C.S., Lytton-Jean, A.K.R., Han, M.S., Mirkin, C.A., Oligonucleotide-Modified Gold Nanoparticles for Intracellular Gene Regulation, *Science, 312*, 1027 (2006).
14. Howard, K., Dong, M., Oupicky, D., Bisht, H., Buss, C., Besenbacher, F., Kjems, J., Nanocarrier Stimuli-Activated Gene Delivery, *Small, 1*, 54 (2006).
15. Chen, C., Lin, Y., Wang, C., Tzeng, H., Wu, C., Chen, Y., Chen, C., Chen, L., Wu, Y., DNA-Gold Nanorod Conjugates for Remote Control of Localized Gene Expression by near Infrared Irradiation, *Journal of the Americal Chemical Society, 128*, 3709 (2006).
16. Horiguchi, Y., Niidome, T., Yamada, S., Nakashima, N., Niidome, Y., Expression of Plasmid DNA Released from DNA Conjugates of Gold Nanorods, *Chemistry Letters, 36*, 952–953 (2007).
17. Hirsch, L., Stafford, R., Bankson, J., Sershen, S., Price, R., Hazle, J., Halas, N., West, J., Targeted Photothermal Tumor Therapy Using Metal Nanoshells, *Proceedings Second Joint EMBS BMES Conference, 1*, 530 (2002).

18. Norman, R. S., Stone, J. W., Gole, A., Murphy, C. J., Sabo-Attwood, T. L., Targeted Photothermal Lysis of the Pathogenic Bacteria, Pseudomonas aeruginosa, with Gold Nanorods, *Nanoletters, 8*, 302 (2008).
19. Pissuwan, D., Valenzuela, S. M., Killingsworth, M. C., Xu, X., Cortie, M., Targeted Destruction of Murine Macrophage Cells with Bioconjugated Gold Nanorods, *Journal of Nanoparticle Research, 9*, 1109–1124 (2007).
20. Dean, N. M., Bennett, C.F., Antisense Oligonucleotide-based Therapeutics for Cancer, *Nature Oncogene, 22*, 9087 (2003).
21. Marcusson, E. G., Bhat, B., Manoharan, M., Bennett, C.F., Dean, N.M., Phosphorothioate Oligodeoxyribonucleotides Dissociate from Cationic Lipids Before Entering the Nucleus, *Nucleic Acids Research, 26*, 2016 (1998).
22. Nikoobakht, B., El-Sayed, M. A., Preparation and Growth Mechanism of Gold Nanorods (NRs) Using Seed-Mediated Growth Method, *Chem. Mater., 15*, 1957 (2003).
23. Gou, L., Murphy, C. J., Fine-Tuning the Shape of Gold Nanorods, *Chem. Mater., 17*, 3668 (2005).
24. Bonetta, L., The Inside Scoop - Evaluating Gene Delivery Methods, *Nature Methods, 2*, 875 (2005).
25. Iczkowski, K. A., Omara-Opyene, A.L., and Roland Klösel, Metafectene is Superior to Lipofectamine in the Transfection of Gsaplha Prostate Cancer Cells, *Molecular Biotechnology, 28*, 97 (2004).
26. Troutman, T. S., Leung, S.J., Romanowski, M., Light-induced Content Release from Plasmon-resonant Liposomes, *Advanced Materials, 21*, 2334 (2009).
27. Wu, G., Mikhailovsky, A., Khant, H.A., Fu, C., Chiu, W., Zasadzinski, J.A., Remotely Triggered Liposome Release by Near-Infrared Light Absorption via Hollow Gold Nanoshells, *Journal of the American Chemical Society, 130*, 8175–8177 (2008).
28. Skirtach, A. G., Javier, A. M., Kreft, O., Kohler, K., Alberola, A. P., Mohwald, H., Parak, W. J., Sukhorukov, G. B., Laser-Induced Release of Encapsulated Materials inside Living Cells, *Angew. Chem. Int. Ed., 45*, 4612 –4617 (2006).
29. Lukacs, G. L., Haggie, P., Seksek, O., Lechardeur, D., Freedman, N., Verkman, A.S., Size-dependent DNA Mobility in Cytoplasm and Nucleus, *J. Biol. Chem., 275*, 1625 (2000).
30. Guarneri, V., C Bengala, C., Orlandini, C., Gennari, A., Donati, S., Campani, D., Collecchi, P., Maur, M.. Conte, P.F., HER2 Overexpression as a Prognostic Factor in Metastatic Breast Cancer Patients Treated with High Dose Chemotherapy and Autologous Stem Cell Support, *Bone Marrow Transplantation, 34*, 413 (2004).
31. Brandt, B., Griwatz, C., Heidl, S., Assmann, G., Zanker, K.S., Detection of the Metastatic Potential of Blood-borne and Immunomagnetically Enriched Epithelial Cells by Quantitative ERBB2 RT-PCR, *Clin. Exp. Metastasis, 14*, 399 (1996).
32. Cai, D., Mataraza, J., Qin, Z., Huang, Z., Huang, J., Chiles, T., Carnahan, D., Kempa, K., Ren, Z., Highly Efficient Molecular Delivery into Mammalian Cells Using Carbon Nanotube Spearing, *Nature Methods, 2*, 449 (2005).

CHAPTER 4:
BIOLOGICALLY FUNCTIONAL CATIONIC PHOSPHOLIPID-GOLD NANOPLASMONIC CARRIERS OF RNA

Rod-shaped nanoplasmonic optical antennae (ie. gold nanorods) in the NIR spectral region, due to their size, core material, and asymmetric geometry, display unique optical properties that make them attractive candidates for drug delivery (1-4), gene delivery (5-9), biomedical and molecular imaging (10-13), and therapeutics (14-22). These unique optical properties have been the main focus of the previous chapters. Despite these unique optical properties, the combination of three key factors – carrier functionality, colloidal stability, and cytotoxicity - have hindered the widespread use of gold rod-shaped nanoplasmonic optical antennae as carriers in biological and biomedical applications. Therefore, in order to harness the full potential of nanomaterials in these applications, this chapter focuses on the importance of the surface coating material surrounding the gold core.

With respect to cytotoxicity, while the gold core is widely accepted as being biocompatible (18), bare gold nanoparticles are known to interact with proteins and induce mis-folding at physiological conditions (23). Specifically, in the case of gold nanorods, the asymmetric geometry is obtained by synthesizing the nanorods in the presence of a high concentration (> 0.1 M) of cetyltrimethylammonium bromide (CTAB), a cationic micellar surfactant that associates preferentially with the {110} crystallographic facet of gold (24). However CTAB is known to degrade biomembranes and peptides (25), raising significant concern about the cytotoxicity of CTAB-coated nanorods *in vitro* and *in vivo* (25-30). The cytotoxic effects of CTAB-coated nanorods can be minimized by reducing the CTAB concentration below the critical micellar concentration (31), but at the expense of the nanorod suspension stability (Fig. 4.1b), consequently compromising their unique optical properties in biological environments. Notably, under physiological conditions, aggregation of nanoparticles has been shown to significantly red-shift and decrease the amplitude of the plasmon resonance band due to closely interacting nanoparticles (23, 32).

Finally, in order for plasmon-resonant nanorods to function as biological carriers, biomolecules such as DNA oligonucleotides, RNA oligonucleotides, or short interfering RNA (siRNA) must be able to adsorb on their surface. Notably, in the case of siRNA, chemical modifications may affect the functionality and efficacy of siRNA (33, 34). Therefore, the attachment of siRNA onto the surface of gold nanorods without additional chemical modifications to the siRNA themselves is highly desirable. Poly(ethylene glycol) (PEG) has previously been used to modify gold nanorods for *in vivo* applications (35-37); however, their ability to maximally carry subsequent biomolecules is limited due

to the absence of surface charge. Organothiols and polystyrenesulfonate have been used to coat gold nanorods; however, attachment of nucleic acids has not been demonstrated (38, 39). Synthetic lipids have also been used to modify gold nanorods (29, 30, 40); however carrier capabilities and/or biocompatibility have not yet been addressed. Polyelectrolyte coating schemes have also been to coat gold nanorods (21, 41); however, plasmonic properties under physiological conditions have not yet been discussed. Alternatively, since cationic lipid formulations have already been optimized for both *in vitro* and *in vivo* gene transfer over the past decade (42, 43) and many cationic lipid-based gene delivery approaches are currently being tested at the clinical level (44, 45), validated cationic lipids make ideal candidates for modifying ordinary nanorods into biologically compatible nanorods that simultaneously satisfy carrier functionality, colloidal stability, and non-cytotoxicity. The positively charged surface can be used to adsorb negatively-charged biomolecules such as RNA oligonucleotides, siRNA, or DNA oligonucleotides (Fig. 4.1a). In addition to carrying siRNA, RNA oligonucleotides, and DNA oligonucleotides, these carriers can also be used to carry a variety of other compounds such as proteins and drugs by incorporation into or binding to the cationic phospholipid membrane (Fig. 4.1a).

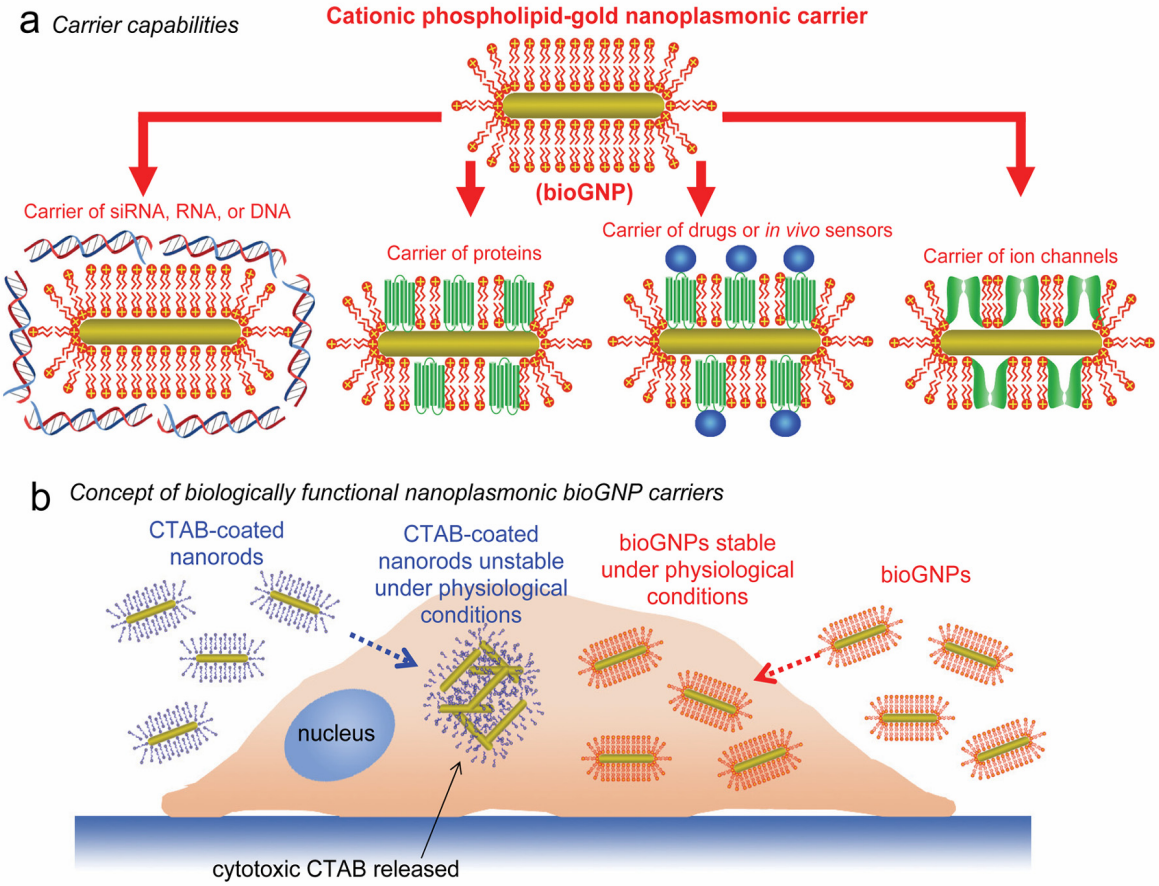

Figure 4.1. Concept of biologically functional cationic phospholipid-gold nanoplasmonic carriers (bioGNPs). (a) Cationic phospholipid bilayer formed around bioGNPs, which can carry RNA, DNA, siRNA, proteins, and drugs. **(b)** When CTAB is reduced below the critical micellar concentration, CTAB-coated gold nanorods aggregate. Dissociated CTAB raises cytotoxicity concerns since CTAB can degrade biomembranes. Nontoxic bioGNPs are stable and able to retain their unique optical properties.

In this chapter, we present biologically functional cationic phospholipid-gold plasmonic carriers (bioGNPs) that exhibit carrier capabilities, demonstrate improved colloidal stability, and show no cytotoxicity under physiological conditions. Using an adaptation of vesicle-to-nanoparticle fusion (40), we exchanged the cytotoxic CTAB surfactant at the nanorod surface with commercially available cationic phospholipids successfully used for *in vivo* studies (46, 47). We first demonstrate that bioGNPs are stable under physiological conditions thus retaining their unique plasmonic properties. We then show that the positively charged surface of nanorods can adsorb cargo such as DNA oligonucleotides, RNA oligonucleotides, or siRNA. We finally demonstrate the biocompatibility of bioGNPs via viability/cytotoxicity and cell proliferation studies.

Methods

Cell preparation. The human breast carcinoma line MCF-7 was purchased from the American Type Culture Collection (ATCC). Dulbecco's modified eagle's media (DMEM) was purchased from Invitrogen and was supplemented with 10% heat-inactivated fetal bovine serum, 0.1% nonessential amino acids, and 1% sodium pyruvate. Cells were cultured in the supplemented media and maintained in a 37˚C incubator with 5% CO_2 humidified air.

Synthesis of DNase/RNase-free gold nanorods*.* Gold nanorods of aspect ratio 3.0 were synthesized by adapting a previously reported seed-mediated growth method (24, 48) to a DNase/RNase-free environment. Hexadecyltrimethylammonium bromide (CTAB), silver nitrate ($AgNO_3$), L-ascorbic acid, sodium tetrahydroborate ($NaBH_4$), and hydrogentetrachloroaurate ($HAuCl_4$) were purchased from Alfa Aeser. All solutions were prepared using 0.2 μm filtered nuclease-free water. All glassware and metalware were baked at 240°C for 24 hours to remove exogenous RNase. All pipetting devices and counter space was treated with 70% ethanol. All disposable plastic pipette tips and centrifuge tubes were certified to be free of RNase.

To prepare the seed solution, 5 mL of 0.2 M CTAB solution was mixed with 5 mL of 0.0005 M $HAuCl_4$. Ice-cold 0.010 M $NaBH_4$ (0.60 mL) was then added and the solution was continuously stirred for 2 minutes at room temperature. To prepare the growth solution, 9.5 mL of 0.1 M CTAB was mixed with 60 μL of 0.10 M $AgNO_3$, 0.5 mL of 0.01 M $HAuCl_4$, 55 μL of 0.10 M ascorbic acid, and 12 μL of seed solution with continuous stirring. The gold nanorods were aged overnight at room temperature. At this point, the CTAB concentration in the gold nanorod solution was approximately 0.1 M. The nanorod concentration (approximately 30 μg/mL or 7E11 particles/mL) was confirmed by adjusting to an absorbance of 1 at the longitudinal plasmon resonance wavelength using UV-VIS spectroscopy. Aspect ratio was determined by scanning electron microscopy (Hitachi S-4500 FESEM) at 150,000X magnification.

Synthesis of bioGNPs. Commercially available cationic phospholipids Oligofectamine, Lipofectamine 2000 and sc29528 were purchased from Invitrogen and Santa Cruz

Biotechnology. Non-ionic surfactant Brij56 was purchased from Fluka and prepared in nuclease-free water.

To remove excess CTAB surfactant, 500 μL unmodified CTAB-coated nanorods (UV-VIS absorbance of 1) in 0.1 mM CTAB were centrifuged at 5000 rpm for 10 minutes. A 10 μL pellet was transferred to a new microcentrifuge tube, redispersed in 500 μL of DEPC-treated water such that the final concentration was approximately 0.1 mM, briefly vortexed, and sonicated for 1 minute.

To replace CTAB with non-ionic Brij56 surfactant at the nanorod surface, nanorods were then centrifuged again at 5000 rpm for 10 minutes. A 10 μL pellet was transferred to a new microcentrifuge tube, resuspended in 500 μL of 0.01 mM Brij56, briefly vortexed, and sonicated for 1 minute.

To replace Brij56 surfactant with a phospholipid bilayer membrane at the nanorod surface, the aforementioned procedure was repeated again to resuspend particles in 50 μL of either Oligofectamine, sc29528, or Lipofectamine 2000. Finally, to remove excess cationic phospholipids in the solution, bioGNPs were washed twice with nuclease-free water by centrifugation at 5000 rpm for 10 minutes.

Preparation of bioGNP carriers. Phosphorothioate 21-mer RNA oligonucleotides conjugated to fluorescein (FAM) dye (488 nm excitation, 532 nm emission) were purchased from Integrated DNA Technologies. The sequence was: 5' GUAGAUUACCACUGGAGUCUU - FAM -3'. Rnase-free 20X Tris-EDTA (TE) buffer was purchased from Invitrogen and was used to prepare 1X TE buffer solution using nuclease-free water.

Stock solutions of RNA oligonucleotides were prepared in RNase-free 1X TE buffer. To 500 μL of bioGNPs, 0.25 μL of 100 μM RNA oligonucleotides was added. The solution was vortexed and allowed to incubate for 1 hour. To remove excess oligonucleotides from solution, bioGNPs were washed twice with nuclease-free water by centrifugation at 5000 rpm for 10 minutes. After preparation of RNA-bioGNP conjugates, an absorbance of 0.2 was measured by UV-VIS. By comparing with the original nanorod's UV-VIS absorbance of 1, the concentration of bioGNPs was estimated to be approximately 1/5 the original nanorod concentration (approximately 6 μg/mL or 1.4E11 particles/mL). Since fluorescence quenching by bioGNPs was not observed, bioGNP carriers of fluorescently-labeled RNA oligonucleotides were finally visualized using fluorescent microscopy

Dynamic light scattering of bioGNP carriers. DLS data were collected for all samples using a DynaPro-99-E-15 DLS apparatus from Wyatt Technologies. For each sample, at least 20 scans were performed, each with a 10 s acquisition time, using a scattering angle of 90º. Optimem medium was purchased from Invitrogen.

CTAB-coated nanorods, Brij56-coated nanorods, are bioGNPs were prepared as described above. DLS measurements were taken of each sample (diluted 1:60 in a quartz cuvette) as-prepared, after washing twice in nuclease-free water, and after resuspending in Optimem medium.

Internalization assay of bioGNP carriers. BioGNP carriers of FAM-labeled RNA oligonucleotides (500 μL) were concentrated into a 5 μL pellet by centrifugation at 5000 rpm for 10 minutes. MCF-7 cells were harvested and resuspended in DMEM media to a concentration of 240,000 cells/mL. To each well of a 6-well plate, 0.5 mL of cell suspension and 5 μL of concentrated FAM-RNA functionalized bioGNPs were added (120,000 cells/well). The cells were allowed to incubate for 10 hours. After 10 hours, cells were carefully washed with 1X phosphate buffered solution (PBS), detached using 0.25% trypsin for 2 minutes, mixed with media 4:1 to deactivate trypsin, collected using centrifugation (1800 rpm, 4 minutes), and resuspended in 2% paraformaldehyde. Trypan blue was finally added to the cell suspension at 50% concentration to quench uninternalized bioGNP carriers.

As a control, surface receptor ERBB2 on ERBB2-positive BT474 cells was labeled with antibodies conjugated to FITC dye (340553, BD Biosciences). Cells were harvested using 1 mM EDTA for 10 minutes. Cells were resuspended in surface-staining buffer containing 0.5% bovine serum albumin (BSA) and 0.1% sodium azide in 1X PBS. 5 μL of normal mouse IgG_1 (I8765, Sigma Aldrich) was added and cells were incubated for 15 minutes to prevent non-specific binding of antibodies to Fc receptors. 15 μL of anti-ERBB2-FITC was added and cells were incubated for 45 minutes at room temperature. Cells were then washed in surface-staining buffer. Cells were resuspended in 1X PBS containing 2% paraformaldehyde. Trypan blue was finally added to the cell suspension at 50% concentration to quench surface receptors labeled with fluorescent antibodies . LSRII flow cytometer (BD Biosciences) and FlowJo software (Tree Star, Ashland, Oregon) was used to analyze samples.

Visualization of internalized bioGNP carriers by darkfield light microscopy. 500 μL of bioGNPs were concentrated into a 5 μL pellet by centrifugation at 5000 rpm for 10 minutes. Sterile and RNase-free glass coverslips were placed into each well of a 6-well plate. MCF-7 cells were harvested and resuspended in cell culture media to a concentration of 240,000 cells/mL. To each well, 0.5 mL of cell suspension and 5 μL of concentrated bioGNPs were added on top of the coverslips (120,000 cells/well). The cells were allowed to incubate for 10 hours. After 10 hours, 2% paraformaldehyde was added to each well to fix cells onto the glass coverslips. For visualization purposes, cell nuclei were stained with DAPI, purchased from Invitrogen, by incubating cells in 300 nM DAPI to each well for 5 minutes. 1X PBS was then added to each well to wash the cells. A coverslip containing fix, adhered cells was then placed facedown on a microscope slide and broadband white light was shined onto the adhered cells from an oblique angle using a darkfield condenser lens. The scattered light alone was collected using a microscope objective lens with a numerical aperture (NA) of 0.65 that was smaller than the NA (1.2-1.4) of the illumination condenser lens.

Viability/cytotoxicity and proliferation analysis. As a standard, liposomes of known concentration and of similar size to the commercial phospholipid liposomes were prepared as previously described[46]. Using these liposomes as standards to compare light intensity measurements, the concentration of the commercial phospholipids was estimated to 6 mM. As a control, unmodified CTAB-coated nanorods were initially resuspended in 6 mM CTAB. Then, 500 μL (50 μg/mL) of bioGNPs or unmodified CTAB-coated nanorods were washed once with nuclease-free water to remove excess lipids/CTAB and were then concentrated into a 5 μL pellets by centrifugation at 5000 rpm for 10 minutes.

MCF-7 cells were harvested and resuspended in cell culture media to a concentration of 240,000 cells/mL. To each well of a 6-well plate, 0.5 mL of cell suspension and 5 μL of concentrated bioGNPs or unmodified CTAB-coated nanorods were added (120,000 cells/well). The cells were allowed to incubate for 24 hours. After 24 hours, wells containing cells which were to be analyzed 72 hours and 120 hours later are exchanged with fresh media. Cells which were to be analyzed after 24 hours were washed with 1X PBS, detached using 0.25% trypsin for 2 minutes, mixed with media 4:1 to deactivate trypsin, collected using centrifugation (1800 rpm, 4 minutes), and resuspended in 0.5 mL of 0.125 μM Calcein AM from Invitrogen. Immediately prior to flow cytometric analysis, 5 μL of PI from BD Pharmingen was added to stain dead cells for cytotoxicity analysis. Cells are simultaneously analyzed for viability and cytotoxicity using the LSRII flow cytometer within 30 minutes. This same viability/cytotoxicity staining procedure was repeated after 72 hours and 120 hours of incubation. Cell proliferation was assessed by cell count analysis using a hemocytometer after 120 hours of incubation.

Results and Discussion

Gold nanorod carriers were synthesized by modifying a seed-mediated growth approach (24, 48) to be free of DNase/RNase contamination. Using dynamic light scattering (DLS), in Fig. 4.2a and in Table 4.1, the resultant CTAB-coated nanorod carriers show a size distribution with an average radius of ~15 nm (30 nm diameter). Since the nanorod's length was short and the rotational diffusion was therefore rapid, the nanorod was approximated as a translationally diffusing sphere whose diameter equaled the length of the nanorod (30 nm). Lengths based on DLS measurements were in agreement with lengths seen in SEM images (Fig. 4.5a). Since the resultant gold nanorod carriers were coated with CTAB that yielded a net positive surface charge from the quaternary ammonium surfactant head group (24), negatively-charged, fluorescently-conjugated 21-mer RNA oligonucleotides readily attached to the CTAB-coated nanorod carriers, enabling visualization by fluorescent microscopy (Fig. 4.2b).

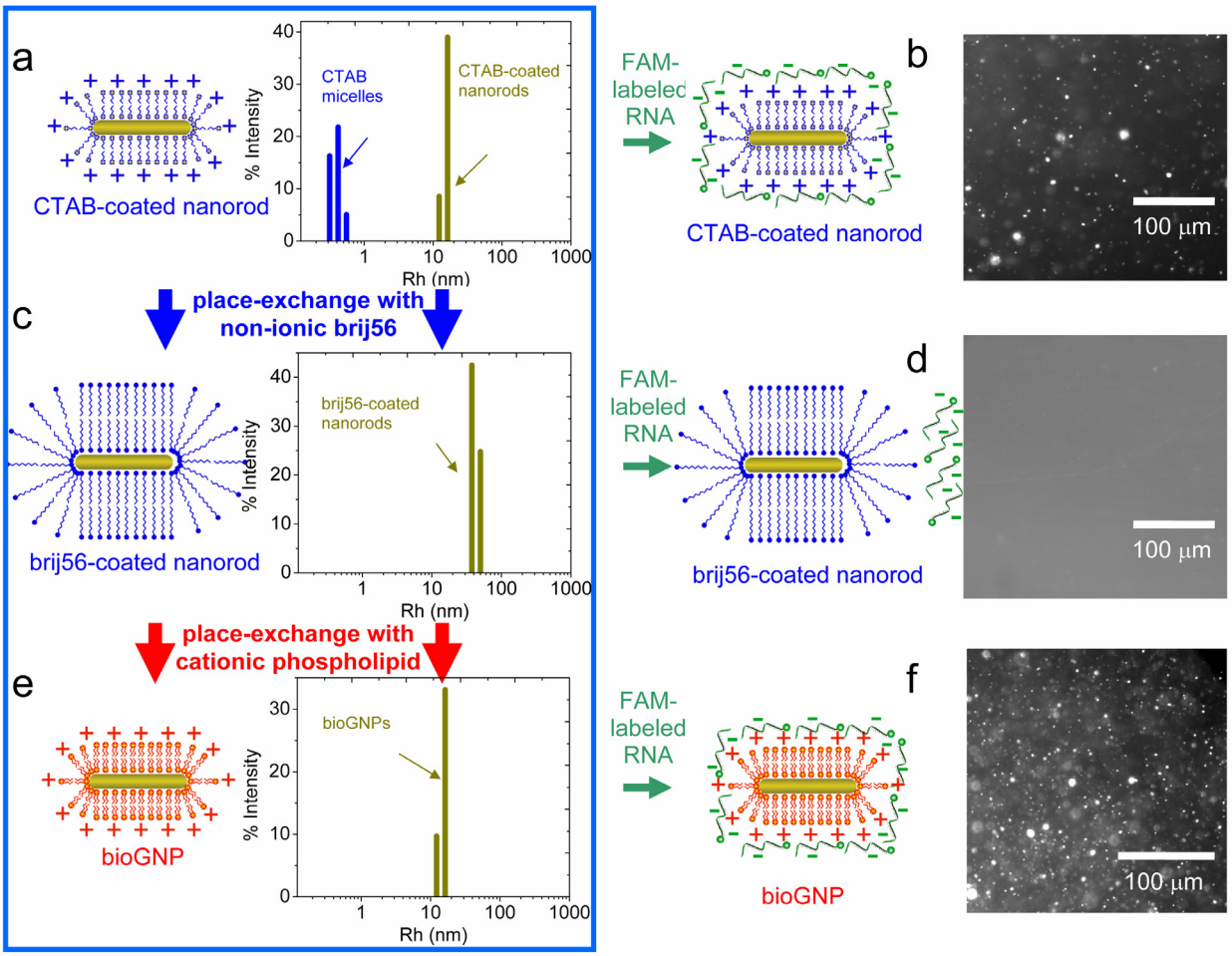

Figure. 4.2. Synthesis of bioGNP carriers. (a) CTAB-coated nanorods prepared by seed-mediated growth process. Dynamic light scattering (DLS): CTAB-coated nanorod carriers show size distribution with an average radius of ~15 nm (30 nm diameter). **(b)** Fluorescent image showing CTAB-coated nanorods carry negatively-charged, fluorescent FAM-conjugated RNA. **(c)** The CTAB surfactant then place-exchanged with a non-ionic surfactant Brij56 surfactant. Using DLS, brij56-coated nanorods show a size distribution with an average radius ~50 nm (100 nm length). **(d)** Fluorescent image showing that brij56-coated nanorods are resistant to coupling with fluorescently-conjugated RNA oligonucleotides. **(e)** The brij56 coating then place-exchanged with cationic phospholipids to form bioGNPs. Using DLS, bioGNPs show an average radius of ~15 nm (30 nm length) with a narrow size distribution. **(f)** Fluorescent image showing bioGNPs carry negatively-charged, fluorescent FAM-conjugated RNA oligonucleotides.

sample	R_h (nm)	L (nm)
CTAB-coated nanorod	14.7 ± 1.9	29.5 ± 3.8
Oligofectamine-coated bioGNP	14.2 ± 2.0	28.4 ± 4.0
Lipofectamine-coated bioGNP	14.6 ± 2.4	29.2 ± 4.9
sc29528-coated bioGNP	15.3 ± 1.7	30.6 ± 3.3

Table 4.1. Hydrodynamic radius R_h and rod lengths L. Based on DLS measurements, hydrodynamic radius Rh and rod lengths L for CTAB-coated nanorods, Oligofectamine-coated bioGNPs, Lipofectamine-coated bioGNPs, and sc29528-coated bioGNPs are summarized in table format.

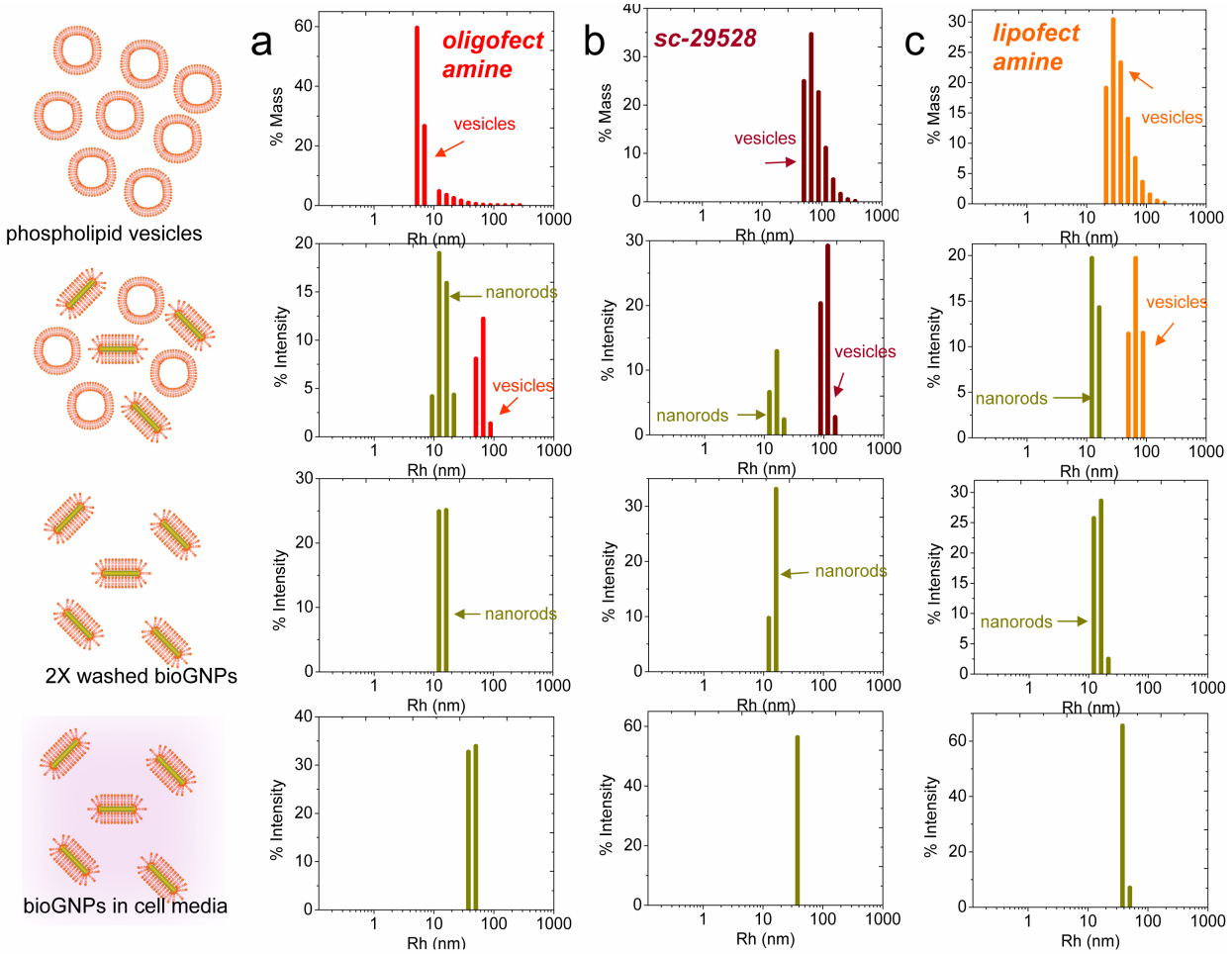

Figure 4.3. Experimental characterization of stability of Oligofectamine-coated bioGNPs, sc29528-coated bioGNPs, and Lipofectamine2000-coated bioGNPs. (a) DLS size distribution of cationic phospholipid vesicles (Oligofectamine), DLS size distribution of Oligofectamine-coated bioGNPs, DLS size distribution of Oligofectamine-coated bioGNPs that have been washed 2X and resuspended in water, and DLS size distribution of Oligofectamine-coated bioGNPs that have been resuspended cell culture media. **(b)** DLS size distribution of cationic phospholipid vesicles (sc29528), DLS size distribution of sc29528-coated bioGNPs, DLS size distribution of sc29528-coated bioGNPs that have been washed 2X and resuspended in water, and DLS size distribution of sc29528-coated bioGNPs that have been resuspended cell culture media. **(c)** DLS size distribution of cationic phospholipid vesicles (Lipofectamine2000), DLS size distribution of Lipofectamine2000-coated bioGNPs, DLS size distribution of Lipofectamine2000-coated bioGNPs that have been washed 2X and resuspended in water, and DLS size distribution of Lipofectamine2000-coated bioGNPs that have been resuspended cell culture media.

The first stage in demonstrating stable bioGNPs was place-exchanging CTAB with cationic phospholipids vesicles at the nanorod surface by using a vesicle-to-nanorod fusion approach. Excess CTAB surfactant was first removed from the CTAB-coated nanorod solution to yield a final CTAB concentration was approximately 0.1 mM. These CTAB-coated nanorods were then dispersed in various commercially available liposome formulations in approximately <50 fold excess. The phospholipid bilayer coating at the nanorods' surface readily replaced the CTAB surfactant. The formation of

phospholipid bilayer coatings on gold nanorods and simultaneous loss of surfactant coatings been previously determined by NMR and FTIR spectroscopy and zeta potential measurements (40).

An alternative route to phospholipid-coated nanorods was to first place-exchanged the CTAB surfactant with the non-ionic surfactant Brij56, followed by place-exchange with cationic phospholipid vesicles. Since CTAB removal from the nanorods is essential to minimize cytotoxicity and to eliminate any electrostatic contribution, the latter procedure was developed since it is known that CTAB is capable of inserting itself into lipid bilayers (49). Therefore, all the results henceforth describe the Brij56-to-phospholipid exchange process for coating gold nanorods with a phospholipid bilayer. In Fig. 4.2c, Brij56-coated nanorods show a size distribution with an average radius ~50 nm (100 nm length). The narrow width of the size distribution suggests that Brij56-coated nanorods were stable and with no observed aggregation over a period of weeks. As seen in the fluorescent image of Fig. 4.2d, the Brij56-coated nanorods were resistant to coupling with fluorescently-conjugated RNA oligonucleotides. The Brij56 coating was then place-exchanged with various commercially-available cationic phospholipids to form bioGNPs by simply exposing surfactant-coated gold nanorods with cationic phospholipid vesicles. BioGNPs show an average radius of ~15 nm (30 nm length) with a narrow size distribution (Fig. 4.2e, Fig. 4.3, and Table 4.1). The smaller average lengths suggest that the phospholipid bilayer did not layer on top of the Brij56 coating, but instead successfully place-exchanged with the Brij56 at the bioGNPs' surface. Furthermore, negatively-charged, fluorescently-conjugated RNA oligonucleotides readily attach to the bioGNP carriers, strongly suggesting that the non-ionic surfactant was successfully place-exchanged by a positively-charged phopholipid bilayer (Fig. 4.2f).

Having established that the CTAB coating can be place-exchanged with a cationic phospholipid membrane, the stability of bioGNPs was then studied and compared against the stability of the CTAB-coated nanorods under biological conditions. CTAB-coated nanorods, which were washed twice and resuspended in nuclease-free water, showed an average radius of ~15 nm (30 nm length) with a broad distribution in Figure 4.4c. The twice-washed CTAB-coated nanorods showed a slightly wider size distribution compared to as-prepared CTAB-coated nanorods in 0.1 M CTAB solution (Fig. 4.4b), suggesting the onset of aggregation. After resuspending the twice-washed CTAB-coated particles in cell culture media, further broadening was seen of the size distribution centered at radius of 60 nm, suggesting that particles were highly unstable in culture media (Fig. 4.4d). In comparison, bioGNPs which were washed twice and resuspended in nuclease-free water were highly stable (Fig. 4.4g). When resuspended in cell culture media, bioGNPs continue to exhibit a narrow size distribution (Fig. 4.4h and Fig. 4.3), thus affirming their excellent stability under biological conditions. Furthermore, optical properties were confirmed using UV-VIS spectroscopy. BioGNPs were suspended in water and were compared to bioGNPs suspended in cell culture media by UV-VIS spectroscopy in Figure 4.5a. BioGNPs suspended in cell culture media continue to display a large absorption cross-section and a narrow spectral width of the longitudinal plasmon resonance band, thus confirming bioGNPs' excellent stability under biological conditions.

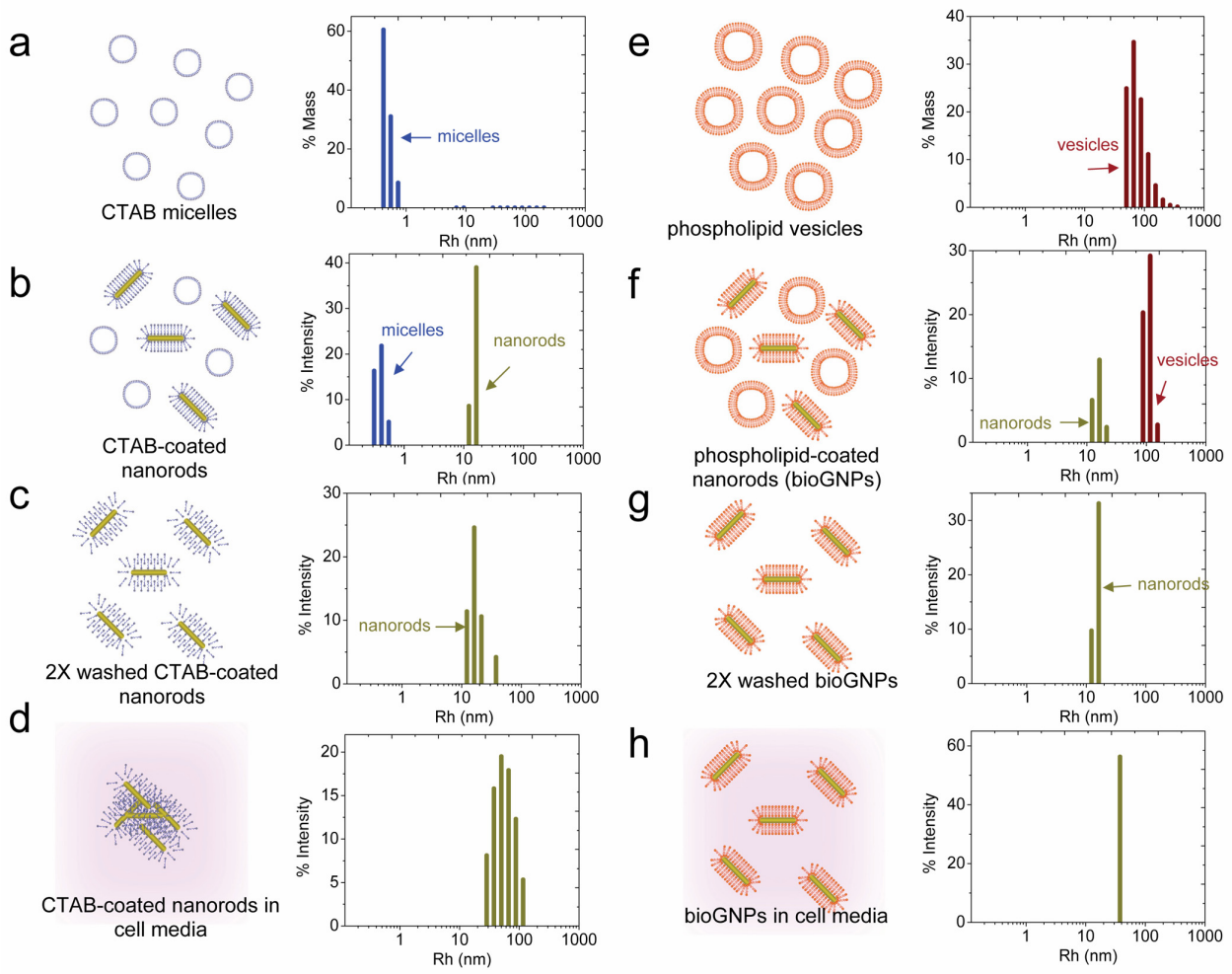

Figure 4.4. Experimental characterization of bioGNP stability. (a) DLS size distribution of CTAB micelles, (b) DLS size distribution of CTAB-coated nanorods, **(c)** DLS size distribution of CTAB-coated nanorods that have been washed 2X and resuspended in water, **(d)** DLS size distribution of CTAB-coated nanorods that have been resuspended cell culture media, **(e)** DLS size distribution of cationic phospholipid vesicles (sc-29528), (f) DLS size distribution of bioGNPs, **(g)** DLS size distribution of bioGNPs that have been washed 2X and resuspended in water, **(h)** DLS size distribution of bioGNPs that have been resuspended cell culture media.

Having confirmed bioGNPs' stability, we then investigated the internalization of bioGNPs into human cells. Net-positively charged bioGNPs were endocytosed by MCF-7 human breast carcinoma cells by incubation for 10 hours. To visualize internalized bioGNPs, the cells were then illuminated with unpolarized white light from an oblique angle using a darkfield condenser lens, and scattered light was collected using a transmission-mode darkfield microscope (Fig. 4.5b). To locate cells' nuclei, darkfield scattering images were overlaid with DAPI-stained images. It is clearly evident from Fig. 4.5b that scattered light from cells containing bioGNPs are easily differentiated from cells lacking bioGNPs.

To further confirm that bioGNPs were in fact internalized within cells and not externally adsorbed onto the cells' surface, MCF-7 cells were first exposed for 10 hours to bioGNP carriers of fluorescently-labeled RNA oligonucleotides. Uninternalized carriers were then rendered non-fluorescent by using trypan blue as a quencher. Since trypan blue absorbs light between 475 and 675 nm (50), the emission of fluorescent dyes within this wavelength range are quenched in the presence of trypan blue. If bioGNP carriers of FAM-labeled RNA oligonucleotides (excitation 495 nm, emission 520 nm) are indeed internalized within cells, it is expected that their fluorescence should remain unquenched when cells are resuspended in trypan blue. Flow cytometry results displayed in Fig. 4.5 confirm that the majority of the bioGNP carriers of FAM-labeled RNA oligonucleotides remained fluorescent within the protective confines of intact cell membranes. In contrast, as a control, surface receptor ERBB2 (also known as HER-2, neu, and EGFR-2) on ERBB2-positive BT474 breast carcinoma cells were labeled with antibodies conjugated to FITC dye (excitation 488 nm, emission 532 nm). To inhibit internalization by receptor-mediated endocytosis, FITC-conjugated antibodies were bound in the presence of sodium azide. Flow cytometry results in Figure 4.5d show that surface-bound FITC on control cells was efficiently quenched in the presence of trypan blue.

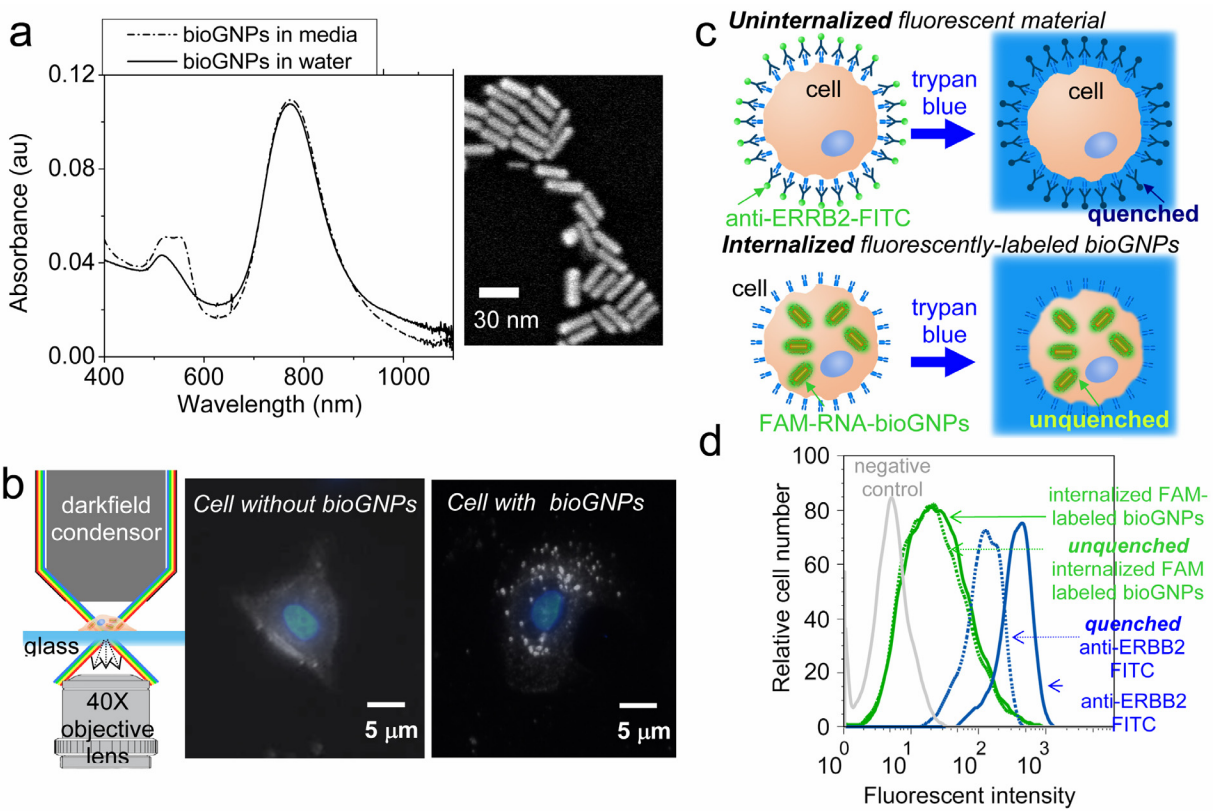

Figure 4.5. Experimental characterization and internalization of bioGNP carriers. (a) UV-VIS absorbance spectra of bioGNPs suspended in water (solid line), UV-VIS absorbance spectra of bioGNPs suspended in media (dash line), and scanning electron microscopy image of bioGNPs, **(b)** Schematic of microscope setup, darkfield scattering image of a cell without bioGNPs overlaid with DAPI-stained nuclei image, and darkfield scattering image of a cell containing single bioGNPs overlaid with DAPI-stained nuclei image. **(c)** concept of internalization assay where uninternalized fluorescent material (ie. FITC conjugated ERBB2 antibody) is quenched by trypan blue and internalized fluorescent material (ie. bioGNP carriers of FAM conjugated RNA oligonucleotides) remains unquenched by trypan blue. **(d)** flow cytometric comparison of MCF-7 cells containing unquenched bioGNP carriers of fluorescently-labeled RNA oligonucleotides and quenched surface-labeled antibodies (FITC conjugated) recognizing ERBB2 surface receptor on ERBB2-positive BT474 cells. Green solid line represents cells containing bioGNP carriers of fluorescently-labeled RNA oligonucleotides in the absence of trypan blue quencher. Green dotted line represents cells containing unquenched bioGNP carriers of fluorescently-labeled RNA oligonucleotides in the presence of trypan blue quencher. Blue solid line represents cells that are surface-labeled with fluorescent antibodies in the absence of trypan blue quencher. Blue dotted line represents cells that are quenched surface-labeled with fluorescent antibodies in the presence of trypan blue quencher. Grey solid line represents negative control cells.

Finally, the biocompatibility of bioGNPs was investigated and compared against unmodified CTAB-coated nanorods by conducting a long term viability/cytoxicity and proliferation studies in MCF-7 cells. Viability/cytotoxicity was conducted using a two-color fluorescence assay to simultaneously determine numbers of live and dead cells. Calcein AM - a dye which converts from nonfluorescent cell-permeant calcein AM into fluorescent cell-impermeant calcein by intracellular esterase enzymes in living cells - was used as a measure of cell viability. Propidium iodide (PI) - a dye that enters through permeabilized membranes of compromised cells - was used as a measure of cell

cytotoxicity. The concentration of commercial cationic phospholipids was estimated to be approximately 6 mM based on DLS comparison of standards of known concentration. Unmodified CTAB-coated nanorods were therefore initially resuspended in 6 mM CTAB to obtain comparable results. Unmodified CTAB-coated nanorods and bioGNPs were then washed with nuclease-free water to remove excess lipids/CTAB and resuspended in cell culture media. Based on DLS measurements, bioGNPs were highly stable while unmodified CTAB-coated nanorods were only moderately stable in cell culture media. In order to retain unique optical properties of stable nanoparticles, further washing was avoided since twice-washed CTAB-coated nanorods tend to strongly aggregate in cell culture media as seen in DLS measurements in Fig. 4.4d. After 72 hours and 120 hours of incubation, based on flow cytometric data, viability (Fig. 4.7a) and cytotoxicity (Fig. 4.7b) of cells containing bioGNPs were statistically significant from cells containing unmodified CTAB-coated nanorods (graphs constructed from flow cytometry data in Fig. 4.6). It is apparent that cells containing bioGNPs are viable whereas cells containing CTAB-coated nanorods are compromised. Clearly, bioGNP carriers are a superior alternative to unmodified CTAB-coated nanorods for biological studies.

Cell proliferation was also assessed by cell count analysis after 120 hours of incubation with and without bioGNPs. Based on cell count analysis, doubling times were then determined for bioGNP-containing samples and compared to an untreated control sample. Doubling time of 55 hours for the untreated control sample was in agreement with doubling times previously reported in literature for MCF-7 cells (51). Cells containing bioGNPs exhibited approximately similar doubling times as the untreated control sample (Fig. 4.7c), verifying that incubation with bioGNPs did not adversely affect proliferation of MCF-7 cells.

While *in vitro* experiments were successfully demonstrated here, developing bioGNP carriers for use *in vivo* mammalian and non-mammalian model systems is anticipated. BioGNP carriers can be coated with cationic phospholipid formulations specifically optimized for biodistribution *in vivo*. In addition to carrying siRNA, RNA oligonucleotides, and DNA oligonucleotides for gene delivery applications, bioGNPs can also be used to carry a variety of other compounds such as proteins and drugs for *in vivo* applications.

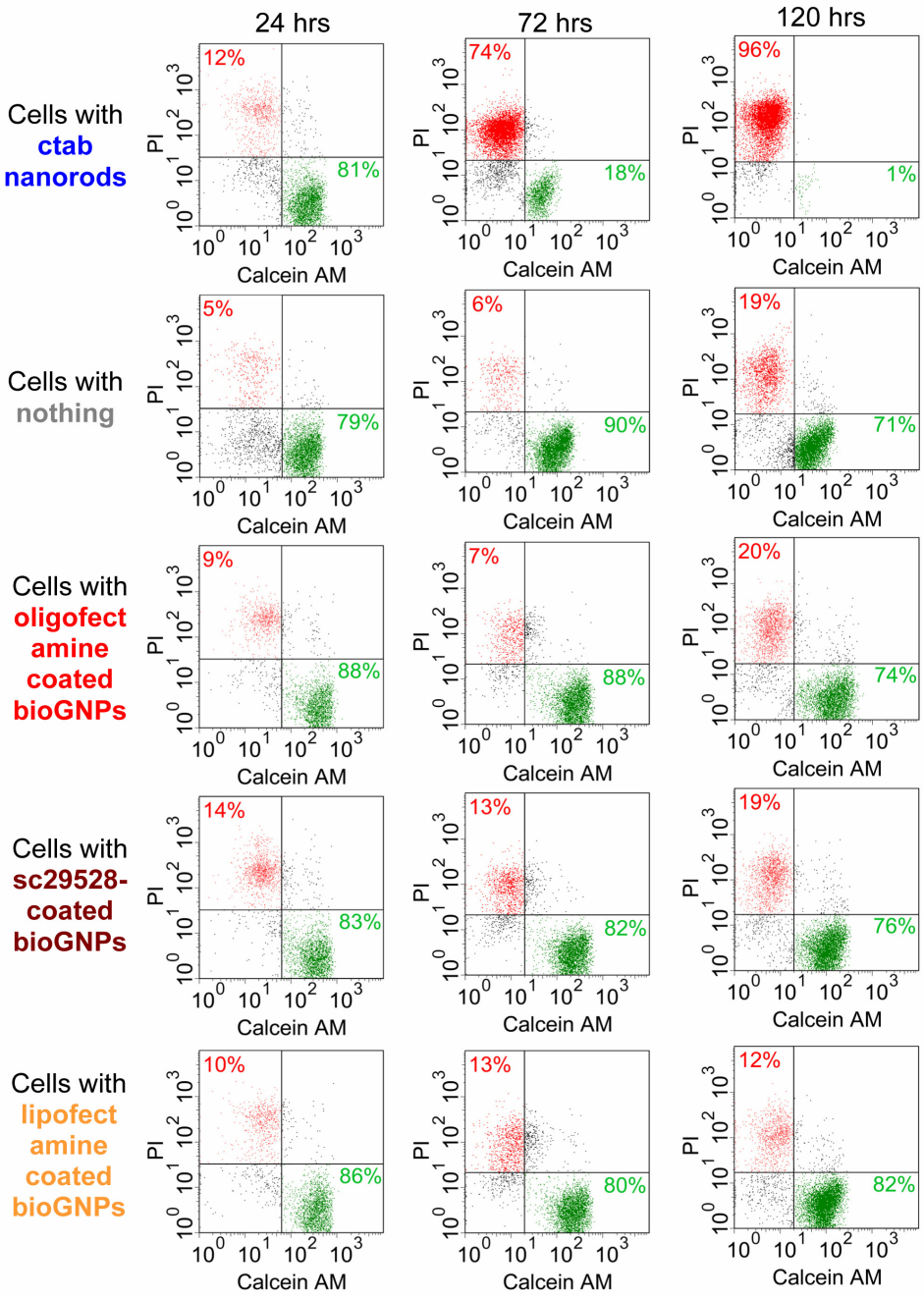

Figure 4.6. Viability/Cytotoxicity analysis. Flow cytometric results of viability and cytotoxicity using Calcein AM and Propidium Iodide after 24 hrs, 72hrs, and 120 hrs incubation with nothing, CTAB-coated nanorods, Oligofectamine-coated bioGNPs, sc29528-coated bioGNPs, and Lipofectamine2000-coated bioGNPs.

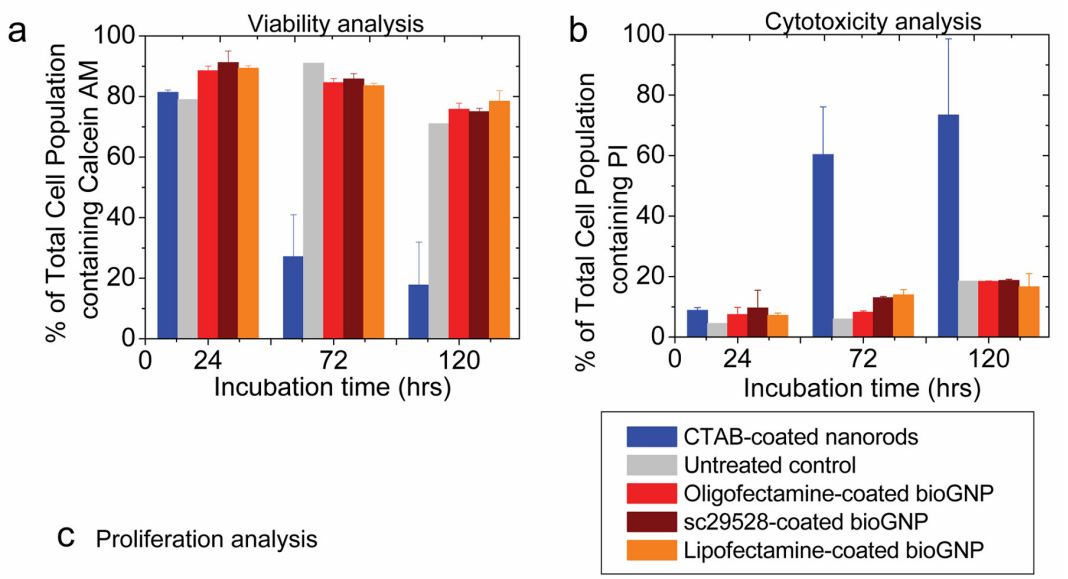

c Proliferation analysis

Sample	$N_{initial}$(cells)	N_{final} (cells)	Doubling time (hrs)
Untreated control cells	2E5	1.2E6	55
Cells with Oligofectamine-coated bioGNPs	2E5	1.2E6	55
Cells with sc29528-coated bioGNPs	2E5	0.9E6	66
Cells with Lipofectamine2000-coated bioGNPs	2E5	1.1E6	58

Figure 4.7. Biocompatibility analysis of bioGNPs. (a) Viability analysis - flow cytometric results of viability using Calcein AM after 24 hrs, 72hrs, and 120 hrs incubation with nothing, CTAB-coated nanorods, Oligofectamine-coated bioGNPs, sc29528-coated bioGNPs, and Lipofectamine2000-coated bioGNPs, **(b)** Cytotoxicity analysis – flow cytometric results of cytotoxcity using PI after 24 hrs, 72hrs, and 120 hrs incubation with nothing, CTAB-coated nanorods, Oligofectamine-coated bioGNPs, sc29528-coated bioGNPs, and Lipofectamine2000-coated bioGNPs, **(c)** Proliferation analysis - table summarizing initial cell count ($N_{initial}$), final cell count after 120 hrs (N_{final}), and calculated doubling times for cells containing nothing, Oligofectamine-coated bioGNPs, sc29528-coated bioGNPs, and Lipofectamine2000-coated bioGNPs.

In closing, biologically functional phospholipid-gold plasmonic bioGNP carriers have been designed that exhibit carrier capabilities, demonstrate improved nanoparticle stability, and show no cytotoxicity under physiological conditions. Successful demonstration of these advantages has been shown here using mammalian cell lines. In addition to these advantages, since bioGNPs are able to retain their unique optical properties under physiological conditions, bioGNPs should be particularly useful in a wide range of applications that utilize selective nanoplasmonic properties. BioGNPs are therefore expected to have important implications in advancing drug delivery, gene delivery, biomedical and molecular imaging, and therapeutics.

References

1. Skirtach, A. G., Javier, A. M., Kreft, O., Kohler, K., Alberola, A. P., Mohwald, H., Parak, W. J., Sukhorukov, G. B., Laser-Induced Release of Encapsulated Materials inside Living Cells, *Angew. Chem. Int. Ed., 45*, 4612 –4617 (2006).

2. Ren, L., Chow, G.M., Synthesis of NIR-Sensitive Au–Au2S Nanocolloids for Drug Delivery, *Materials Science and Engineering, C23*, 113–116 (2003).
3. Sershen, S. R., Westcott, S. L., Halas, N. J., West, J. L., Temperature-Sensitive Polymer–Nanoshell Composites for Photothermally Modulated Drug Delivery, *J. Biomed. Mater. Res., 51*, 293–298 (2000).
4. Wijaya, A., Schaffer, S.B., Pallares, I.G., Hamad-Schifferli, K., Selective Release of Multiple DNA Oligonucleotides from Gold Nanorods, *ACS Nano, 3*, 80 (2009).
5. Chen, C., Lin, Y., Wang, C., Tzeng, H., Wu, C., Chen, Y., Chen, C., Chen, L., Wu, Y., DNA-Gold Nanorod Conjugates for Remote Control of Localized Gene Expression by near Infrared Irradiation, *Journal of the Americal Chemical Society, 128*, 3709 (2006).
6. Horiguchi, Y., Niidome, T., Yamada, S., Nakashima, N., Niidome, Y., Expression of Plasmid DNA Released from DNA Conjugates of Gold Nanorods, *Chemistry Letters, 36*, 952–953 (2007).
7. Lee, S. E., Liu, G. L., Kim, F., Lee, L. P., Remote Optical Switch for Localized and Selective Control of Gene Interference, *Nanoletters, 9*, 562 (2009).
8. Barhoumi, A., Huschka, R., Bardhana, R., Knight, M.W., Halas, N.J., Light-Induced Release of DNA from Plasmon-Resonant Nanoparticles: Towards Light-Controlled Gene Therapy, *Chemical Physics Letters, 482*, 171 (2009).
9. Braun, G. B., Pallaoro, A., Wu, G., Missirlis, D., Zasadzinski, J.A., Tirrell, M., Reich, N.O., Laser-Activated Gene Silencing via Gold Nanoshell-siRNA Conjugates, *ACS Nano, 3*, 2007 (2009).
10. Nallathamby, P. D., Lee, K.J., Xu, X.N., Design of Stable and Uniform Single Nanoparticle Photonics for In Vivo Dynamics Imaging of Nanoenvironments of Zebrafish Embryonic Fluids, *ACS Nano, 2*, 1371–1380 (2008).
11. Copland, J. A., Eghtedari, M., Popov, V.L., Kotov, N., Mamedova, N., Motamedi, M., Oraevsky, A.A., Bioconjugated Gold Nanoparticles as a Molecular Based Contrast Agent: Implications for Imaging of Deep Tumors Using Optoacoustic Tomography, *Mol. Imaging Biol., 6*, 341 (2004).
12. Javier, D. J., Nitin, N., Roblyer, D.M.,Richards-Kortum, R., Metal-based Nanorods as Molecule-specific Contrast Agents for Reflectance Imaging in 3D Tissues, *Journal of Nanophotonics, 2*, 1 (2008).
13. Choi, Y., Park, Y., Kang, T., Lee, L.P., Selective and Sensitive Detection of Metal Ions by Plasmon Resonance Energy Transfer-based Nanospectroscopy, *Nature Nanotechnology, 4*, 742 (2009).
14. Huang, X., El-Sayed, I. H., Qian, W., El-Sayed, M. A., Cancer Cell Imaging and Photothermal Therapy in the Near-Infrared Region by Using Gold Nanorods, *Journal of the Americal Chemical Society, 128*, 2115 (2006).
15. Huang, Y. F., Sefah, K., Bamrungsap, S., Chang, H., Tan, W., Selective Photothermal Therapy for Mixed Cancer Cells Using Aptamer-Conjugated Nanorods, *Langmuir, 24*, 11860 (2008).
16. Pissuwan, D., Valenzuela, S. M., Killingsworth, M. C., Xu, X., Cortie, M., Targeted Destruction of Murine Macrophage Cells with Bioconjugated Gold Nanorods, *Journal of Nanoparticle Research, 9*, 1109–1124 (2007).
17. Choi, M., Stanton-Maxey, K. J., Stanley, J. K., Levin, C. S., Bardhan, R., Akin, D., Badve, S., Sturgis, J., Robinson, J. R., Bashir, R., Halas,, and N. J., C., S. E., A

Cellular Trojan Horse for Delivery of Therapeutic Nanoparticles into Tumors, *Nanoletters, 7*, 3759 (2007).
18. Loo, C., Hirsch, L., Lee, M., Chang, E., West, J., Halas, N., Drezek, R., Gold Nanoshell Bioconjugates for Molecular Imaging in Living Cells, *Opt. Lett., 30*, 1012 (2005).
19. Skrabalak, S. E. C., J.; Au, L.; Lu, X.; Li, X.; Xia, Y., Gold Nanocages for Biomedical Applications, *Advanced Materials, 19*, 3177–3184 (2007).
20. Gobin, A. M., O'Neal, D.P., Watkins, D.M., Halas, N.J., Drezek, R.A., West, J.L., Near Infrared Laser-tissue Welding using Nanoshells as an Exogenous Absorber., *Laser Surg. Med., 37*, 123 (2005).
21. Hauck, T. S., Jennings, T. L., Yatsenko, T., Kumaradas, J. C., Chan, W. C., Enhancing the Toxicity of Cancer Chemotherapeutics with Gold Nanorod Hyperthermia, *Advanced Materials, 20*, 3832–3838 (2008).
22. Norman, R. S., Stone, J. W., Gole, A., Murphy, C. J., Sabo-Attwood, T. L., Targeted Photothermal Lysis of the Pathogenic Bacteria, Pseudomonas aeruginosa, with Gold Nanorods, *Nanoletters, 8*, 302 (2008).
23. Zhang, D., Neumann, O., Wang, H., Yuwono, V.M., Barhoumi, A., Perham, M., Hartgerink, J.D., Wittung-, and Stafshede, P., Halas, N.J., Gold Nanoparticles Can Induce the Formation of Protein-based Aggregates at Physiological pH, *Nanoletters, 9*, 666 (2009).
24. Nikoobakht, B., El-Sayed, M. A., Preparation and Growth Mechanism of Gold Nanorods (NRs) Using Seed-Mediated Growth Method, *Chem. Mater., 15*, 1957 (2003).
25. Broderick, G., Craig, M., Metabolism of Peptides and Amino Acids During In Vitro Protein Degradation by Mixed Rumen Organisms, *J. Dairy Sci., 72*, 2540 (1989).
26. Cortesi, R., Esponito, E., Menegatti, E., Gambari, R., Nastruzzi, C., Effect of Cationic Liposome Composition on In vitro Cytotoxicity and Protective Effect on Carried DNA, *Int. J. Pharm., 139*, 69 (1996).
27. Ruissen, F., Le, M., Carroll, J.M., van der Valk, P.G.M., Schalkwijk, J., Differential Effects of Detergents on Keratinocyte Gene Expression, *J. Invest. Dermatol., 110*, 358–363 (1998).
28. Huff, T. B., Hansen, M.N., Cheng, J., Wei, A., Controlling the Cellular Uptake of Gold Nanorods, *Langmuir, 23*, 1596 (2007).
29. Niidome, Y., Honda, K., Higashimoto, K., Kawazumi, H., Yamada, S., Nakashima, N., Sasaki, Y., Ishida, Y., Kikuchi, J., Surface Modification of Gold Nanorods with Synthetic Cationic Lipids, *Chem. Commun., 36*, 3777 (2007).
30. Takahashi, H., Niidome, T., Kawano, T., Yamada, S., Niidome Y., Surface Modification of Gold Nanorods using Layer-by-layer Technique for Cellular Uptake, *J. Nanopart Res., 10*, 221 (2008).
31. Connor, E., Mwamuka, J., Gole, A., Murphy, C.J., Wyatt, M.D., Gold Nanoparticles are Taken up by Human Cells But Do Not Cause Acute Cytotoxicity, *Small, 1*, 325 (2005).
32. Wang, S., Lu, W., Tovmachenko, O., Rai, U., Yu, H., Ray, P.C., Challenge in Understanding Size and Shape Dependent Toxicity of Gold Nanomaterials in Human Skin Keratinocytes, *Chem. Phys. Lett., 463*, 145 (2008).

33. Wang, X., Nguyen, T., Gillespie, D., Jensen, R., Lu, Z., A Multifunctional and Reversibly Polymerizable Carrier for Efficient siRNA Delivery, *Biomaterials, 29*, 343 (2008).
34. Chiu, Y., Rana, T.M., siRNA Function in RNAi: A Chemical Modification Analysis, *RNA, 9*, 1034 (2003).
35. Niidome, T., Yamagata, M., Okamoto, Y., Akiyama, Y., Takahashi, H., Kawano, T., Katayama, Y., Niidome, Y., PEG-modified Gold Nanorods with a Stealth Character for In vivo Applications, *J. Controlled Release, 114*, 343 (2006).
36. Eghtedari, M., Liopo, A.V., Copland, J.A., Oraevsky, A.A., Motamedi, M., Engineering of Hetero-Functional Gold Nanorods for the in vivo Molecular Targeting of Breast Cancer Cells, *Nanoletters, 9*, 287 (2009).
37. Liao, H., Hafner, J.H., Gold Nanorod Bioconjugates, *Chem. Mater., 17*, 4636 (2005).
38. Leonov, A. P., Zheng, J., Clogston, J.D., Stern, S.T., Patri, A.K., Wei, A., Detoxification of Gold Nanorods by Treatment with Polystyrenesulfonate, *ACS Nano, 2*, 2481–2488 (2008).
39. Yu, C., Varghese, L., Irudayaraj, J., Surface Modification of Cetyltrimethylammonium Bromide-Capped Gold Nanorods to Make Molecular Probes, *Langmuir, 23*, 9114 (2007).
40. Orendorff, C. J., Alam, T.M., Sasaki, D.Y., Bunker, B.C., Voigt, J.A., Phospholipid-Gold Nanorod Composites, *ACS Nano, 3*, 971–983 (2009).
41. Gole, A., Murphy, C.J., Polyelectrolyte-Coated Gold Nanorods: Synthesis, Characterization and Immobilization, *Chem. Mater., 17*, 1325 (2005).
42. Bergan, D., Galbraith, T., Sloane, D.L., Gene Transfer In Vitro and In Vivo by Cationic Lipids Is Not Significantly Affected by Levels of Supercoiling of Reporter Plasmid, *Pharm. Res., 17*, 967 (2000).
43. Felgner, P. L., Tsai, Y.J., Sukhu, L., Wheeler, C.J., Manthorpe, M., Marshall, J., Cheng, S.H., Improved Cationic Lipid Formulations for Irt Vivo Gene Therapy, *Ann. N.Y. Acad. Sci., 772*, 126 (1995).
44. Madhusudan, S., Tamir, A., Bates, N., Flanagan, E., Gore, M.E., Barton, D.P.J., Harper, P., Seckl, M., Thomas, H., Lemoine, N.R., Charnock, M., Habib, N.A., Lechler, R., Nicholls, J., Pignatelli, M., Ganesan, T.S., A Multicenter Phase I Gene Therapy Clinical Trial Involving Intraperitoneal Administration of E1A-Lipid Complex in Patients with Recurrent Epithelial Ovarian Cancer Overexpressing HER-2/neu Oncogene, *Clin. Cancer Res., 10*, 2986–2996 (2004).
45. Rubin, J., Galanis, E., Pitot, H.C., Richardson, R.L., Burch, P.A., Charboneau, J.W., Reading, C.C., Lewis, B.D., Stahl, S., Akporiaye, E.T., Harris, D.T., Phase I Study of Immunotherapy of Hepatic Metastases of Colorectal Carcinoma by Direct Gene Transfer of an Allogeneic Histocompatibility Antigen, HLA-B7, *Gene Ther., 4*, 419 (1997).
46. Tompkins, S. M., Lo, C., Tumpey, T.M., Epstein, S.L., Protection Against Lethal Influenza Virus Challenge by RNA Interference In Vivo, *Proc. Natl. Acad. Sci. U.S.A., 101*, 8682 (2004).
47. Magin-Lachmann, C., Kotzamanis, G., D'Aiuto, L., Cooke, H., Huxley, C., Wagner, E., In Vitro and In Vivo Delivery of Intact BAC DNA - Comparison of Different Methods, *J. Gene Med., 6*, 195 (2004).

48. Gou, L., Murphy, C. J., Fine-Tuning the Shape of Gold Nanorods, *Chem. Mater., 17*, 3668 (2005).
49. Thomas, C. F., Luisi, P.L., RNA Selectively Interacts with Vesicles Depending on Their Size, *J. Phys. Chem. B, 109*, 14544 (2005).
50. Wang, R., Kovalchin, J.T., Muhlenkamp, P., Chandawarkar, R.Y., Exogenous Heat Shock Protein 70 Binds Macrophage Lipid Raft Microdomain and Stimulates Phagocytosis, Processing, and MHC-II Presentation of Antigens, *Blood, 107*, 1636 (2006).
51. Barnes, J. A., Dix, D. J., Collins, B. W., Luft, C., Allen, J. W., Expression of Inducible Hsp70 Enhances the Proliferation of MCF-7 Breast Cancer Cells and Protects Against the Cytotoxic Effects of Hyperthermia, *Cell Stress Chaperones, 6*, 316 (2001).

CHAPTER 5:
NANOPLASMONICS-ENABLED ON-DEMAND GENE SILENCING: RNAI APPROACH

RNA interference (RNAi) is an alternative method to the antisense DNA strategy to silence genes with sequence-specificity. Short interfering RNA (siRNA) are short double-stranded RNA sequences (~21 bp) that are capable of inducing silencing effects through the RNAi pathway. Similar its antisense DNA predecessor, siRNA also enables direct, sequence-specific silencing of genes, but also alone, lacks the temporal control necessary for precise manipulation. To meet these needs, nanoplasmonic optical antennae, utilized as nanoplasmonic gene switches, are specifically designed to be compatible with and capable of carrying siRNA, thereby combining the benefits of sequence-specificity with spatiotemporal manipulation and enabling on-demand gene silencing of endogenous intracellular genes by siRNA.

To enable on-demand control, siRNA duplexes are electrostatically attached to the cationic phospholipid bilayer of the nanoplasmonic gene switch (Fig. 5.1a). While siRNA duplexes are attached to nanoplasmonic gene switches, their interfering functionality is inactivated. Using light illumination as a remote trigger to destabilize the electrostatic interaction, siRNA duplexes are released and their functionality is "activated" (Fig 5.1b).

In this chapter, on-demand gene silencing of endogenous intracellular genes is demonstrated using siRNA. siRNA also signals the degradation of specifically targeted mRNA; however, degradation is through a different mechanism compared to antisense DNA. Here, siRNA duplexes are electrostatically attached to cationic phospholipid-gold nanoplasmonic gene switches and internalized in living cells (Fig. 5.1c). In the presence of continuous-wave illumination, the electrostatic interaction is destabilized and siRNA duplexes are released into the cytosol. The unbound siRNA duplexes sequentially trigger cytosolic RNA-inducing silencing complex (RISC) to unwind the duplexes, bind to complementary mature mRNA, and silence gene expression (Fig. 5.1c). Since key components of RISC have been discovered in both the nucleus and cytosol (1), another model (2) suggests that unbound siRNA duplexes transport to the nucleus. In the nucleus, siRNA duplexes trigger RISC to unwind the duplexes, bind to premature mRNA, and silence gene expression (Fig. 5.1d). Other models (2) also propose that RISC actively transports siRNA duplexes from the cytosol to the nucleus for degradation.

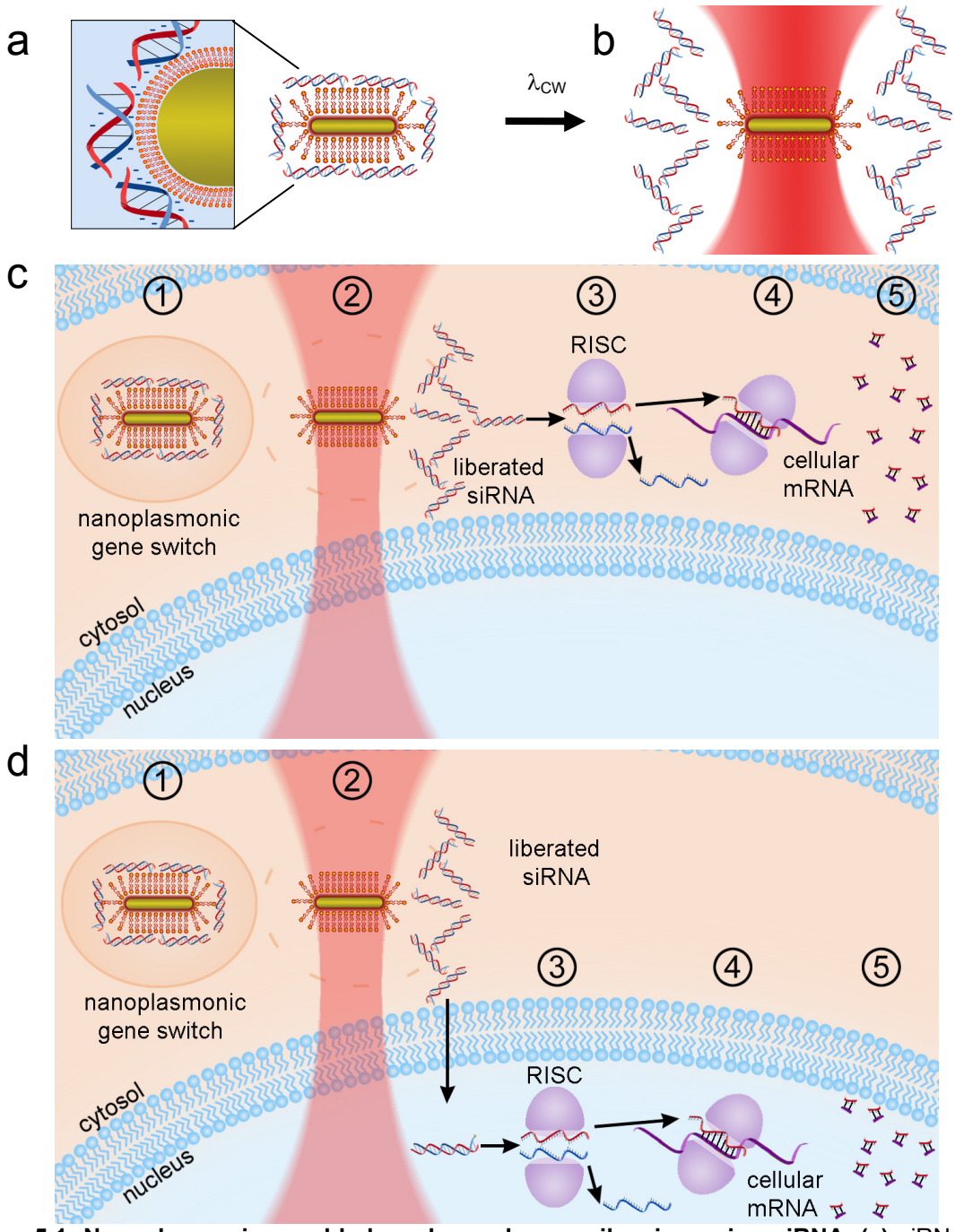

Figure 5.1. Nanoplasmonics-enabled on-demand gene silencing using siRNA. (a) siRNA duplexes electrostatically attached to the cationic phospholipid bilayer of the nanoplasmonic gene switch. **(b)** In the presence of continuous-wave illumination, the electrostatic interaction is destabilized and siRNA is released. **(c)** On-demand gene silencing using siRNA: Step 1 - siRNA duplexes electrostatically attached to nanoplasmonic gene switches and internalized in cells. Step 2 - in the presence of illumination, the electrostatic interaction is destabilized and siRNA is released. Step 3 - unbound siRNA triggers cytosolic RISC to unwind the duplex. Step 4 - cytosolic RISC binds single-stranded RNA to its complementary mRNA. Step 5 - gene-of-interest is silenced. **(d)** Alternative model: Step 1 and step 2 are the same. Step 3 unbound siRNA transports to the nucleus, where it is recognized and unwound by nuclear RISC. Step 4 - nuclear RISC binds single-stranded RNA to its complementary mRNA. Step 5 - gene-of-interest is silenced.

Methods

Synthesis of RNase-free CTAB-coated gold nanorods. Rnase-free gold nanorods of aspect ratios 2.5 and 4.0 were synthesized using a previously-reported RNase-free adaptation (3) of a seed-mediated growth method (4, 5). The asymmetric geometry resulted from synthesizing the nanorods in the presence of cetyltrimethylammonium bromide (CTAB). The concentration of CTAB-coated nanorods was confirmed by adjusting to an absorbance of 1 at the longitudinal plasmon resonance wavelength using UV-VIS spectroscopy (8453, Hewlett Packard). Aspect ratios were determined by scanning electron microscopy (Hitachi S-4500 FESEM) at 150,000X magnification. RNase activity in the supernatant solution was detected using an RNase activity kit (AM1964, Ambion) and was quantitatively measured over time using a fluorometer (Fluoromax-3, Horiba Jobin Yvon).

Synthesis of siRNA-conjugated nanoplasmonic gene switches. Commercially-available cationic phospholipid Oligofectamine was purchased from Invitrogen. 21-mer siRNA conjugated to fluorescein (FAM) dye (495 nm excitation, 520 nm emission) were purchased from Integrated DNA Technologies. 21-mer scrambled siRNA was purchased from Dharmacon. 21-mer siRNA targeted to IκB was purchased from Qiagen.

Firstly, the CTAB surfactant at the nanorod surface was exchanged with a cationic phospholipid bilayer to form biologically functional cationic phospholipids-gold nanoplasmonic carriers (bioGNPs). BioGNPs were synthesized and characterized as previously described (3). Here, bioGNPs are used as nanoplasmonic switches. In summary, to remove excess CTAB surfactant, 500 μL unmodified CTAB-coated nanorods (UV-VIS absorbance of 1) were centrifuged at 5000 rpm for 10 minutes. A 10 μL pellet was transferred to a new microcentrifuge tube, redispersed in 500 μL of nuclease-free water, briefly vortexed, and sonicated for 1 minute. To replace CTAB surfactant with a phospholipid bilayer membrane at the nanorod surface, nanorods were then centrifuged again at 5000 rpm for 10 minutes. A 10 μL pellet was transferred to a new microcentrifuge tube, resuspended in 50 μL of Oligofectamine, briefly vortexed, and sonicated for 1 minute.

After the CTAB coating was replaced with a cationic phospholipid coating, siRNA was then conjugated to the bioGNPs. To 500 μL of bioGNPs, 2 μL of 100 μM RNA siRNA was added. The solution was vortexed and allowed to incubate for 30 minutes. To remove excess siRNA from solution, bioGNPs were washed with nuclease-free water by centrifugation at 5000 rpm for 10 minutes and finally resuspended in 500 μL of nuclease-free water.

After preparation of siRNA-bioGNP conjugates, an absorbance of 0.2 was measured by UV-VIS (8453, Hewlett Packard). By comparing with the original nanorod's UV-VIS absorbance of 1, the concentration of bioGNPs was estimated to be approximately 1/5 the original nanorod concentration (approximately 6 μg/mL or 1.4E11 particles/mL).

For characterization of internalized siRNA-bioGNP conjugates, varying concentrations of approximately 3E11 particles/mL, 4E11 particles/mL, or 7E11 particles/mL (based on UV-VIS measurements) were used.

Thermal liberation of siRNA from nanoplasmonic gene switches. To each separate cell of an 8-cell micro sample holder (208-92086, Shimadzhu), 50 μL of siRNA-conjugated nanoplasmonic switches or unconjugated nanoplasmonic switches were added. Samples were simultaneously heated from 20°C to 70°C (10°C increment, 5 minutes) using a temperature-controlled UV-VIS spectrometer (2501, Shimadzhu). Absorbance spectra were collected for each sample at each temperature increment.

Cell preparation. The human cervical carcinoma cell line HeLa was purchased from the American Type Culture Collection (ATCC). Dulbecco's modified eagle's media (DMEM) formulated with high glucose and GlutaMAX was purchased from Invitrogen and was supplemented with 10% heat-inactivated fetal bovine serum. Unless specified otherwise, cells were seeded at an initial concentration of 20,000 cells/well in a 96-well plate, cultured in the supplemented media, and maintained in a 37 °C incubator with 5% CO2 humidified air.

Internalization of nanoplasmonic gene switches. The siRNA-conjugated bioGNPs were coated with cationic phospholipids for optimal internalization. Firstly, 1000 μL of siRNA-conjugated bioGNPs were concentrated into a 10 μL pellet by centrifugation at 5000 rpm for 20 minutes. The pellet was transferred to a new microcentrifuge tube and then resuspended in 25 μL of Oligofectamine. The solution was vortexed and allowed to incubate for 20 minutes. For higher concentrations of conjugates, the multiple tubes of conjugates were prepared the same as described above. After 20 minutes, 175 μL of nuclease-free water was added to each tube to dilute the concentration of free cationic phospholipids in solution. If there were multiple tubes, the tubes were then combined into a single tube. The conjugates were concentrated into a 0.5 μL pellet by centrifugation.

HeLa cells were washed once with Optimem media. The concentrated pellet was resuspended in 100 μL of Optimem media, gently mixed, and added to each well of the 96-well plate. The cells were allowed to incubate for 4 hours at 37°C.

Visualization of internalized nanoplasmonic gene switches by darkfield light microscopy. A 10% paraformaldehyde aqueous solution (15712-S) was purchased from Electron Microscopy Sciences and was used to prepare 4% stock solutions using 1X PBS. DAPI (D-1306) was purchased from Invitrogen.

For visualization purposes, HeLa cells were seeded onto 12 mm gridded glass coverslips (72265-12, Electron Microscopy Sciences) at 30,000 cells/well in a 24-well plate. Nanoplasmonic switches were internalized as described above. After internalization, cells were fixed by incubating cells with 2% paraformaldehyde per well for 10 minutes. Cell nuclei were stained with DAPI by incubating cells in 300 nM DAPI

per well for 5 minutes. 1X PBS was used to twice-wash the cells. The coverslip containing fix, adhered cells was then placed facedown and adhered to a microscope slide. Cells were located using the grids imprinted on the coverslips.

Darkfield scattering was visualized using an inverted microscope (Axiovert, Zeiss) at 40X magnification. Broadband white light was shined onto the adhered cells from an oblique angle using a darkfield condenser lens. The scattered light alone was collected using a microscope objective lens with a numerical aperture (NA) of 0.65 that was smaller than the NA (1.2-1.4) of the illumination condenser lens. DIC and DAPI were visualized using an upright fluorescence microscope (Axio Imager, Zeiss) at 40X magnification.

Conventional lipofection of siRNA. Optimem reduced-serum media and Lipofectamine 2000 were purchased from Invitrogen. 21-mer siRNA targeted to IκB was purchased from Qiagen.

Conventional lipofection of siRNA was carried out according to manufacturer's instructions. Briefly, HeLa cells were washed once with Optimem media. Cells were then incubated with 25 nM siRNA in Optimem media for 6 hours. After 6 hours, the media was replaced with fresh supplemented DMEM culture media. Cells were allowed to incubate for an additional 72 hours at 37°C.

For characterization of internalized siRNA, cells were incubated with 0 nM, 50 nM, 100 nM, or 200 nM siRNA in Optimem media for 6 hours. After 6 hours, the media was replaced with fresh supplemented DMEM culture media. Cells were allowed to incubate for an additional 72 hours at 37 °C.

On-demand gene silencing. After internalization of nanoplasmonic gene switches for 4 hours, the media was replaced with fresh supplemented DMEM culture media. The 96-well plate was placed in a CO_2-filled, sealed container, containing a high transmission glass window (NT45-661) purchased from Edmund Optics. Wells were illuminated from a top with 50 mW of 785 nm CW diode laser from Newport Corp. with a spot size of 2 mm (one quadrant of a well in a 96-well plate) for 15 minutes. After illumination, cells were allowed to incubate for an additional 72 hours at 37°C.

Direct immunostaining and flow cytometry analysis. Fluorescently-labeled antibodies recognizing IκB (sc-1643-AF488) were purchased from Santa Cruz Biotechnologies. Fluorescently-labeled normal mouse isotype antibodies (sc-3890) were also purchased from Santa Cruz Biotechnologies and were used as the negative control. Permeabilization buffer was prepared by adding 0.1% (w/v) saponin, 0.3% (w/v) Triton-X, and 0.1% (w/v) NaN_3 to Hank's Balanced Salt Solution (Invitrogen).

Cells were harvested, resuspended in 250 μL of 1X PBS, and fixed with 250 μL of 4% paraformaldehyde for 10 minutes. After 10 minutes, excess paraformaldehyde was removed by centrifuging and resuspending cells in 400 μL of permeabilization buffer (repeated twice). Cells were then counted to ensure all samples contained the same

number of cells prior to immunostaining. For 50,000 cells, 10 μL of antibody or isotype antibody were added. Cells were gently mixed and incubated at room temperature for 45 minutes. After 45 minutes, excess antibodies were removed by centrifuging and resuspending cells in 400 μL of permeabilization buffer. To remove permeabilization buffer, cells were finally centrifuged and resuspended in 500 μL of 1X PBS. LSRII flow cytometer (BD Biosciences) and FlowJo software (Tree Star, Ashland, Oregon) were used to analyze samples.

Results and Discussion

Gold nanorods were synthesized by modifying a seed-mediated growth approach (4, 5) to be free of RNase contamination (3). The resultant CTAB-coated gold nanorods were ensured to be free of RNases by detecting RNase activity over time (Fig. 5.2). Using an adaptation of vesicle-to-nanoparticle fusion, the cytotoxic CTAB at the nanorods' surface was then place-exchanged with biocompatible cationic phospholipids to form biologically functional cationic phospholipid-gold nanoplasmonic carriers (bioGNPs) (3) as described in Chapter 4. Negatively charged siRNA readily attached to the bioGNPs.

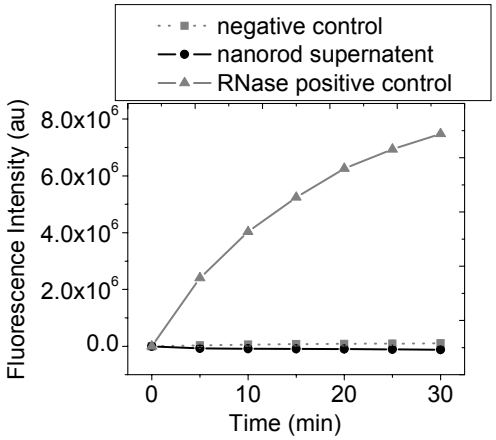

Figure 5.2. RNase-free characterization of gold nanorods. No RNase activity detected over time compared to the positive control.

The first step in demonstrating bioGNPs as nanoplasmonic gene switches was demonstrating the controlled thermal liberation of siRNA from the bioGNPs' surface. If siRNA dissociates from the cationic phospholipid bilayer at elevated temperatures, this unbinding event should change the dielectric constant of the medium locally surrounding the bioGNPs and therefore result in an observable shift in bioGNPs' longitudinal plasmon resonance wavelength (6, 7). A UV-VIS spectrometer containing a thermal-jacketed cell was used to evaluate the temperature-dependent absorbance of the bioGNP-containing solutions. Control bioGNPs without siRNA showed no shift in the longitudinal plasmon resonance wavelength at elevated temperatures (Fig. 5.3b), indicating that the phospholipid bilayer remained stable at elevated temperatures. In

contrast, siRNA-bioGNP conjugates showed a marked blue-shift in the longitudinal plasmon resonance wavelength at elevated temperatures due to the dissociation of siRNA from the bioGNPs' surface (Fig. 5.3a). Additionally, Figure 5.3c shows that the longitudinal plasmon resonance wavelength of the siRNA-bioGNPs blue-shifts with incrementing temperature until it eventually matches the longitudinal plasmon resonance wavelength of the control bioGNPs, strongly suggesting the complete dissociation of siRNA from the intact phospholipid bilayer at 70°C.

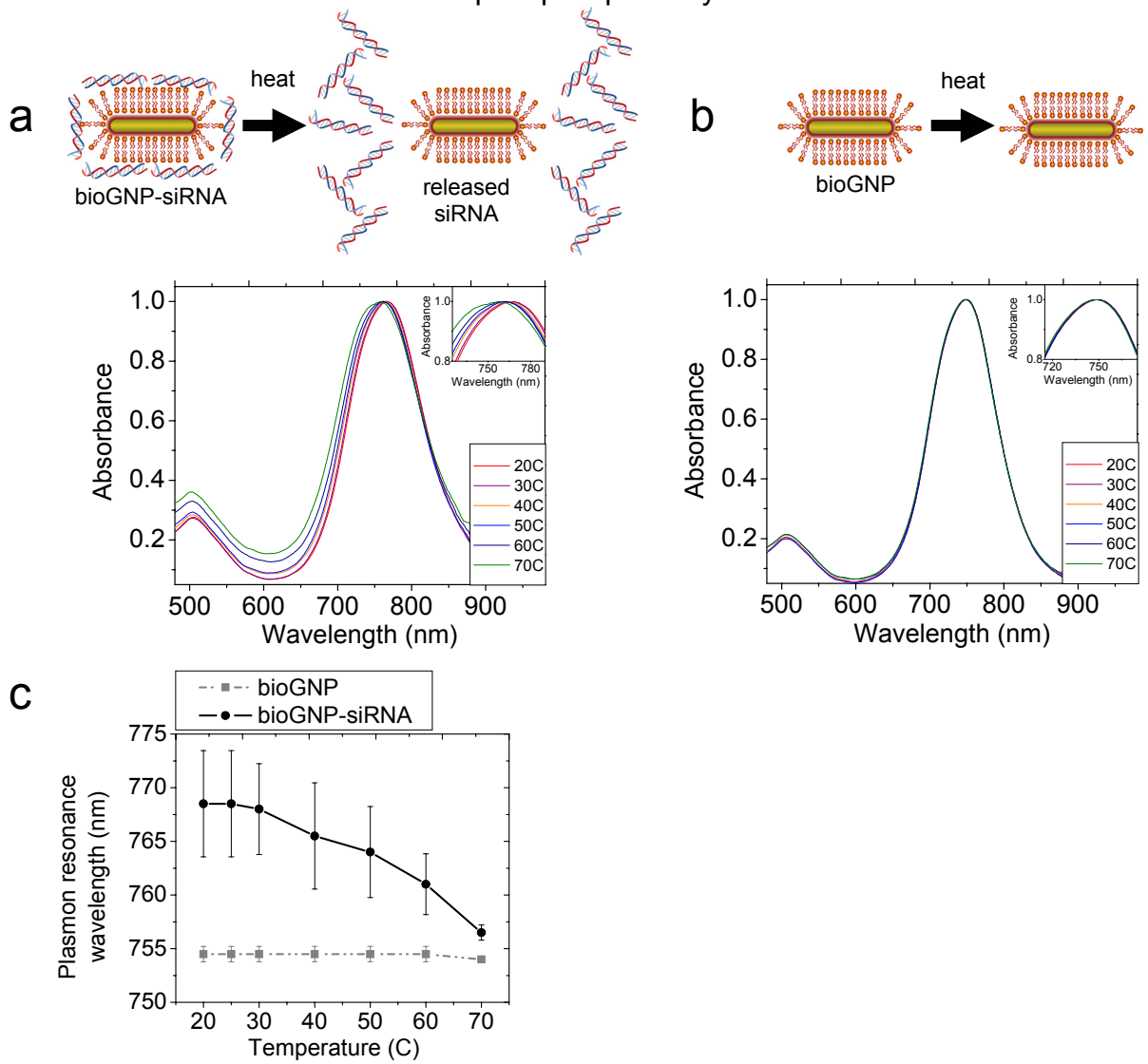

Figure 5.3. Thermal release of siRNA from bioGNPs. (a) UV-VIS spectra of siRNA-bioGNPs as temperature increased from 20° to 70°C. **(b)** UV-VIS spectra of control bioGNPs as temperature increased from 20° to 70°C. **(c)** Longitudinal plasmon resonance wavelength of bioGNPs and siRNA-bioGNPs as a function of temperature.

Having established that siRNA can be thermally dissociated from the cationic phospholipid bilayer, the controlled photothermal dissociation of siRNA was

investigated. Here, bioGNPs are demonstrated as nanoplasmonic gene switches. Fluorescently-labeled FAM-siRNAs were bound to nanoplasmonic gene switches and unbound FAM-siRNAs were then removed from the background solution by centrifugation. Light with wavelength 785 nm was used to illuminate nanoplasmonic gene switches. Under illumination, the bound FAM-siRNAs were released from these matching nanoplasmonic gene switches (Fig. 5.4) into solution and the fluorescent intensity was measured. A statistically significant increase in the fluorescent intensity was seen when these nanoplasmonic gene switches with a longitudinal plasmon resonance wavelength of 785 nm (Fig. 5.4b). In sharp contrast, no increase in fluorescent intensity was observed when mismatching nanoplasmonic gene switches with a longitudinal plasmon resonance wavelength of 660 nm, were illuminated with 785 nm light (Fig. 5.4b), confirming that FAM-siRNA remained attached to these mismatching nanoplasmonic gene switches.

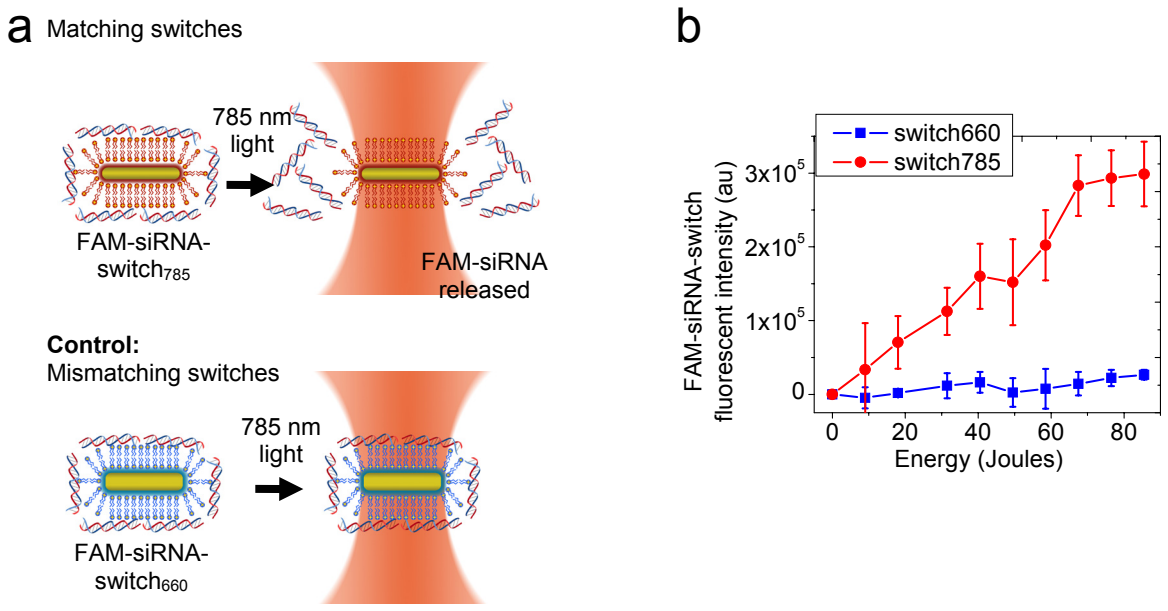

Figure 5.4. Photothermal release of siRNA from nanoplasmonic gene switches. (a) FAM-siRNA conjugated switches with longitudinal plasmon resonance 785 nm are illuminated with 785 nm light. siRNA is released. FAM-siRNA conjugated switches with longitudinal plasmon resonance 660 nm are illuminated with 785 nm light. No siRNA is released. **(b)** Graph of fluorescence versus light energy indicating photothermal release of FAM-labeled siRNA into solution.

Nanoplasmonic gene switches were then internalized in HeLa human cervical cancer cells. To visualize internalized nanoplasmonic gene switches, the cells were illuminated with unpolarized white light from an oblique angle using a darkfield condenser lens, and scattered light was collected using a transmission-mode darkfield microscope (Fig. 5.5). To locate cells' boundaries and nuclei, DIC images were overlaid with DAPI-stained images and placed adjacent to darkfield scattering images. It is clearly evident from Figure 5.5 that scattered light from cells containing nanoplasmonic gene switches (Fig. 5.5b) is easily differentiated from cells lacking nanoplasmonic gene

switches (Fig. 5.5a). Long-term viability/cytotoxicity and proliferation studies were conducted in Chapter 4 to ensure that internalized nanoplasmonic gene switches caused no adverse effects on cell behavior.

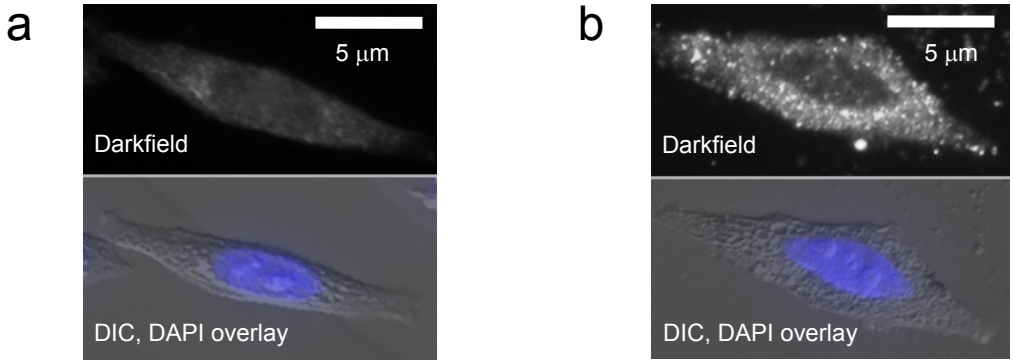

Figure 5.5. Visualization of internalized nanoplasmonic gene switches. (a) Darkfield scattering image of a HeLa cell without nanoplasmonic gene switches. DAPI-stained nuclei image overlaid with DIC image. **(b)** Darkfield scattering image of a HeLa cell containing nanoplasmonic gene switches. DAPI-stained nuclei image overlaid with DIC image.

To estimate the amount of internalized siRNA-conjugated nanoplasmonic gene switches, fluorescently-labeled FAM-siRNA were bound to nanoplasmonic gene switches and unbound FAM-siRNA were then removed from the background solution by centrifugation. Known concentrations of FAM-siRNA conjugated nanoplasmonic gene switches (7E11, 4E11, and 3E11 particles/mL based on UV-VIS measurements) were incubated with HeLa cells. Cells should internalize more nanoplasmonic switches in the presence of increasing concentrations. Fluorescent intensities of individual cells were then measured by flow cytometry (Fig. 5.6b) and a standard concentration curve of internalized FAM-siRNA conjugated nanoplasmonic switches was constructed (Fig. 5.6a). Fluorescence quenching by bioGNPs was not observed (3). To correlate the fluorescent intensities of the internalized FAM-siRNA conjugated nanoplasmonic gene switches to the amount of internalized FAM-siRNA, control cells were incubated with known concentrations of FAM-siRNA (50 nM, 100 nM, and 200 nM) for 5 hours. A standard concentration curve of internalized FAM-siRNA was then constructed based on flow cytometry analysis (Fig. 5.6a). These standard curves were later utilized to estimate the concentration of siRNA-conjugated nanoplasmonic switches necessary for gene silencing.

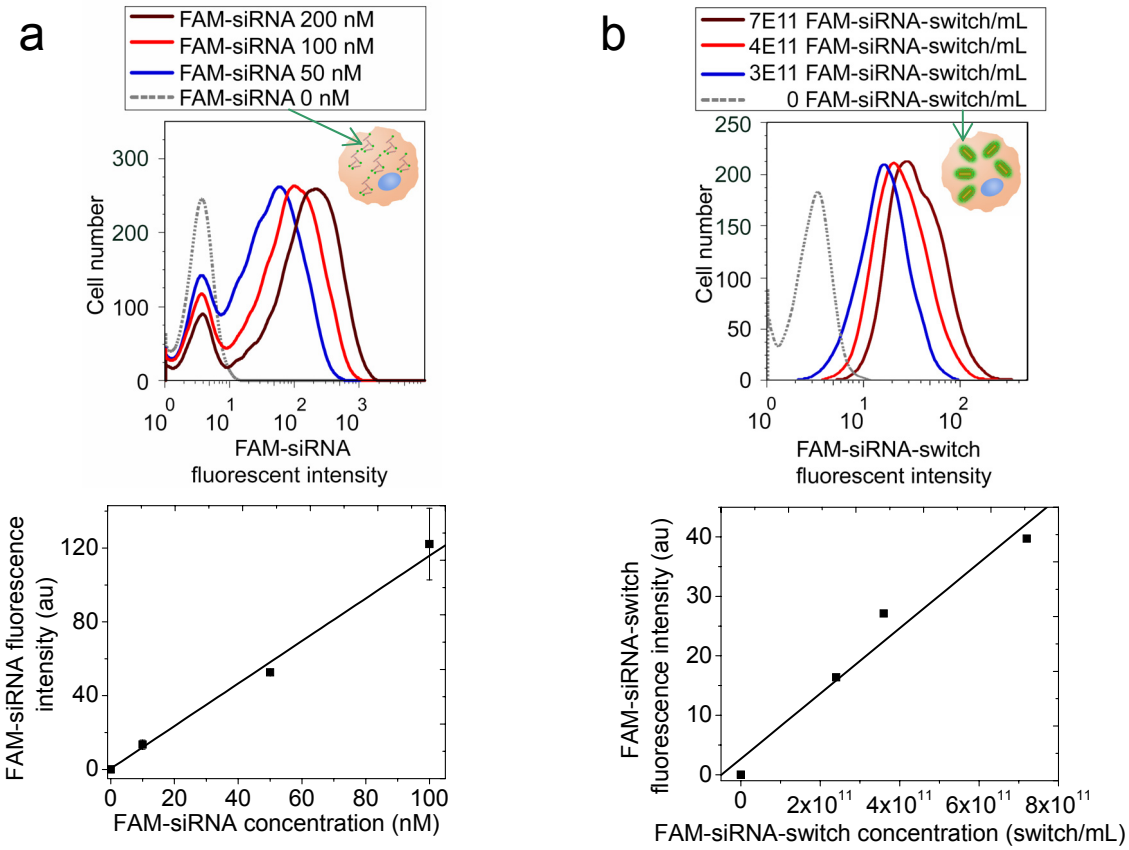

Figure 5.6. Characterization of intracellular siRNA and siRNA-switch. (a) Flow cytometry analysis of HeLa cells incubated with 0, 50, 100, and 200 nM of FAM-labeled siRNA. **(b)** Flow cytometry analysis of HeLa cells incubated with 0, 3E11, 4E11, and 7E11 FAM-labeled siRNA-switches.

After characterizing the internalization of siRNA-conjugated nanoplasmonic gene switches, on-demand gene silencing inhibitory IκB (IκB) of was conducted. Unbound siRNAs targeting IκB and strongly decreased protein expression levels by 50%, verifying silencing functionality (positive control Fig. 5.7a). The aforementioned standard curves (Fig. 5.6) were then used to estimate the concentration of nanoplasmonic gene switches to deliver equivalent concentrations of bound siRNA. The estimated siRNA-conjugated nanoplasmonic gene switches were then internalized in HeLa cells. Under light illumination, internalized nanoplasmonic gene switches should photothermally disrupt encapsulating endosomes (8-10) and photothermally release siRNA. The unbound siRNA should sequentially trigger the RNA-induced silencing complex (RISC) to unwind the duplex, bind to complementary messenger RNA (mRNA), and silence gene expression (11). On-demand gene silencing of IκB resulted in a 30% decrease in IκB expression (Fig. 5.7d). Scrambled siRNA-conjugated nanoplasmonic gene switches were also internalized in HeLa cells and illuminated to verify no non-specific, off-target down-regulation of IκB protein levels occurred (negative control Fig. 5.7c). No decrease in IκB protein levels were observed when nanoplasmonic gene switches alone (lacking siRNA) were illuminated (negative control Fig. 5.7b).

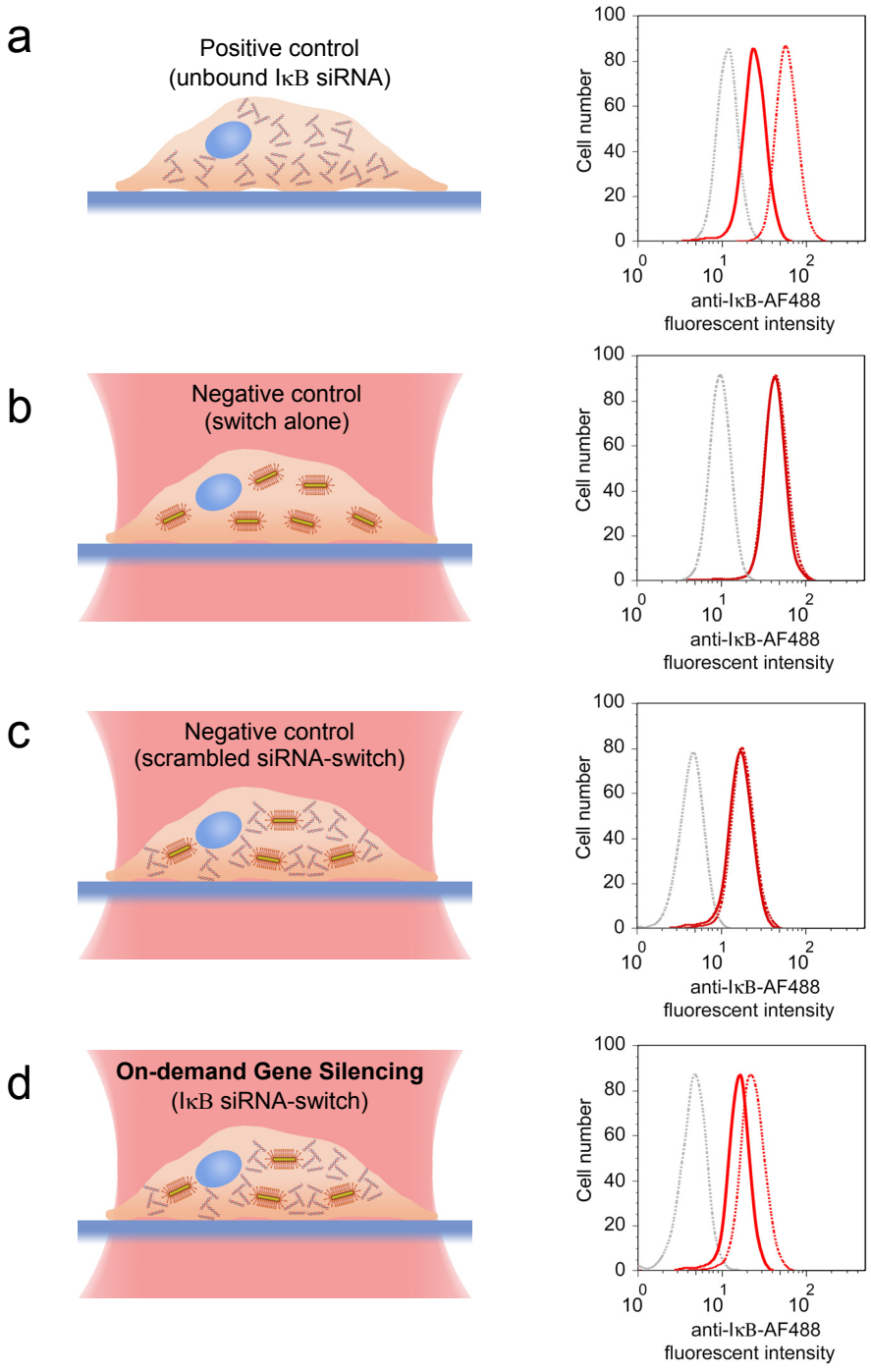

Figure 5.7. On-demand gene silencing of IκB using siRNA. To set dynamic range of flow cytometry fluorescence, grey dotted curve indicates negative isotype control for fluorescence and red dotted curve indicates positive control for fluorescence. Red solid line indicates: **(a)** Positive control for IκB silencing using unbound siRNA. **(b)** Negative control for IκB silencing using illuminated nanoplasmonic gene switches lacking siRNA. **(c)** Negative control for IκB silencing using illuminated nanoplasmonic gene switches with scrambled siRNA. **(d)** On-demand gene silencing of IκB.

In closing, nanoplasmonic gene switches, have been specifically designed to be compatible with and capable of carrying siRNA, thereby combining the benefits of sequence-specificity with spatiotemporal manipulation and enabling on-demand gene silencing of endogenous intracellular genes by siRNA.

References

1. Robb, G. B., Brown, K.M., Khurana, J., Rana, T.M., Specific and Potent RNAi in the Nucleus of Human Cells, *Nature Structural and Molecular Biology, 12*, 133 (2005).
2. Berezhna, S. Y., Supekova, L., Supek, F., Schultz, P.G., Deniz, A.A., siRNA in Human Cells Selectively Localizes to Target RNA sites, *Proceedings of the National Academy of Sciences, 103*, 7682 (2006).
3. Lee, S. E., Sasaki, D.Y., Perroud, T.D., Yoo, D., Patel, K.D., Lee, L.P., Biologically Functional Cationic Phospholipid-Gold Nanoplasmonic Carriers of RNA, *Journal of the Americal Chemical Society, 131*, 14066–14074 (2009).
4. Gou, L., Murphy, C. J., Fine-Tuning the Shape of Gold Nanorods, *Chem. Mater., 17*, 3668 (2005).
5. Nikoobakht, B., El-Sayed, M. A., Preparation and Growth Mechanism of Gold Nanorods (NRs) Using Seed-Mediated Growth Method, *Chem. Mater., 15*, 1957 (2003).
6. Sonnichsen, C., Plasmons in Metal Nanostructures, in *Physics*, Ludwig-Maximilians-University of Munich, pp. 104 (2001).
7. Huang, X., Gold Nanoparticles Used in Cancer Cell Diagnostics, Selective Photothermal Therapy and Catalysis of NADH Oxidation Reaction, in *Chemistry and Biochemistry*, Georgia Tech, pp. 209 (2006).
8. Lee, S. E., Liu, G. L., Kim, F., Lee, L. P., Remote Optical Switch for Localized and Selective Control of Gene Interference, *Nanoletters, 9*, 562 (2009).
9. Skirtach, A. G., Javier, A. M., Kreft, O., Kohler, K., Alberola, A. P., Mohwald, H., Parak, W. J., Sukhorukov, G. B., Laser-Induced Release of Encapsulated Materials inside Living Cells, *Angew. Chem. Int. Ed., 45*, 4612 –4617 (2006).
10. Wu, G., Mikhailovsky, A., Khant, H.A., Fu, C., Chiu, W., Zasadzinski, J.A., Remotely Triggered Liposome Release by Near-Infrared Light Absorption via Hollow Gold Nanoshells, *Journal of the American Chemical Society, 130*, 8175–8177 (2008).
11. Sontheimer, E., Assembly and Function of RNA Silencing Complexes, *Nature Reviews Molecular Cell Biology, 6*, 127 (2005).

CHAPTER 6:
CREATION OF A TRANSCRIPTIONAL PULSE BY ON-DEMAND GENE ACTIVATION AND REPRESSION

Transcriptional networks carry out essential functions in living organisms (1). Within these networks, genes are persistently transcribed in a long-lasting manner or transiently transcribed in a short-lived manner. In this way, transcriptional networks are dynamical systems, where genes are temporally regulated through dynamic interactions with other activating and repressing genes (Fig. 6.1a). Persistent and transient transcriptional activities serve important regulatory purposes, resulting in significantly different functions in developmental processes (2), immunological signal transduction pathways (3), and disease progression (4). Precise temporal control of a single gene's transcriptional activities, therefore, is of critical physiological interest.

Synthetic gene networks can be constructed to temporally control transcriptional activities (5-8). Notably, pulse-generating synthetic networks enable the generation of transient gene expression with defined duration (5). While these simplified models provide insight into more complex transcriptional networks, their direct correlation to naturally-occurring systems and their direct implications on biological function are unknown. The generation of a transcriptional pulse without permanent modification or simplification of the genome is therefore highly desirable.

Optically activated gold nanoparticles (9-28) (GNPs), referred to here as nanoplasmonic switches, can enable the realization of a pulse-generating system. Nanoplasmonic switches efficiently convert light energy into surface-localized heat, otherwise known as photothermal conversion (29-31), when the incident light is matched to their plasmon resonance wavelength. In particular, the NIR wavelength regime is well suited for biomedical applications since tissues and cells are essentially transparent at 800-1300 nm (32). Additionally, heat transfer from the surface of nanoplasmonic switches' to the surrounding cellular environment is highly localized, decaying exponentially within a few nanometers (14, 17, 29) and therefore is thought to have minimal adverse effects on cells. Among the GNPs, rod-shaped GNPs, well known as gold nanorods, are of particular interest for use as nanoplasmonic switches due to their large absorption cross-section, a narrow spectral width of the longitudinal plasmon resonance band, and tunability of the longitudinal plasmon resonance wavelength based on aspect ratio.

These unique optical properties of rod-shaped nanoplasmonic switches make them attractive candidates for temporal control of transcriptional networks in naturally-occurring systems. Because of their large surface area, nanoplasmonic switches are

ideal carriers of interfering oligonucleotides such as DNA, RNA, short hairpin RNA (shRNA), and short interfering RNA (siRNA). Interfering oligonucleotides enable sequence-specific silencing of intracellular genes, but alone, lack the temporal control necessary for precise manipulation. While attached to these carriers, oligonucleotides are in an inactive state. In the presence of light matched to their plasmon resonance wavelength, nanoplasmonic switches photothermally release oligonucleotides (9, 13, 20, 22, 25, 28) to locally interfere with gene expression (10, 14). In addition to the inhibitory effects of interfering oligonucleotides, exogenous foreign genes can be also introduced and expressed on-demand (11). Thus, nanoplasmonic switches combine the benefits of sequence-specificity and spatiotemporal control for precise manipulation of gene expression. Additionally, because their narrow longitudinal plasmon resonance bands can be spectrally separated, rod-shaped nanoplasmonic switches of different aspect ratios enable selective control of silencing multiple genes on-demand.

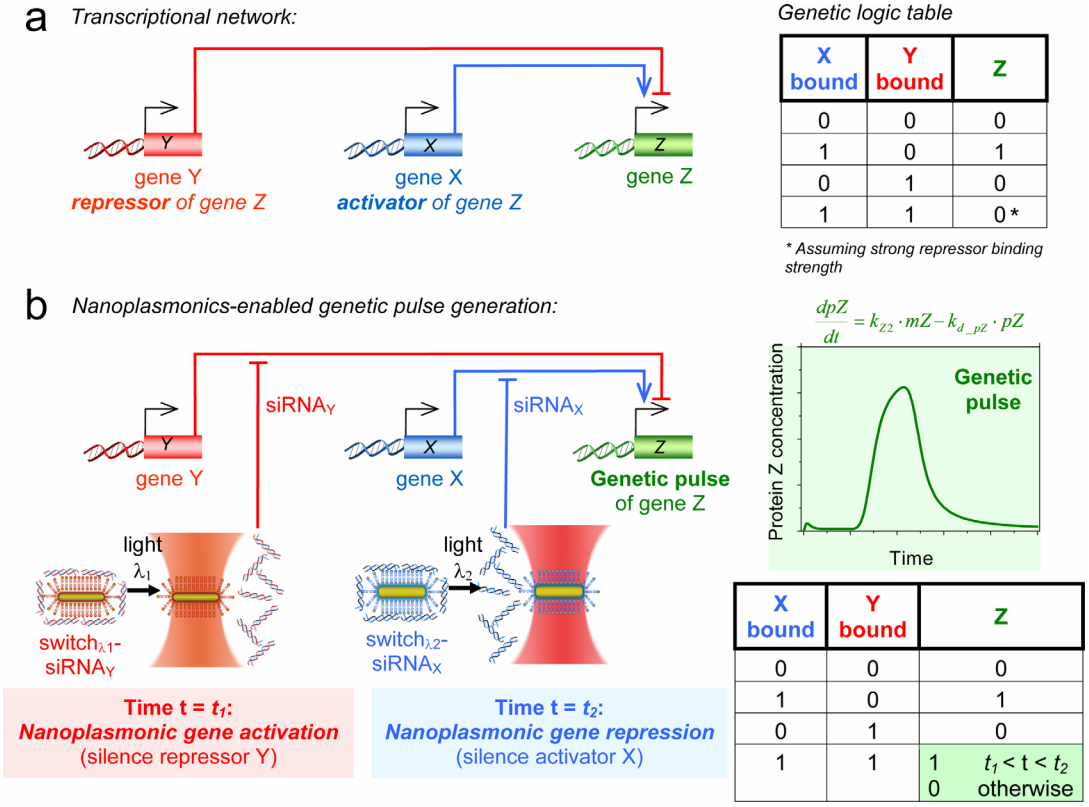

Figure 6.1. Concept of nanoplasmonics-enabled on-demand transcriptional pulse generation. (a) Typical transcriptional network. **(b)** nanoplasmonic switches of different aspect ratios used to selectively manipulate the binding activities of repressors and activators upstream from the target gene to generate a transcriptional pulse of target gene expression.

A transcriptional pulse of target gene expression can be generated by utilizing siRNA-conjugated nanoplasmonic switches of different aspect ratios to selectively manipulate the binding activities of repressors and activators upstream from the target gene. The repressor and activator binding kinetics are mathematically modeled here to generate a transcriptional pulse of target gene expression (Fig. 6.1b and Fig. 6.2). To

initiate the transcriptional pulse, living cells are illuminated with light wavelength λ_1 at time t_1. Light illumination sequentially causes the photothermal release of siRNA$_Y$ from nanoplasmonic switches of plasmon resonance λ_1, the silencing of the repressor Y, and the activation of the target gene Z (Fig. 6.1b). Since the target gene expression is consequently activated, on-demand gene silencing of the repressor is referred to here as "nanoplasmonic gene activation." To terminate the transcriptional pulse, living cells are then illuminated with light wavelength λ_2 at time t_2. Light illumination sequentially causes the photothermal release of siRNA$_X$ from nanoplasmonic switches of plasmon resonance λ_2, the silencing of the activator X, and the repression of the target gene Z (Fig. 6.1b). Since the target gene expression is resultantly repressed, the on-demand gene silencing of the activator is defined here as "nanoplasmonic gene repression." A genetic logic table summarizing this transcriptional pulse behavior is shown in Figure 6.1b.

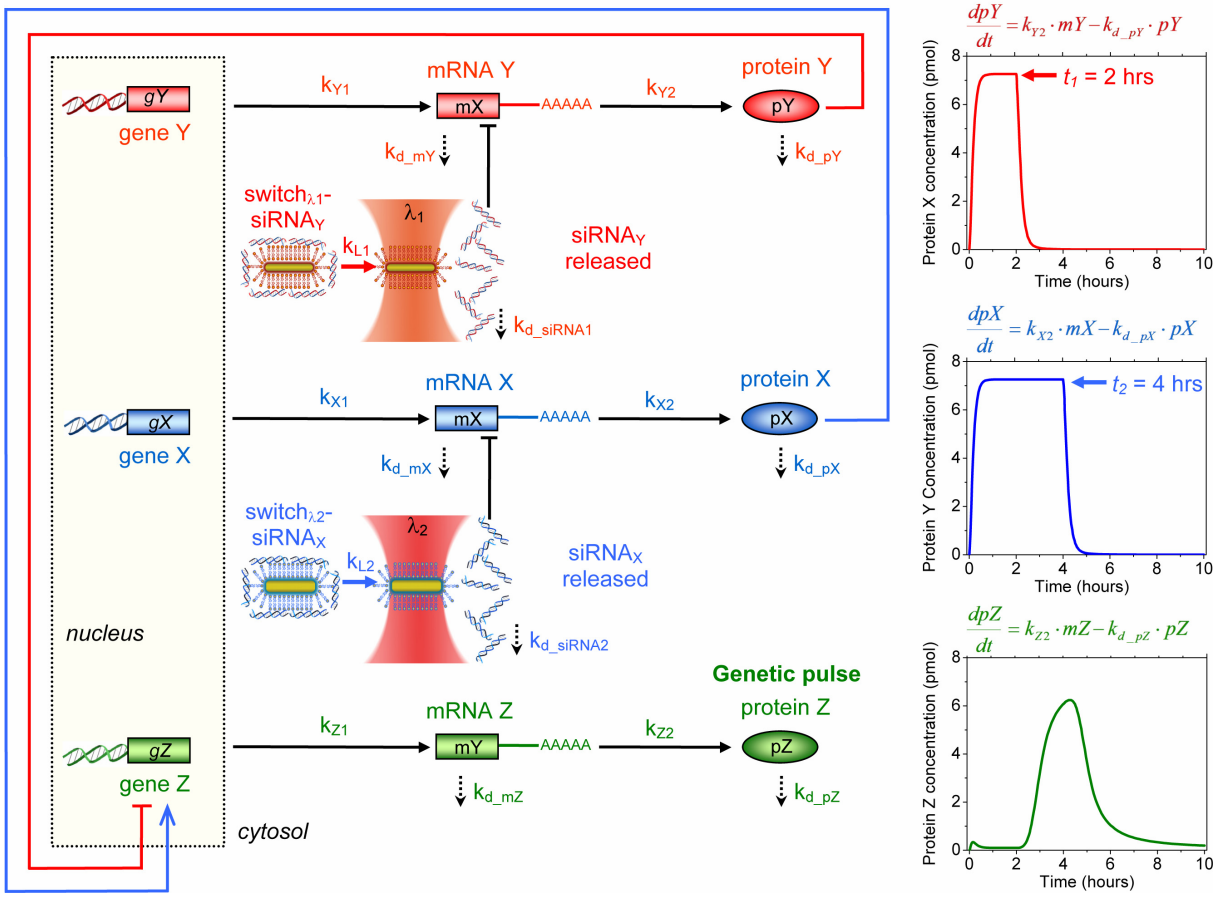

Figure 6.2. Mathematical model of on-demand transcriptional pulse generation. Changes in mRNA (*mX, mY, mZ*), and protein (*pX, pY, pZ*) concentrations over time for genes (*gX, gY, gZ*) are mathematically described and conceptually shown. At time t_1: repressor *Y* is silenced by on-demand release of siRNA$_Y$ from nanoplasmonic switch (longitudinal plasmon resonance λ_1). Downstream gene *Z* is activated (nanoplasmonic gene activation). At time t_2: activator *X* is silenced by on-demand release of siRNA$_X$ from nanoplasmonic switch (longitudinal plasmon resonance λ_2). Downstream gene *Z* is repressed (nanoplasmonic gene repression). Simulated concentration profiles over time for *pX*, *pY*, and *pZ*. Rates of mRNA synthesis are represented by k_{X1}, k_{Y1}, and k_{Z1}, and rates of protein synthesis are represented by k_{X2}, k_{Y2}, and k_{Z2}. Rates of mRNA degradation are represented by k_{d_mX}, k_{d_mY}, and k_{d_mZ}, and rates of protein degradation are represented by k_{d_pX}, k_{d_pY}, and k_{d_pZ}.

In this article, we present the on-demand generation of a transcriptional pulse of target gene expression by using nanoplasmonic switches of different aspect ratios to selectively manipulate the binding activities of repressors and activators upstream from the target gene. We first demonstrate that siRNA conjugated to nanoplasmonic switches of different aspect ratios can be selectively and independently liberated using the appropriate wavelength of light. We then show on-demand gene silencing of repressors and activators in living cells. We show that downstream translocation activities can be visualized in response to on-demand gene silencing of repressors and activators. We finally demonstrate nanoplasmonics-enabled transcriptional pulse generation of target gene expression by examining two target genes with different transcriptional activation profiles. Using nanoplasmonic control, the timing of genetic activities can be systematically varied on-demand. Equipped with new nanoplasmonic tools to directly probe the intracellular space, quantitative approaches should capture many dynamic activities within the living cell that were otherwise previously impossible to detect using conventional methods.

Methods

Mathematical model and simulation. A transcriptional pulse of target gene Z expression was generated by selectively manipulating the binding activities of repressor Y and activator X at gene Z's promoter region using nanoplasmonic switches. Activator and repressor binding kinetics were derived from the Michaelis-Menton and Hill input equations (1). Light-controlled gene silencing using siRNA-conjugated nanoplasmonic switches was modeled similarly to repressor binding kinetics.

Based on a two compartment model (33) shown in Figure 6.2, the transcriptional pulse can be described by the following differential equations (Eq. 1-8), which represent changes in mRNA (*mX*, *mY*, and *mZ*) and protein (*pX*, *pY*, and *pZ*) concentrations over time for each gene (*gX*, *gY*, and *gZ*).

$$\frac{dmX}{dt} = k_{X1} * gX * \left(\frac{\beta_X}{1 + \left(\frac{sirna2}{K_X} \right)^2} \right) - k_{d\_mX} * mX - k_{d\_sirna1\_mrna} * mX \quad (1)$$

$$\frac{dpX}{dt} = k_{X2} * mX - k_{d\_pX} * pX \quad (2)$$

$$\frac{dmY}{dt} = k_{Y1} * gY * \left(\frac{\beta_Y}{1 + \left(\frac{sirna1}{K_Y} \right)^2} \right) - k_{d\_mY} * mY - k_{d\_sirna2\_mrna} * mY \quad (3)$$

$$\frac{dpY}{dt} = k_{Y2} * mY - k_{d\_pY} * pY \quad (4)$$

$$\frac{dmZ}{dt} = k_{Z1} * gZ * \beta_Z * \left(\frac{1}{1 + \left(\frac{pY}{K_Y} \right)} \right) * \left(\frac{pX}{K_X + pX} \right) - k_{d\_mZ} * mZ \quad (5)$$

$$\frac{dpZ}{dt} = k_{Z2} * mZ - k_{d\_pZ} * pZ \quad (6)$$

$$\frac{dsirna1}{dt} = k_{L1} * gnp\_sirna1 - k_{d\_sirna1} * sirna1 \quad (7)$$

$$\frac{dsirna2}{dt} = k_{L2} * gnp\_sirna2 - k_{d\_sirna2} * sirna2 \quad (8)$$

Matlab™ software was used to numerically solve the differential equations for protein concentrations over time (Fig. 6.2). Nanoplasmonic gene activation at time t_1 followed by nanoplasmonic gene repression at time t_2 resulted in the generation of a transcriptional pulse of target gene Z expression, as shown in Figure 6.2 and summarized in Figure 6.1b. Rate constants for mRNA and protein degradation were approximated similarly to those previously reported in literature for a eukaryotic model (1). Target mRNA degradation rate by siRNA, as reported previously by others (34), was used in the model. Rate constants and initial values used in this mathematical model are reported in Tables 6.1.

Parameter	Value
Rate of mRNA synthesis (k_{X1}, k_{Y1}, k_{Z1})	1 pmol/day
Rate of protein sythesis (k_{X2}, k_{Y2}, k_{Z2})	100000 pmol/day
Half life of eukaryotic mRNA ($\tau_{1/2}$)	1 hr=0.042 day
Half life of eukaryotic protein ($\tau_{1/2}$)	2 hrs=0.083 day
Rate of mRNA degradation (k_{d_mX}, k_{d_mY}, k_{d_mZ})	16.5 days^{-1}
Rate of protein degradation (k_{d_pX}, k_{d_pY}, k_{d_pZ})	8.4 days^{-1}
Gene concentration (gX, gY, gZ)	10 pmol
Probability that activator is bound (β)	1
Hill coefficients (Kx, Ky)	1
Rate of siRNA degradation (k_{d_sirna})	0.34 day^{-1}
Rate of target mRNA degradation by siRNA (k_{d_rnai})	16.6 days^{-1}
Initial concentration of siRNA on nanoplasmonic switches	0.001 pmol

Table 6.1. Kinetic rates and initial values used in mathematical model of a transcriptional pulse generated using nanoplasmonic switches.

Several assumptions were made in this mathematical model. It was assumed no siRNA was released when light illumination did not match the plasmon resonance wavelength of the nanoplasmonic switches. It was also assumed that all siRNA on the nanoplasmonic switches were released at once upon light illumination of the correct wavelength. Since the model's timescale was on the order of hours, it was assumed that nanoplasmonic switches did not degrade in this timeframe and therefore the concentration of nanoplasmonic switches remained the same. Due to the tight packing of siRNA on the nanoplasmonic switches, steric hinderances inhibited nuclease degradation of siRNA while siRNA was attached to the nanoplasmonic switches (35). Once siRNA was released from the nanoplasmonic switches using light, the siRNA degraded with degradation rates as reported previous literature (34).

Synthesis of RNase-free CTAB-coated gold nanorods. Rnase-free gold nanorods of aspect ratios 2.5 and 4.0 were synthesized using a previously-reported RNase-free adaptation (36) of a seed-mediated growth method (37, 38). The asymmetric geometry resulted from synthesizing the nanorods in the presence of cetyltrimethylammonium bromide (CTAB). The concentration of CTAB-coated nanorods was confirmed by adjusting to an absorbance of 1 at the longitudinal plasmon resonance wavelength using UV-VIS spectroscopy (8453, Hewlett Packard). Aspect ratios were determined by scanning electron microscopy (Hitachi S-4500 FESEM) at 150,000X magnification. RNase activity in the supernatant solution was detected using an RNase activity kit (AM1964, Ambion) and was quantitatively measured over time using a fluorometer (Fluoromax-3, Horiba Jobin Yvon).

Synthesis of siRNA-conjugated nanoplasmonic gene switches. Commercially-available cationic phospholipid Oligofectamine was purchased from Invitrogen. 21-mer siRNA conjugated to fluorescein (FAM) dye (495 nm excitation, 520 nm emission) were purchased from Integrated DNA Technologies. 21-mer scrambled siRNA was purchased from Dharmacon. 21-mer siRNA targeted to NF-κB and IκB were purchased from Qiagen.

Firstly, the CTAB surfactant at the nanorod surface was exchanged with a cationic phospholipid bilayer to form biologically functional cationic phospholipids-gold nanoplasmonic carriers (bioGNPs). BioGNPs were synthesized and characterized as previously described (36). Here, bioGNPs are used as nanoplasmonic switches. In summary, to remove excess CTAB surfactant, 500 μL unmodified CTAB-coated nanorods (UV-VIS absorbance of 1) were centrifuged at 5000 rpm for 10 minutes. A 10 μL pellet was transferred to a new microcentrifuge tube, redispersed in 500 μL of nuclease-free water, briefly vortexed, and sonicated for 1 minute. To replace CTAB surfactant with a phospholipid bilayer membrane at the nanorod surface, nanorods were then centrifuged again at 5000 rpm for 10 minutes. A 10 μL pellet was transferred to a new microcentrifuge tube, resuspended in 50 μL of Oligofectamine, briefly vortexed, and sonicated for 1 minute.

After the CTAB coating was replaced with a cationic phospholipid coating, siRNA was then conjugated to the bioGNPs. To 500 μL of bioGNPs, 2 μL of 100 μM RNA siRNA

was added. The solution was vortexed and allowed to incubate for 30 minutes. To remove excess siRNA from solution, bioGNPs were washed with nuclease-free water by centrifugation at 5000 rpm for 10 minutes and finally resuspended in 500 μL of nuclease-free water.

For generating the transcriptional pulse: IκB siRNA was conjugated to bioGNPs with plasmon resonance wavelength 785 nm. NF-κB siRNA was conjugated to bioGNPs with plasmon resonance wavelength 660 nm.

After preparation of siRNA-bioGNP conjugates, an absorbance of 0.2 was measured by UV-VIS (8453, Hewlett Packard). By comparing with the original nanorod's UV-VIS absorbance of 1, the concentration of bioGNPs was estimated to be approximately 1/5 the original nanorod concentration (approximately 6 μg/mL or 1.4E11 particles/mL).

For characterization of internalized siRNA-bioGNP conjugates, varying concentrations of approximately 3E11 particles/mL, 4E11 particles/mL, or 7E11 particles/mL (based on UV-VIS measurements) were used.

Optical setup. An 80 mW 785 nm CW diode laser (Newport Corp.) and a 60 mW 660 nm CW diode laser (Newport Corp.) were co-aligned such that their beams simultaneously overlapped. Firstly, both lasers were positioned parallel to each other on a manually-adjustable xyz stage. A dichroic mirror (Omega Optical) was positioned below the 785 nm laser. A shortpass filter (Omega Optical) was placed below the 660 nm laser. To make the two beams orthogonal to each other, the 660 nm laser beam was reflected 90° towards the direction of the other laser by using the shortpass filter as a reflector. The dichroic mirror transmitted the 785 nm laser beam and reflected the 660 nm laser beam another 90° such that both beams simultaneously overlapped and co-aligned with each other.

Photothermal liberation of siRNA from nanoplasmonic gene switches. To a 2 mm path length quartz cuvette (3-2.45-Q-2, Starna Cells Inc.), 50 μL of FAM-siRNA-conjugated nanoplasmonic gene switches with 660 nm plasmon resonance wavelength or FAM-siRNA-conjugated nanoplasmonic gene switches with 785 nm plasmon resonance wavelength were added. Using the optical setup described above, the samples were illuminated from a top with 50 mW of either 785 nm or 660 nm light with a spot size of 2 mm. During illumination, fluorescence emission spectra were collected at 2 minute intervals for each sample using a fluorometer (Fluoromax-3, Horiba Jobin Yvon). A shortpass filter was positioned in front of the fluorometer's detector to block the detector from the laser sources.

Cell preparation. The human cervical carcinoma cell line HeLa was purchased from the American Type Culture Collection (ATCC). Dulbecco's modified eagle's media (DMEM) formulated with high glucose and GlutaMAX was purchased from Invitrogen and was supplemented with 10% heat-inactivated fetal bovine serum. Unless specified otherwise, cells were seeded at an initial concentration of 20,000 cells/well in a 96-well

plate, cultured in the supplemented media, and maintained in a 37 °C incubator with 5% CO2 humidified air.

Internalization of nanoplasmonic gene switches. The siRNA-conjugated bioGNPs were coated with cationic phospholipids for optimal internalization. Firstly, 1000 μL of siRNA-conjugated bioGNPs were concentrated into a 10 μL pellet by centrifugation at 5000 rpm for 20 minutes. The pellet was transferred to a new microcentrifuge tube and then resuspended in 25 μL of Oligofectamine. The solution was vortexed and allowed to incubate for 20 minutes. For higher concentrations of conjugates, the multiple tubes of conjugates were prepared the same as described above. After 20 minutes, 175 μL of nuclease-free water was added to each tube to dilute the concentration of free cationic phospholipids in solution. If there were multiple tubes, the tubes were then combined into a single tube. The conjugates were concentrated into a 0.5 μL pellet by centrifugation.

HeLa cells were washed once with Optimem media. The concentrated pellet was resuspended in 100 μL of Optimem media, gently mixed, and added to each well of the 96-well plate. The cells were allowed to incubate for 4 hours at 37°C.

Visualization of internalized nanoplasmonic gene switches by darkfield light microscopy. A 10% paraformaldehyde aqueous solution (15712-S) was purchased from Electron Microscopy Sciences and was used to prepare 4% stock solutions using 1X PBS. DAPI (D-1306) was purchased from Invitrogen.

For visualization purposes, HeLa cells were seeded onto 12 mm gridded glass coverslips (72265-12, Electron Microscopy Sciences) at 30,000 cells/well in a 24-well plate. Nanoplasmonic switches were internalized as described above. After internalization, cells were fixed by incubating cells with 2% paraformaldehyde per well for 10 minutes. Cell nuclei were stained with DAPI by incubating cells in 300 nM DAPI per well for 5 minutes. 1X PBS was used to twice-wash the cells. The coverslip containing fix, adhered cells was then placed facedown and adhered to a microscope slide. Cells were located using the grids imprinted on the coverslips.

Darkfield scattering was visualized using an inverted microscope (Axiovert, Zeiss) at 40X magnification. Broadband white light was shined onto the adhered cells from an oblique angle using a darkfield condenser lens. The scattered light alone was collected using a microscope objective lens with a numerical aperture (NA) of 0.65 that was smaller than the NA (1.2-1.4) of the illumination condenser lens. DIC and DAPI were visualized using an upright fluorescence microscope (Axio Imager, Zeiss) at 40X magnification.

Conventional lipofection of siRNA. Optimem reduced-serum media and Lipofectamine 2000 were purchased from Invitrogen. 21-mer siRNA targeted to NF-κB and IκB was purchased from Qiagen.

Conventional lipofection of siRNA was carried out according to manufacturer's instructions. Briefly, HeLa cells were washed once with Optimem media. Cells were then incubated with 25 nM siRNA in Optimem media for 6 hours. After 6 hours, the media was replaced with fresh supplemented DMEM culture media. Cells were allowed to incubate for an additional 72 hours at 37 °C.

For characterization of internalized siRNA, cells were incubated with 0 nM, 50 nM, 100 nM, or 200 nM siRNA in Optimem media for 6 hours. After 6 hours, the media was replaced with fresh supplemented DMEM culture media. Cells were allowed to incubate for an additional 72 hours at 37 °C.

On-demand gene silencing of IκB and NF-κB. After internalization of siRNA-conjugated (IκB or NF-κB siRNA) nanoplasmonic gene switches for 4 hours, the media was replaced with fresh supplemented DMEM culture media. The 96-well plate was placed in a CO_2-filled, sealed container, containing a high transmission glass window (NT45-661) purchased from Edmund Optics. Firstly, wells were illuminated from a top with 50 mW of 785 nm CW diode laser from Newport Corp. with a spot size of 2 mm (one quadrant of a well in a 96-well plate) for 15 minutes. Two hours after initial illumination with 785 nm light, wells were illuminated from a top with 50 mW of 660 nm CW diode laser from Newport Corp. with a spot size of 2 mm (one quadrant of a well in a 96-well plate) for 15 minutes. After illumination, cells were allowed to incubate for an additional 72 hours at 37 °C.

For IP-10 and RANTES studies, the media was replaced with fresh supplemented DMEM culture media containing 3 μm monensin (M5273, Sigma) 48 hours after illumination. The cells were allowed to incubate for an additional 24 hours at 37 °C.

Direct immunostaining for flow cytometry analysis. Fluorescently-labeled antibodies recognizing NF-κB (sc-8008-PE) and IκB (sc-1643-AF488, sc-945-AF488) were purchased from Santa Cruz Biotechnologies. Fluorescently-labeled normal mouse isotype antibodies (sc-2866, sc-3890, and sc-45068) were also purchased from Santa Cruz Biotechnologies and were used as negative controls. Fluorescently-labeled antibodies recognizing IP-10 and RANTES, and appropriate isotype controls were purchased from R&D Systems. Permeabilization buffer, for use with NF-κB and IκB antibodies, was prepared by adding 0.1% (w/v) saponin, 0.3% (w/v) Triton-X, and 0.1% (w/v) NaN_3 to Hank's Balanced Salt Solution (Invitrogen). Permeabilization buffer, for use with IP-10 and RANTES antibodies, was prepared by adding 0.1% (w/v) saponin and 0.06% (w/v) NaN_3 to Hank's Balanced Salt Solution (Invitrogen).

Cells were harvested, resuspended in 250 μL of 1X PBS, and fixed with 250 μL of 4% paraformaldehyde for 10 minutes. After 10 minutes, excess paraformaldehyde was removed by centrifuging and resuspending cells in 400 μL of permeabilization buffer (repeated twice). Cells were then counted to ensure all samples contained the same number of cells prior to immunostaining. For 50,000 cells, 10 μL of antibody or isotype

antibody were added. Cells were gently mixed and incubated at room temperature for 45 minutes. After 45 minutes, excess antibodies were removed by centrifuging and resuspending cells in 400 μL of permeabilization buffer. To remove permeabilization buffer, cells were finally centrifuged and resuspended in 500 μL of 1X PBS. LSRII flow cytometer (BD Biosciences) and FlowJo software (Tree Star, Ashland, Oregon) were used to analyze samples.

Direct immunostaining for NF-κB translocation studies by fluorescence microscopy. 72 hours after on-demand gene silencing of IκB or NF-κB using siRNA, cells (adhered to glass coverslips) were fixed in cold 50% methanol for 3 minutes on ice followed by cold 100% methanol for 15 minutes on ice. For three times, cells were washed with and incubated in 1X PBS for 5 minutes on a rocker at speed ~100 rpm. Cells were blocked with 5% normal mouse serum (01-6501, Invitrogen) in 1X PBS for 30 minutes on a rocker at speed ~100 rpm. For two times, cells were washed with and incubated in 1X PBS for 5 minutes on a rocker at speed ~100 rpm. Cells were then incubated in 300 nM DAPI (D1306, Invitrogen) in 1X PBS for 5 minutes in the dark on a rocker at speed ~100 rpm. Cells were washed with and incubated in 1X PBS for 5 minutes on a rocker at speed ~100 rpm. To 200 μL of 1X PBS, 60 mL of anti-NF-κB (sc8008 AF488, Santa Cruz Biotechnologies) was added. Cells were allowed to incubate for 2 hours in the dark on a rocker at speed ~100 rpm. For three times, cells were washed with and incubated in 1X PBS for 5 minutes on a rocker at speed ~100 rpm. Coverslip containing fixed, stained adhered cells was finally placed facedown on a microscope slide, sealed with clear nail polish, and imaged using fluorescence microscopy.

Results and Discussion

Gold nanorods were synthesized by modifying a seed-mediated growth approach (37, 38) to be free of RNase contamination (36). The resultant CTAB-coated gold nanorods were ensured to be free of RNases by detecting RNase activity over time (Chapter 5). Using an adaptation of vesicle-to-nanoparticle fusion, the cytotoxic CTAB at the nanorods' surface was then place-exchanged with biocompatible cationic phospholipids to form biologically functional cationic phospholipid-gold nanoplasmonic carriers (bioGNPs) (36) as described in Chapter 4. Negatively charged siRNA readily attached to the bioGNPs.

The first stage in nanoplasmonics-enabled transcriptional pulse generation was the selective and independent photothermal dissociation of siRNA. Here, bioGNPs are demonstrated as nanoplasmonic switches. In the presence of incident light that is matched to the nanoplasmonic switches' longitudinal plasmon resonance wavelength, the conduction band electrons of the nanoplasmonic switches collectively oscillate in phase on resonance and subsequently make collisions with the metal lattice, thereby dissipating heat (31). Since this photothermal conversion of light energy into heat is highly localized to the surface of the nanoplasmonic switches (14, 17, 29), this heat

should dissociate the siRNA from the cationic phospholipid bilayer. Additionally, since their narrow longitudinal plasmon resonance bands are spectrally separated as shown in Fig. 6.3a, nanoplasmonic switches of different aspect ratios should be excited independently of each other using the appropriate wavelength of light (13). Fluorescently-labeled FAM-siRNAs were bound to nanoplasmonic switches and unbound FAM-siRNAs were then removed from the background solution by centrifugation. Light with wavelength 785 nm was initially used to illuminate nanoplasmonic switches. Under illumination, the bound FAM-siRNAs were released from the matching nanoplasmonic switches into solution and the fluorescent intensity was measured. A statistically significant increase in the fluorescent intensity was seen when matching nanoplasmonic switches with a longitudinal plasmon resonance wavelength of 785 nm (UV-VIS spectra Fig. 6.3a) and an aspect ratio of 4.0 (SEM images Fig. 6.3b) were illuminated, strongly suggesting that bound FAM-siRNA were photothermally liberated from these matching nanoplasmonic switches into solution (Fig. 6.3c). In sharp contrast, no increase in fluorescent intensity was observed when mismatching nanoplasmonic switches with a longitudinal plasmon resonance wavelength of 660 nm (UV-VIS absorbance spectra Fig. 6.3a) and an aspect ratio of 2.5 (SEM images Fig. 6.3b) were illuminated with 785 nm light, confirming that FAM-siRNA remained attached to these mismatching nanoplasmonic switches (Fig. 6.3c). It is clearly evident from Figure 6.3c that bound siRNA can be selectively and independently liberated from nanoplasmonic switches that are matched to the incident light.

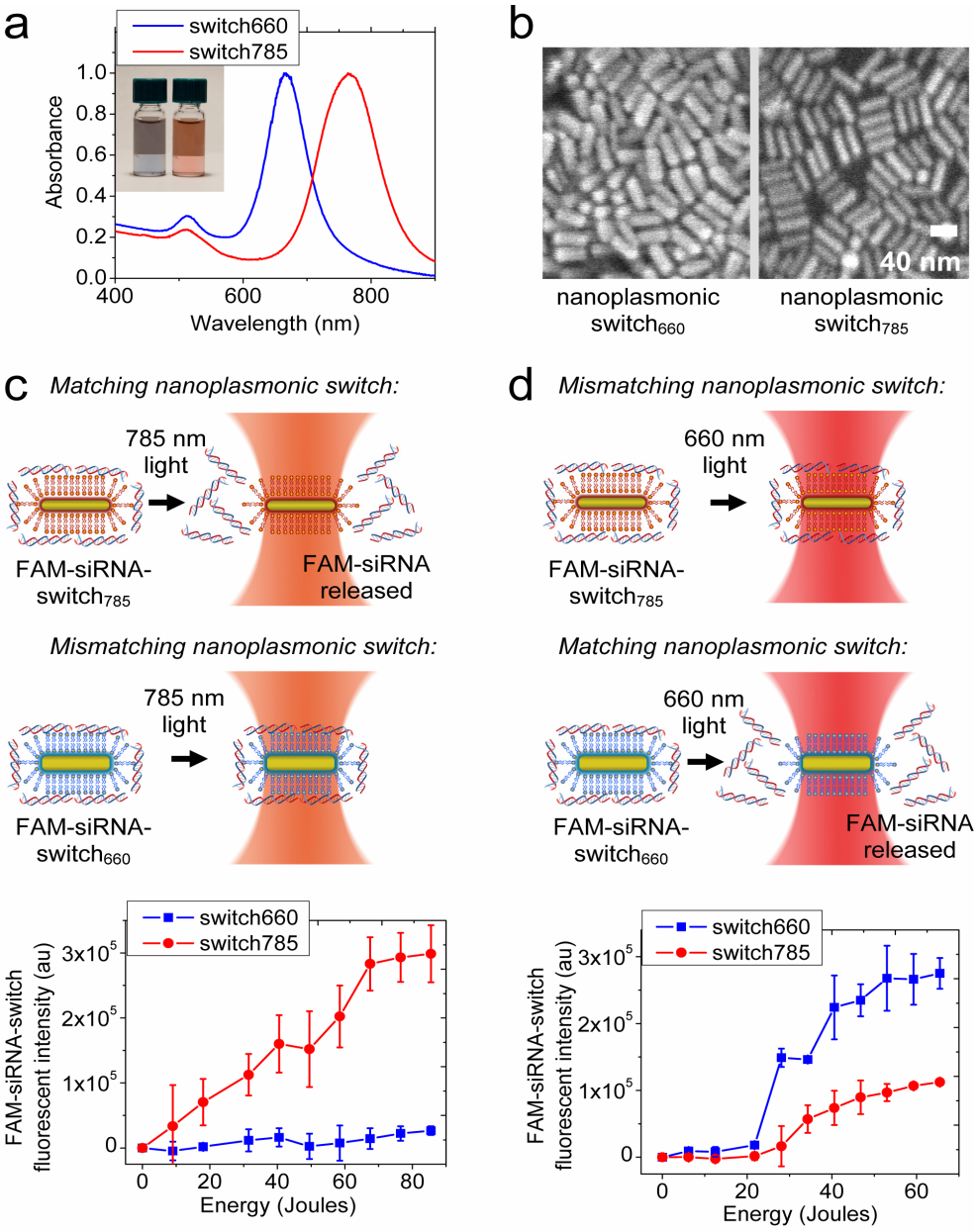

Figure 6.3. Selective and independent photothermal release of siRNA from nanoplasmonic gene switches. (a) UV-VIS spectra of nanoplasmonic gene switches. **(b)** scanning electron microscopy images of nanoplasmonic gene switches, **(c)** FAM-siRNA conjugated switches with longitudinal plasmon resonance 785 nm are illuminated with 785 nm light. siRNA is released. FAM-siRNA conjugated switches with longitudinal plasmon resonance 660 nm are illuminated with 785 nm light. No siRNA is released. **(d)** FAM-siRNA conjugated switches with longitudinal plasmon resonance 785 nm are illuminated with 660 nm light. No siRNA is released. FAM-siRNA conjugated switches with longitudinal plasmon resonance 660 nm are illuminated with 660 nm light. siRNA is released.

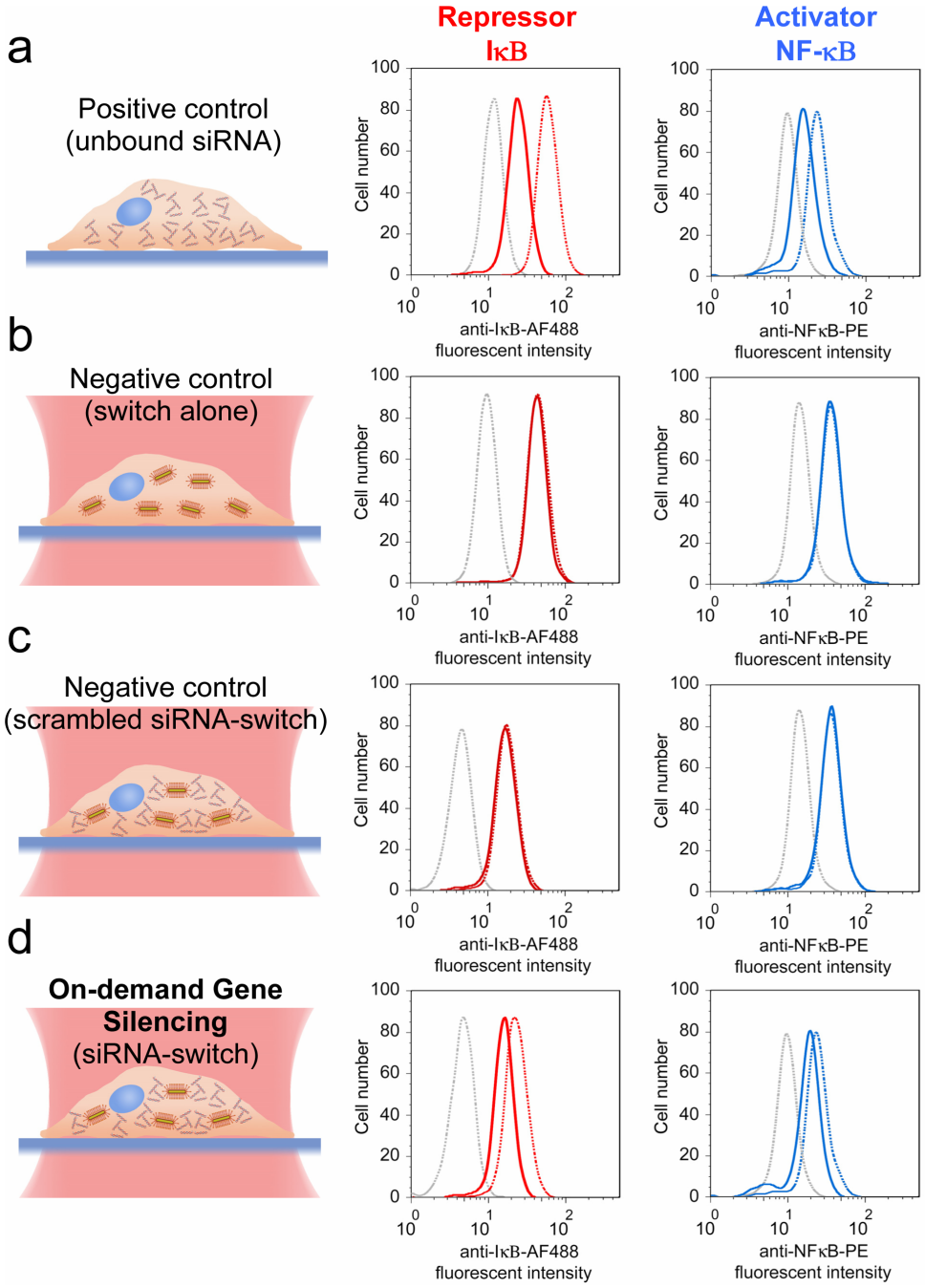

Figure 6.4. On-demand gene silencing of IκB and NF-κB using siRNA. To set dynamic range of flow cytometry fluorescence, grey dotted curve indicates negative isotype control for fluorescence and red/blue dotted curve indicates positive control for fluorescence. **(a)** Red solid line indicates positive control for IκB silencing using unbound siRNA. Blue solid line indicates positive control for NF-κB silencing using unbound siRNA. **(b)** Red solid line indicates negative control for IκB silencing using illuminated nanoplasmonic gene switches lacking siRNA. Blue solid line indicates negative control for NF-κB silencing using illuminated nanoplasmonic gene switches lacking siRNA. **(c)** Red solid line indicates negative control for IκB silencing using illuminated nanoplasmonic gene switches with scrambled siRNA. Blue solid line indicates negative control for NF-κB silencing using illuminated nanoplasmonic gene switches with scrambled siRNA. **(d)** Red solid line indicates on-demand gene silencing of IκB. Blue solid line indicates on-demand gene silencing of NF-κB.

After confirming the photothermal dissociation of siRNA from the cationic phospholipid bilayer, on-demand gene silencing of repressor and activator expression in HeLa cells was conducted. Inhibitory IκB (IκB) was selected to represent the repressor in this article. Likewise, nuclear factor κB (NF-κB) was chosen to represent the activator. Unbound siRNAs targeting IκB and NF-κB strongly decreased their respective expression levels by 50%, verifying their silencing functionality (positive control Fig. 6.4a). The aforementioned standard curves in Chapter 5 were then used to estimate the concentration of nanoplasmonic switches to deliver equivalent concentrations of bound siRNA. The estimated siRNA-conjugated nanoplasmonic switches were then internalized in HeLa cells. Under light illumination, internalized nanoplasmonic switches should photothermally disrupt encapsulating endosomes (14, 16, 39) and photothermally release siRNA. The unbound siRNA should sequentially trigger the RNA-induced silencing complex (RISC) to unwind the duplex, bind to complementary messenger RNA (mRNA), and silence gene expression (40). On-demand gene silencing of IκB resulted in a 30% decrease in IκB expression (Fig. 6.4d). A similar decrease in NF-κB expression was also seen after on-demand gene silencing of NF-κB (Fig. 6.4d). To ensure that illumination of nanoplasmonic switches themselves caused no down-regulation effects, nanoplasmonic switches without siRNA were internalized in control HeLa cells. No decrease in IκB or NF-κB protein levels were observed when nanoplasmonic switches alone (lacking siRNA) were illuminated (negative control Fig. 6.4b). Scrambled siRNA-conjugated nanoplasmonic switches were also internalized in HeLa cells and illuminated to verify no non-specific, off-target down-regulation of IκB or NF-κB protein levels occurred (negative control Fig. 6.4c).

To further assess functionality, downstream nuclear translocation was examined after nanoplasmonic silencing of IκB and NF-κB expression. To locate cells' boundaries and nuclei, DIC images and DAPI-stained images were placed adjacent to NF-κB-immunostained images (Fig. 6.5). The activator NF-κB and the repressor IκB form an inactive complex that typically remains sequestered in the cytoplasm (41), as shown in the negative control (Fig. 6.5, column i). External stimuli, such as the tumor necrosis factor alpha (TNFα), signal the degradation of the repressor IκB and the subsequent nuclear translocation of the now "active" NF-κB, as shown by the strong nuclear presence of NF-κB in the positive control (Fig. 6.5, column ii). In a similar fashion, Fig. 6.5, column (iii) also shows the presence of NF-κB in the nucleus after on-demand gene silencing of the repressor IκB, indicating that IκB was inhibited, the IκB/ NF-κB complex was dissociated, and the active NF-κB was able to translocate to the nucleus. In contrast, on-demand gene silencing of NF-κB decreased overall expression of NF-κB (Fig. 6.5, column iv). No nuclear translocation was observed. Since downstream translocation activities could be visualized after nanoplasmonic silencing of NF-κB and IκB, it was reasoned that nanoplasmonic control of downstream target genes should also be conceivable.

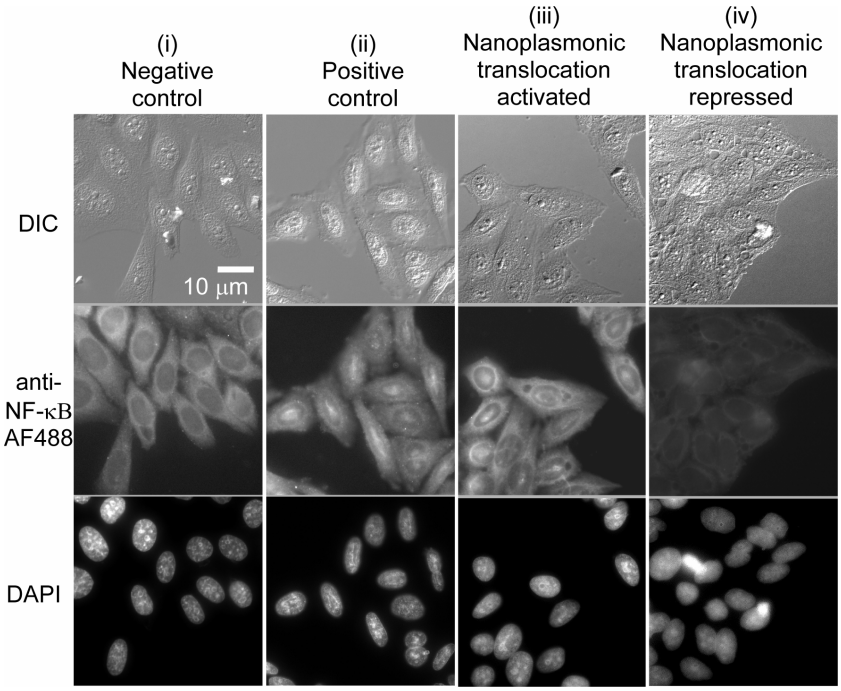

Figure 6.5. Downstream translocation events after on-demand gene silencing of repressor IκB and activator NF-κB. DIC, immunostaining of NF-κB, and DAPI staining of nuclei of (i) untreated cells (negative control), (ii) cells treated with TNFα (positive control), (iii) cells after on-demand gene silencing of repressor IκB (nanoplasmonic translocation activated), and (iv) cells after on-demand gene silencing of activator NF-κB (nanoplasmonic translocation repressed).

Finally, a transcriptional pulse of target gene expression was generated by utilizing siRNA-conjugated nanoplasmonic switches of different aspect ratios to selectively and temporally manipulate the activities of repressors and activators upstream from the target gene. On-demand gene silencing of the repressor IκB was used to activate target gene expression and thereby initiate the transcriptional pulse (t_1 = 0 hrs). To terminate the transcriptional pulse, on-demand gene silencing of NF-κB was used to repress the target gene expression (t_2 = 2 hrs). To test this hypothesis, two target genes with different transcriptional activation profiles were examined. The target gene IP-10 is an early response gene and is known to be immediately activated within 30 minutes of stimulation, whereas the target gene RANTES is a late response gene and requires more than 3 hours of stimulation to be activated (3, 42, 43). If the transcriptional pulse was indeed generated, IP-10 should be activated while RANTES should remain inactivated. A genetic logic table summarizing the behavior of IP-10 and RANTES is shown in Figure 6.6. In Figure 6.6d, flow cytometric results show activation of IP-10 expression while RANTES expression remains inactivated, confirming that a transcriptional pulse was generated using nanoplasmonic control. Control experiments were carried out to ensure that persistent silencing of repressor IκB resulted in activation of both IP-10 and RANTES (Fig. 6.6c). Both IP-10 and RANTES remained inactivated when activator NF-κB was persistently silenced (Fig. 6.6b).

	Repressor IκB siRNA bound	*Activator* NF-κB siRNA bound	*Early gene* IP-10	*Late gene* RANTES
(a)	0	0	0	0
(b)	0	1	0	0
(c)	1	0	1	1
(d)	1	1	1 *t* >0.5 hrs 0 otherwise	1 *t* >3 hrs 0 otherwise

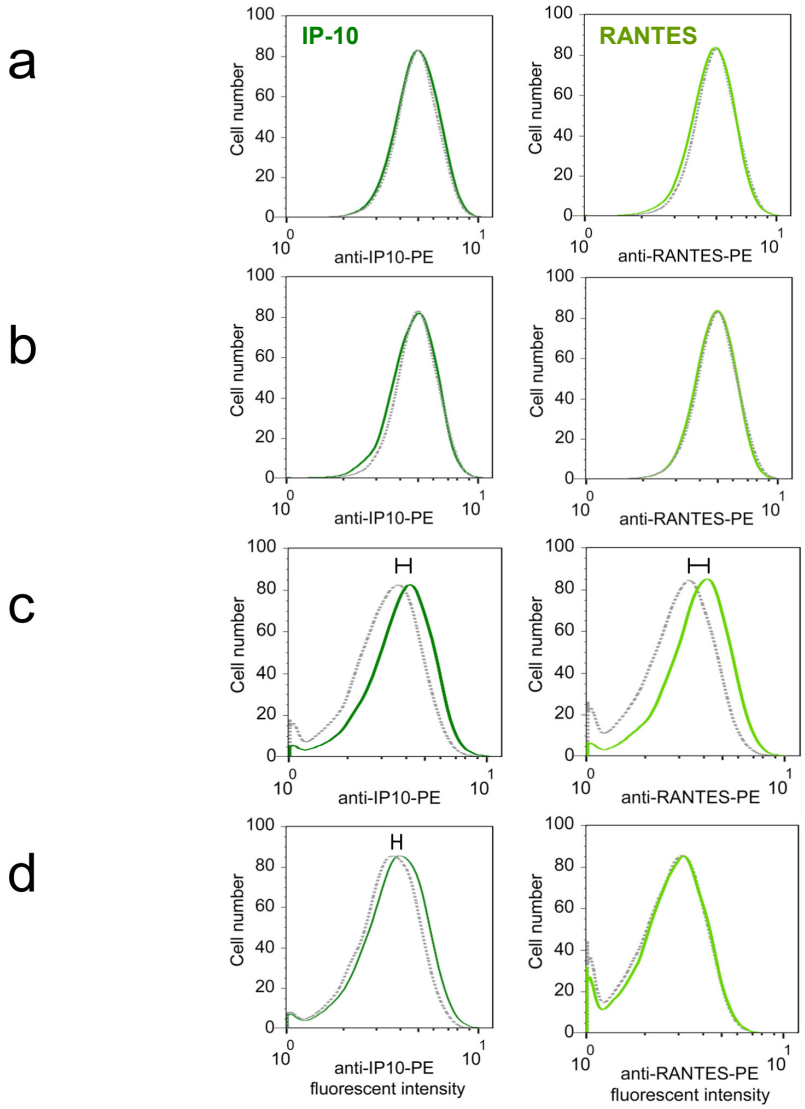

Figure 6.6. Transcriptional pulse characterized by examining activation of early gene IP-10 and late gene RANTES by flow cytometry. Grey dotted line represents negative, unactivated control. Green solid curves represent IP-10 or RANTES activation. **(a)** No IκB or NF-κB silencing: IP-10 and RANTES unactivated. **(b)** Persistent NF-κB silencing: IP-10 and RANTES unactivated. **(c)** Persistent IκB silencing: both IP-10 and RANTES activated. **(d)** Two hour transcriptional pulse created: IP-10 activated, RANTES unactivated.

In closing, a nanoplasmonics-enabled transcriptional pulse generation of target gene expression was demonstrated. Using nanoplasmonic control, the timing of genetic activities can be systematically varied on-demand. It is possible to temporally control biological behavior in future studies in order to understand how exactly transient and steady-state responses dictate normal biological processes and how unregulated behavior can lead to dysfunction. Equipped with new nanoplasmonic tools to directly probe the intracellular space, quantitative approaches should capture many dynamic activities within the living cell that were otherwise previously impossible to detect using conventional methods. We therefore expect these nanoplasmonic tools and methodologies to have important implications in advancing drug delivery, gene delivery, imaging, and therapeutics.

References

1. Alon, *An Introduction to Systems Biology*, CRC Press (2007).
2. Chubb, J. R., Trcek, T., Shenoy, S.M., Singler, R.H., Transcriptional Pulsing of a Developmental Gene, *Current Biology, 16*, 1018 (2006).
3. Hoffman, A., Levchenko, A., Scott, M.L., Baltimore, D., The IkB-NFkB Signaling Module: Temporal Control and Selective Gene Activation, *Science, 298*, 1241 (2002).
4. Weinberger, L. S., Dar, R.D., Simpson, M.L., Transient-Mediated Fate Determination in Transcriptional Circuit of HIV, *Nature Genetics, 40*, 466 (2008).
5. Basu, S., Mehreja, R., Thiberge, S., Chen, M., Weiss, R., Spatiotemporal Control of Gene Expression with Pulse Generating Networks, *Proceedings of the National Academy of Sciences, 101*, 6355 (2004).
6. Elowitz, M. B., Leibler, S., A Synthetic Oscillatory Network of Transcriptional Regulators, *Nature Genetics, 403*, 335 (2000).
7. Stricker, J., Cookson, S., Bennett, M.R., Mather, W.H., Tsimring, L.S., Hasty, J., A Fast Robust and Tunable Synthetic Gene Oscillator, *Nature, 456*, 516 (2008).
8. Tigges, M., Marquez-Lago, T.T., Stelling, J., Fussenegger, M., A Tunable Synthetic Mammalian Oscillator, *Nature, 457*, 309 (2009).
9. Barhoumi, A., Huschka, R., Bardhana, R., Knight, M.W., Halas, N.J., Light-Induced Release of DNA from Plasmon-Resonant Nanoparticles: Towards Light-Controlled Gene Therapy, *Chemical Physics Letters, 482*, 171 (2009).
10. Braun, G. B., Pallaoro, A., Wu, G., Missirlis, D., Zasadzinski, J.A., Tirrell, M., Reich, N.O., Laser-Activated Gene Silencing via Gold Nanoshell-siRNA Conjugates, *ACS Nano, 3*, 2007 (2009).
11. Chen, C., Lin, Y., Wang, C., Tzeng, H., Wu, C., Chen, Y., Chen, C., Chen, L., Wu, Y., DNA-Gold Nanorod Conjugates for Remote Control of Localized Gene Expression by near Infrared Irradiation, *Journal of the Americal Chemical Society, 128*, 3709 (2006).
12. Choi, M., Stanton-Maxey, K. J., Stanley, J. K., Levin, C. S., Bardhan, R., Akin, D., Badve, S., Sturgis, J., Robinson, J. R., Bashir, R., Halas,, and N. J., C., S. E., A Cellular Trojan Horse for Delivery of Therapeutic Nanoparticles into Tumors, *Nanoletters, 7*, 3759 (2007).

13. Wijaya, A., Schaffer, S.B., Pallares, I.G., Hamad-Schifferli, K., Selective Release of Multiple DNA Oligonucleotides from Gold Nanorods, *ACS Nano, 3*, 80 (2009).
14. Lee, S. E., Liu, G. L., Kim, F., Lee, L. P., Remote Optical Switch for Localized and Selective Control of Gene Interference, *Nanoletters, 9*, 562 (2009).
15. Skrabalak, S. E. C., J.; Au, L.; Lu, X.; Li, X.; Xia, Y., Gold Nanocages for Biomedical Applications, *Advanced Materials, 19*, 3177–3184 (2007).
16. Skirtach, A. G., Javier, A. M., Kreft, O., Kohler, K., Alberola, A. P., Mohwald, H., Parak, W. J., Sukhorukov, G. B., Laser-Induced Release of Encapsulated Materials inside Living Cells, *Angew. Chem. Int. Ed., 45*, 4612 –4617 (2006).
17. Skirtach, A. G., Dejugnat, C., Braun, D., Susha, A.S., Rogach, A.L., Parak, W.J., Mohwald, H., Sukhorukov, G.B., The Role of Metal Nanoparticles in Remote Release of Encapsulated Materials, *Nanoletters, 5*, 1371 (2005).
18. Sershen, S. R., Westcott, S. L., Halas, N. J., West, J. L., Temperature-Sensitive Polymer–Nanoshell Composites for Photothermally Modulated Drug Delivery, *J. Biomed. Mater. Res., 51*, 293–298 (2000).
19. Ren, L., Chow, G.M., Synthesis of NIR-Sensitive Au–Au2S Nanocolloids for Drug Delivery, *Materials Science and Engineering, C23*, 113–116 (2003).
20. Han, G., You, C., Kim, B., Turingan, R., Forbes, N., Martin, C.T., Rotello, V.M., Light-Regulated Release of DNA and Its Delivery to Nuclei by Means of Photolabile Gold Nanoparticles, *Angew. Chem. Int. Ed., 118*, 3237 –3241 (2006).
21. Hauck, T. S., Jennings, T. L., Yatsenko, T., Kumaradas, J. C., Chan, W. C., Enhancing the Toxicity of Cancer Chemotherapeutics with Gold Nanorod Hyperthermia, *Advanced Materials, 20*, 3832–3838 (2008).
22. Horiguchi, Y., Niidome, T., Yamada, S., Nakashima, N., Niidome, Y., Expression of Plasmid DNA Released from DNA Conjugates of Gold Nanorods, *Chemistry Letters, 36*, 952–953 (2007).
23. Huang, X., El-Sayed, I. H., Qian, W., El-Sayed, M. A., Cancer Cell Imaging and Photothermal Therapy in the Near-Infrared Region by Using Gold Nanorods, *Journal of the Americal Chemical Society, 128*, 2115 (2006).
24. Huang, Y. F., Sefah, K., Bamrungsap, S., Chang, H., Tan, W., Selective Photothermal Therapy for Mixed Cancer Cells Using Aptamer-Conjugated Nanorods, *Langmuir, 24*, 11860 (2008).
25. Jones, M. R., Millstone, J.E., Giljohann, D.A., Seferos, D.S., Young, K.L., Mirkin, C.A., Plasmonically Controlled Nucleic Acid Dehybridization with Gold Nanoprisms, *ChemPhysChem, 10*, 1461 (2009).
26. Norman, R. S., Stone, J. W., Gole, A., Murphy, C. J., Sabo-Attwood, T. L., Targeted Photothermal Lysis of the Pathogenic Bacteria, Pseudomonas aeruginosa, with Gold Nanorods, *Nanoletters, 8*, 302 (2008).
27. Pissuwan, D., Valenzuela, S. M., Killingsworth, M. C., Xu, X., Cortie, M., Targeted Destruction of Murine Macrophage Cells with Bioconjugated Gold Nanorods, *Journal of Nanoparticle Research, 9*, 1109–1124 (2007).
28. Takahashi, H., Niidome, Y., Yamada, S., Controlled Release of Plasmid DNA from Gold Nanorods Induced by Pulsed Near-Infrared Light, *Chem. Commun.*, 2247–2249 (2005).
29. Cortie, M., Xu, X., Chowdhury, H., Zareie, H., Smith, G., Plasmonic Heating of Gold Nanoparticles and Its Exploitation, *Proc. SPIE, 5649*, 565–573 (2005).

30. Khlebtsov, B., Zharov, V., Melnikov, A., Tuchin, V., Khlebtsov, N., Optical Amplification of Photothermal Therapy with Gold Nanoparticles and Nanoclusters, *Nanotechnology, 17*, 5167–5179 (2006).
31. Link, S., El-Sayed, M., Shape and Size Dependence of Radiative, Non-Radiative and Photothermal Properties of Gold Nanocrystals, *Int. Reviews in Physical Chemistry, 19*, 409 (2000).
32. Svoboda, K., Biological Applications of Optical Forces, *Annu. Rev. Biophys. Biomol. Struct., 23*, 247 (1994).
33. Hartgrove, J., Schmidt, F., The Role of mRNA and Protein Stability in Gene Expression, *The FASEB Journal, 3*, 2360 (1989).
34. Barlett, D., Davis M., Effect of siRNA Nuclease Stability on the in vitro and in vivo Kinetics of siRNA-Mediated Gene Silencing, *Biotechnology and Bioengineering, 97*, 909 (2007).
35. Rosi, N. L., Giljohann, D.A., Thaxton, C.S., Lytton-Jean, A.K.R., Han, M.S., Mirkin, C.A., Oligonucleotide-Modified Gold Nanoparticles for Intracellular Gene Regulation, *Science, 312*, 1027 (2006).
36. Lee, S. E., Sasaki, D.Y., Perroud, T.D., Yoo, D., Patel, K.D., Lee, L.P., Biologically Functional Cationic Phospholipid-Gold Nanoplasmonic Carriers of RNA, *Journal of the Americal Chemical Society, 131*, 14066–14074 (2009).
37. Gou, L., Murphy, C. J., Fine-Tuning the Shape of Gold Nanorods, *Chem. Mater., 17*, 3668 (2005).
38. Nikoobakht, B., El-Sayed, M. A., Preparation and Growth Mechanism of Gold Nanorods (NRs) Using Seed-Mediated Growth Method, *Chem. Mater., 15*, 1957 (2003).
39. Wu, G., Mikhailovsky, A., Khant, H.A., Fu, C., Chiu, W., Zasadzinski, J.A., Remotely Triggered Liposome Release by Near-Infrared Light Absorption via Hollow Gold Nanoshells, *Journal of the American Chemical Society, 130*, 8175–8177 (2008).
40. Sontheimer, E., Assembly and Function of RNA Silencing Complexes, *Nature Reviews Molecular Cell Biology, 6*, 127 (2005).
41. Lee, J., Burckart, G.J., Nuclear Factor Kappa B: Important Transcription Factor and Therapeutic Target, *J. Clin. Pharmacol., 38*, 981 (1998).
42. Liu, Q., Muruve, D.A., Molecular Basis of the Inflammatory Response to Adenovirus Vectors, *Gene Therapy, 10*, 935 (2003).
43. Bowen, G. P., Borland, S.L., Lam, M., Libermann, T.A., Wong, N.C.W., Muruve, D.A., Adenovirus Vector-Induced Inflammation: Capsid Dependent Induction of the C-C Chemokine RANTES Requires NF-kB, *Human Gene Therapy, 13*, 367 (2002).

CHAPTER 7:
FUTURE WORK AND CONCLUSIONS

A living cell dynamically responds to its perpetually changing environment, such that signaling proteins, transcription factors, and enzymes are constantly synthesized, transported from one organelle to another, and finally shuttled to their appropriate locations to give rise to cell function. The intracellular distribution of these molecular complexes is spatially non-uniform and dynamically changing over time in response to environmental cues (1). Quantitative knowledge of the intracellular biochemical distribution is critical for understanding intracellular organization and function in developmental processes, growth, differentiation, apoptosis, and disease.

Intracellular manipulation in conjunction with real-time imaging can provide unparalleled insight into the intracellular biochemical distribution as a result of local environmental changes. Recent advancements in nanotechnology and nanoplasmonics now enable nanoplasmonic optical antennae to directly interface with intracellular processes. The dual functions of nanoplasmonic optical antennae, discussed in Chapter 2, can be utilized in combination to enable intracellular manipulation in conjunction with real-time imaging. By focusing electromagnetic fields down to dimensions smaller than the diffraction limit, nanoplasmonic optical antennae - functioning as nanoplasmonic gene switches - enable spatially precise regulation of genetic activity to give rise to location-specific function. Additionally, nanoplasmonic optical antennae - functioning as biosensors – can also focus electromagnetic fields to significantly enhance spectral information for plasmon resonance energy transfer (PRET) (2-4) and surface-enhanced Raman spectroscopy (SERS) (5-13). By utilizing a combination of both nanoplasmonic gene switches and biosensors in an experiment (Fig. 7.1), quantitative “spectral snapshots” (ie. spectroscopic imaging) of the intracellular biochemical distribution can be obtained over time as function of changes in the local environment.

Integration with PRET biosensors

PRET biosensors enhance spectral information of biomolecules in the local environment. Plasmon resonance energy can be transferred from nanoplasmonic optical antennae, functioning as biosensors, to molecules in proximity. When the plasmon resonance spectrum of an antenna is intentionally matched to the absorption spectrum of the molecules, energy transfer by PRET (2-4) results in wavelength-specific quenching in the Rayleigh scattering spectrum. For instance, when the plasmon resonance energy of the biosensors is transferred to adsorbed cytochrome *c*, wavelength-specific quenching is observed in the Rayleigh scattering spectrum of the biosensor (2, 4). The quenching positions exactly correspond to the absorbance peaks of cytochrome *c*.

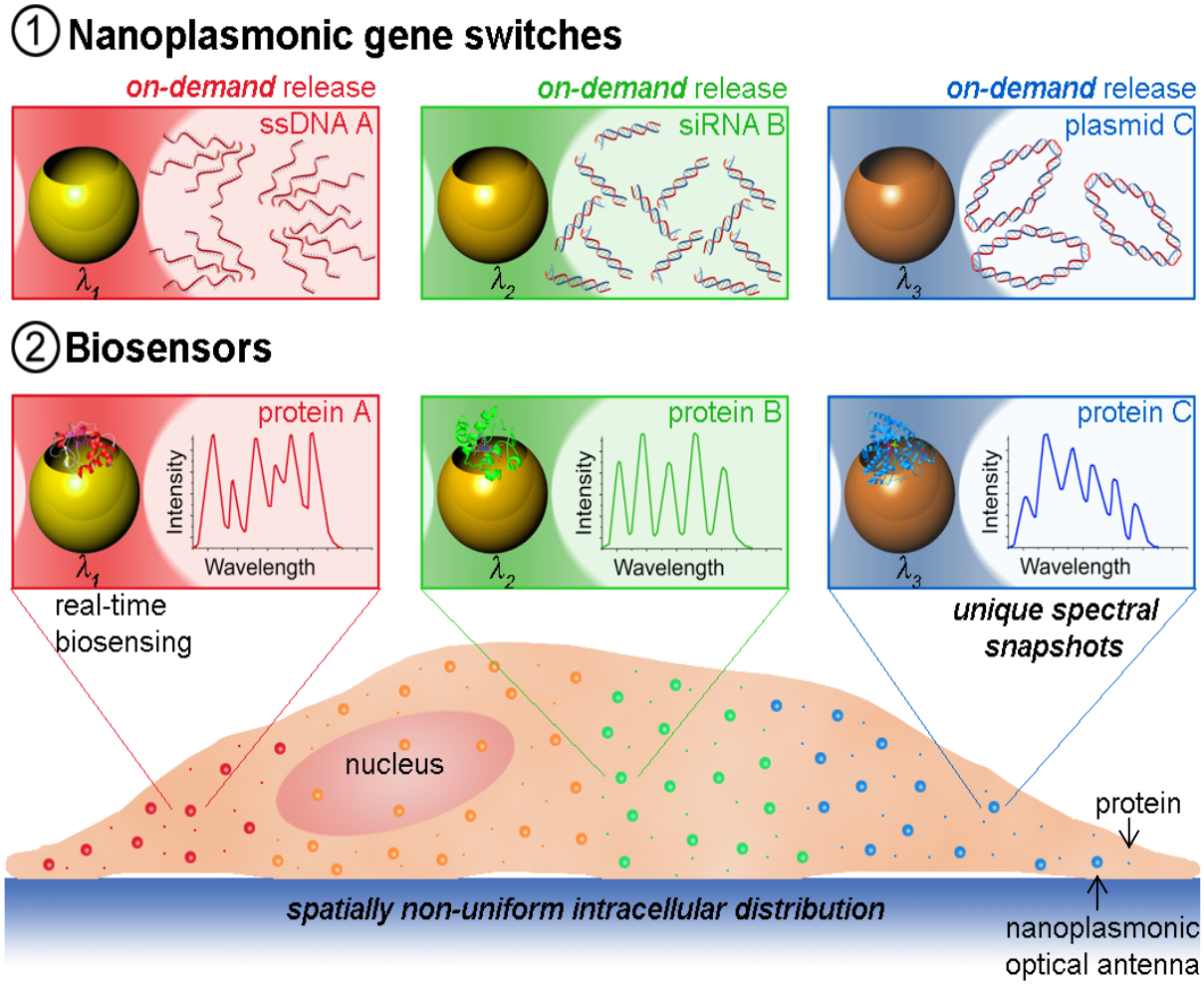

Figure 7.1. Concept of nanoplasmonic optical antennae for on-demand gene regulation and real-time imaging. The intracellular distribution is spatially non-uniform and dynamically changing over time in response to environmental cues. By focusing electromagnetic fields down to dimensions smaller than the diffraction limit, nanoplasmonic optical antennae - functioning as nanoplasmonic gene switches - enable on-demand and spatially precise gene regulation to give rise to location-specific function. In addition to on-demand gene regulation, nanoplasmonic optical antennae - functioning as biosensors - enhance spectral information for PRET and SERS. "Spectral snapshots" of the dynamically changing intracellular biochemical distribution can be obtained over time using multiple nanoplasmonic optical antennae with distinct plasmon resonance wavelengths matched to incident light wavelengths λ_1, λ_2, and λ_3.

In addition to cytochrome *c* sensing, highly sensitive and selective metal ion sensing is also enabled by PRET spectroscopy. When the transition metal ion (blue) binds with the matching ligand (red), *d* orbitals are split, generating a new absorption band of the metal-ligand complex in the visible range (3). Due to this new absorption band, Rayleigh scattering energy from the biosensor can be transferred to the metal-ligand complex. There is no spectral overlap between ligands and the biosensor in the absence of the metal ion. When the electronic absorption frequency of the metal-ligand complex matches with the Rayleigh scattering frequency, the selective energy transfer

is induced by this spectral overlap and distinguishable resonant quenching in the resonant Rayleigh scattering spectrum is observed (3).

Integration with SERS biosensors

SERS biosensors also enhance spectral information of biomolecules in the local environment. In the presence of incoming electromagnetic radiation, molecules in proximity of the biosensor undergo a momentary transition from the ground state to a virtual state. Transitions are related to the biochemical composition. Enhanced Raman scattering, utilized in surface-enhanced Raman spectroscopy (SERS) (5-13), results when the transition is immediately to a vibrational level of the ground state. Therefore, the spectral information captured by SERS biosensors is a unique molecular fingerprint which can be used to identify molecules-of-interest in a label-free manner. For example, biologically functional gold nanocrescent antennae utilized as SERS biosensors (9). For sensing of Rhodamine 6G, vibrational peaks (ex. 615 cm^{-1}), corresponding to the aromatic ring bending and stretching of Rhodamine 6G, were shown to be significantly enhanced, with an estimated Raman enhancement factor of larger than 10^{10} using this SERS biosensor. Magnetically controlled magnetic-gold nanocrescent antennae have also been fabricated to enable external control of the position and orientation of the SERS biosensors. The orientation of asymmetric biosensors has been shown to be absolutely critical for enabling large local field enhancement and therefore high biosensor sensitivity (8).

Conclusions

In this dissertation, on-demand gene silencing of endogenous intracellular genes using antisense DNA was demonstrated. In addition to antisense DNA, siRNA is also known to inducing silencing effects. Therefore, biologically functional cationic phospholipid-gold nanoplasmonic carriers that are compatible with and capable of carrying siRNA cargo were also fabricated. Using biologically functional cationic phospholipid-gold nanoplasmonic carriers of siRNA, on-demand gene silencing of endogenous intracellular genes by siRNA was demonstrated. In addition to inhibitory effects, genes can also be expressed on-demand using nanoplasmonic optical antennae. A transcriptional pulse of target gene expression was generated using siRNA-conjugated nanoplasmonic gene switches of different aspect ratios to selectively and temporally manipulate the activities of repressors and activators upstream from the target gene. Equipped with new nanoplasmonic optical antennae to directly probe the intracellular space, quantitative and systematic approaches should capture many dynamic activities within the living cell that were otherwise previously impossible to detect using conventional methods.

References

1. Alberts, B., Johnson, A., Lewis, J., Raff, M., Roberts, K., Walters, P., *Molecular Biology of the Cell*, Garland Science, New York (2002).
2. Liu, G. L., Long, Y., Choi, Y., Kang, T., Lee, L.P., Quantized Plasmon Quenching Dips Nanospectroscopy via Plasmon Resonance Energy Transfer, *Nature Methods, 4*, 1015 (2007).
3. Choi, Y., Park, Y., Kang, T., Lee, L.P., Selective and Sensitive Detection of Metal Ions by Plasmon Resonance Energy Transfer-based Nanospectroscopy, *Nature Nanotechnology, 4*, 742 (2009).
4. Choi, Y., Kang, T., Lee, L.P., Plasmon Resonance Energy Transfer (PRET)-based Molecular Imaging of Cytochrome c in Living Cells, *Nanoletters, 9*, 85 (2009).
5. Nikoobakht, B., Wang, J., El-Sayed, M. A., Surface-enhanced Raman Scattering of Molecules Adsorbed on Gold Nanorods: Off-Surface Plasmon Resonance Condition, *Chemical Physics Letters, 366*, 17–23 (2002).
6. Nie, S., Emory, S.R., Probing Single Molecules and Single Nanoparticles by Surface-Enhanced Raman Scattering, *Science, 275*, 1102 (1997).
7. Willets, K. A., Van Duyne, R.P., Localized Surface Plasmon Resonance Spectroscopy and Sensing, *Annu. Rev. Phys. Chem., 58*, 267–297 (2007).
8. Liu, G. L., Lu, Y., Kim, J., Doll, J.C., Lee, L.P., Magnetic Nanocrescents as Controllable Surface-enhanced Raman Scattering Nanoprobes for Biomolecular Imaging, *Advanced Materials, 17*, 2683 (2005).
9. Lu, Y., Liu, G.L., Kim, J., Mejia, Y.X., Lee, L.P., Nanophotonic Crescent Moon Structures with Sharp Edge for Ultrasensitive Biomolecular Detection by Local Electromagnetic Field Enhancement Effect, *Nanoletters, 5*, 119 (2005).
10. Kniepp, K., Kniepp, H., Itzkan, I., Dasari, R.R., Feld, M.S., Ultrasensitive Chemical Analysis by Raman Spectroscopy, *Chem. Rev., 99*, 2957 (1999).
11. Jackson, J. B., Halas, N.J., Surface-enhanced Raman Scattering on Tunable Plasmonic Nanoparticle Substrates, *Proceedings of the National Academy of Sciences, 101*, 17930–17935 (2004).
12. Cho, H., Lee, B., Liu, G.L., Agarwal, A., Lee, L.P., Label-free and Highly Sensitive Biomolecular Detection using SERS and Electrokinetic Preconcentration, *Lab Chip, 9*, 3360–3363 (2009).
13. Choi, D., Kang, T., Cho, H., Choi, Y., Lee, L.P., Additional Amplifications of SERS via an Optofluidic CD-based Platform, *Lab Chip, 9*, 239 (2009).